POLITECNICO DI MILANO
Dipartimento di Elettronica, Informazione e Bioingegneria
DOTTORATO IN INGEGNERIA DELL'INFORMAZIONE

Integration of Direct-Written Organic Photodetectors and Organic Transistors: Towards Passive Pixels for Plastic Large-Area Imagers

Doctoral Dissertation of:
Andrea Grimoldi

Advisor:
Prof. Dario Andrea Nicola Natali
Tutor:
Prof. Angelo Geraci
Supervisor of the Doctoral Program:
Prof. Carlo Fiorini

2015 - XXVIII

Contents

Abstract

In the past few decades organic electronics has raised considerable interest because of solution processability, mechanical flexibility and tunable optical capabilities of organic semiconductors. The related development of solution process technology paves the way for large area, low cost and flexible electronics. Printing techniques mutated from graphical art can successfully cope with the need of patterning capability. Among them inkjet printing allows fast prototyping and reduced waste of material.

In light exploiting applications organic semiconductors show outstanding characteristics with their high absorption coefficients and typical luminescence in the visible range of wavelengths. Organic LED-based screens and lighting systems are gaining more and more market share. Moreover, great scientific and engineering investigations are leading to significant improvement in the efficiency of organic solar cells.

The field of organic photodetectors has seen a raise in research efforts during last years, opening the way to new optoelectronic applications in medical and industrial imaging, telecommunications and environmental control. The realization, characterization and optimization of organic photodetectors fabricated by means of inkjet printing technology are the research subjects of this thesis. After an introductive chapter, where a description of fabrication techniques and an overview of the state of art of inkjet printed photosensors are provided, the thesis is organised in two parts: the first concerning the optimization of vertical photodetectors aiming to their integration with switching elements to build an organic imager; the second focusing on the development of photodetectors with reduced dark current, extended spectral response or integrated in complex electronic circuits.

Large area, non-fragile imagers are devices of great attractiveness for X-ray medical and industrial diagnostic, but a fully-direct-written matrix has not been demonstrated yet. Concerning these large area imagers, specific performances are requested for the light sensing element. In chapter 2 we go through a careful optimization of a first inkjet printed photodetector prototype. The feedback from characterization helped to adjust step by step the

device structure to the specifics. The selection of bottom electrode and its functionalizer led to the realization of devices fulfilling the specifics for a large area imager. The following chapter is devoted to the fabrication of a prototype imager, after an introduction on the fundamentals of its operation principle. The integration of the photosensitive element described before with an addressing component is a non-trivial task and it is deeply discussed. Finally, the fabrication and the characterization of a direct-written organic imager is presented.

While the first part is related to a specific application, the latter copes with three different purposes. In organic photodetectors electrode/semiconductor interface plays an important role determining the amount of carriers injection and consequently the dark current. This is a key performance that can enable or not the integration of a light sensor in system with demanding signal-to-noise ratio requirement. Moreover, interface traps can affect the response speed of the device. These considerations encouraged us to work on devices with a suitably synthesized interlayer. A double aim was sought for the new layer: to reduce dark current and to improve the wettability of the top water-based electrode on a hydrophobic photoactive material. Fabrication process and results of electro-optical characterization of these new detectors are presented in chapter 4.

Photodetectors with photoactive blend based on small molecules is presented in chapter 5. Small molecules have some advantages with respect to polymers, in particular they are not affected by polydispersity and are characterized by a simpler purification technique. An approach that allows small molecule printing is proposed. Moreover, the extension of the photoresponse to NIR range was addressed. At last results of an in-depth study on the role of PFN are reported.

In the last chapter another integration topic is presented. Being requirements on dark current and on photodetector dimensions more relaxed with respect to the strict ones of the first part, planar structure can be adopted. This choice was necessary to operate transistors of the circuit at their characteristic voltages. The validation of the realized system as dusk sensor is proven by full-system measurements.

Chapter 1

Background knowledge

In this chapter the fundamental knowledge will be briefly reviewed to provide the background needed to appreciate the experimental efforts presented in this thesis. In particular fabrication techniques exploited in this work will be described pointing out their advantages and constrains. After that the working mechanism of photodetectors and phototransistors will be discussed together with their relevant figures of merit. The last part of the chapter is an overview of the inkjet printed photosensors, which compare to the ones developed in this work.

1.1 Fabrication techniques

In contrast to lithographic methods, mostly employed in the fabrication of inorganic devices via a subtractive approach, direct-writing technology does not use secondary instrumentation or processes (such as masks or litography lift-off) but additive techniques which involve a single deposition step per layer, eventually followed by a drying or a sintering step. This strategy reduces time and costs needed for the fabrication, furthermore lowers the amount of wasted materials. Latter we will report only those techniques employed in this work for the fabrication of organic photodetectors and transistor: inkjet printing and femtosecond laser ablation.

1.1.1 Inkjet printing

Inkjet printing[1] is a digital, additive and very flexible printing technique which could enable the cost-effective fabrication of different devices into large-area electronic systems and it was adopted in the past to demonstrate high-performance field-effect transistors and circuits,[2–4] memory devices,[5] sen-

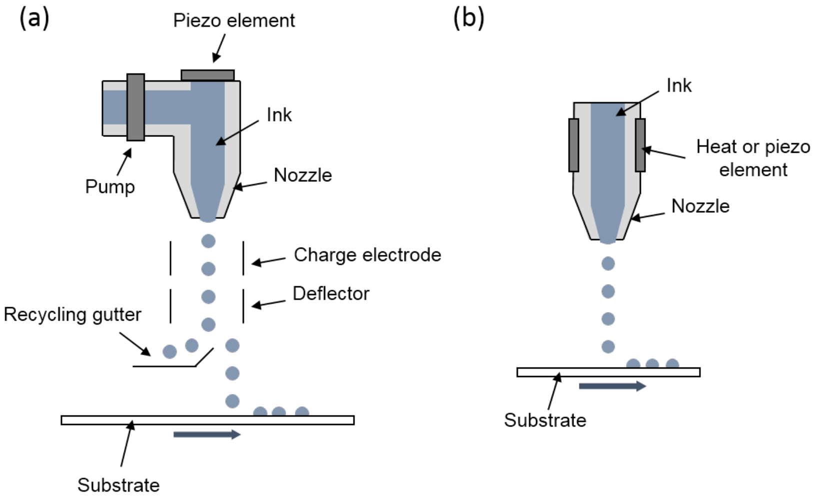

Figure 1.1: Schemes of continuous (a) and DOD (b) inkjet printer nozzles.

sors[6–10] and polymer solar cells.[2,11] Inkjet printing exploits a drop-by-drop deposition approach.[2] The droplets of a low viscosity solution are jetted by a nozzle and can be generated either continuously or on demand (drop-on-demand). In the continuous mode a pressure ejects ink from the nozzle creating a stream of liquid that forms droplets due to Rayleigh instability which are charged by an electric field applied to the nozzle (fig. 1.1a). Charged droplets are separated from the uncharged ones and deflected by an electric field before reaching the substrate. The uncharged droplets are undeflected and collected by a gutter and re-used. The very high ejecting frequency (65000 – 165000 droplets/s) enables fast printing. Nozzle clogging is prevented because the jet is always active, allowing also the use of volatile solvents. However, for desktop applications, industrial productions requiring a higher precision and lab-scale research, the drop-on-demand (DOD) system is more commonly used because of a lower system complexity and higher accuracy of droplet displacement. With DOD, thermal bubble techniques or piezoelectric transducers are used to force droplets out of the nozzle (fig. 1.1b). A thermal printhead uses a heater causing a rapid vaporization of the ink and inducing the formation of a bubble. Consequently, the pressure in the nozzle increases, forcing a droplet to be ejected. Thermal DOD technology is simple in design and features lower costs, but it is restricted to vaporizable fluids required for the bubble's formation. Due to this limitation, piezoelectric transduction is commonly preferred and indeed all the examples of inkjet printed photodetectors so far reported in

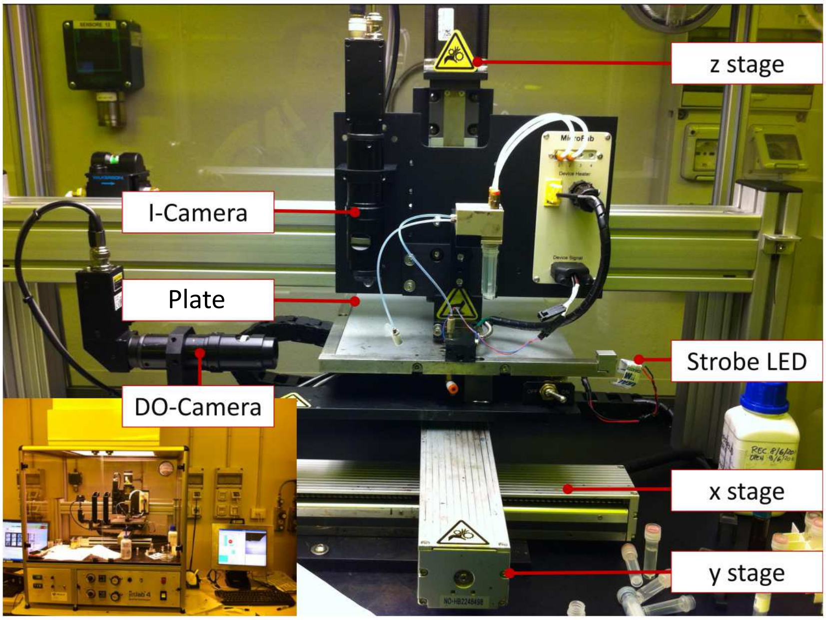

Figure 1.2: Photograph of Microfab JETLAB 4 inkjet printer used in this work.

literature make use of this approach. In piezoelectric printheads a piezoelectric material is electrically stimulated causing its compression and expansion according to its resonant modes. As a result, a pressure wave propagates into the nozzle propelling a droplet out of it. Ink viscosity must be in the range of 1 to $30mPas$. Typically patterns deposited by inkjet printing have feature sizes of $20-50\mu m$, in the best cases, and thickness lower than $1\mu m$. Inkjet printing throughput is around $0.01-0.5m^2/s$ and the registration is pretty good, with an alignment error possibly smaller than $10\mu m$.

Inkjet printing has been employed in various fabrication processes of organic optoelectronics devices.[2,12,13]

In this work two DOD inkjet printers are exploited (fig. 1.2). In the following a brief description of the main aspects that have to be taken in consideration for deposition optimization.

1.1.1.1 Droplets formation and driving waveform features

The physics behind droplets formation is still under debate.[14] Some parameters were considered to assess the fenomena, e.g. Reynolds and Onhesorge numbers. For example for a Newtonian fluid (for which the viscous stress is proportional to the strain rate) simulations predict that droplets formation requires Onhesorge number to be comprised between 0.1 and 1. In that range the viscous forces are weak enough to allow the break of the fluid stream and droplets formation, meanwhile strong enough to prevent the formation of satellite secondary droplets. Given that a printability map can be drawn. It's worth to notice that for non-Newtonian fluids these consideration are not valid and there isn't a univocal explanation.

A proper formulation of the ink should also avoid frequent nozzle clogging.

The shape of the driving waveform applied to the piezoelectric transducer strictly affects the fluid ejection and the droplet formation. Usually the combination of positive and negative pulses is adopted to prevent the dripping and to control the amount of ejected fluid. The propelled droplet usually has a hemispherical shape with a tail in its upper part. The tail tends to subdivide itself in satellite droplets. How fast and how much this occurs depends on the fluid rheology. The ink formulation, i.e. solid part concentration and solvents used, and the shape of the driving voltage should be empirically engineered to obtain a stable jet with the wanted amount of ink volume per drop. The stability of the jet is mandatory to achieve an accurate and deterministic printed pattern, otherwise material may be deposited on wrong places and not on the pattern regions.

1.1.1.2 Droplets interaction with substrate and drying process

After droplet ejection it impacts on the substrate and undergoes a phase change to solid through solvent evaporation.[14] The dynamics of this processes is crucial for organic electronics applications because it determines the morphology of the printed material and the shape of the printed pattern. Ink formulation (specifically its evaporation rate and surface tension), printing drop spacing and surface energy of the substrate strongly affect the result obtained. Also temperature, pressure and humidity of the environment can play a role. A careful engineering of these parameters have to be done in order to avoid undesired effects. Here a couple of most known examples.

Line printing The drop spacing has to be chosen in order to print a continuous line merging drops together into a liquid bead. If drop spacing is too large droplets do not coalescence. The reduction of the spacing leads to a situation of initial coalescence where liquid bead shows a periodic irregularity. After sufficient overlap a parallel-sided bead is formed. Further decrease of printing step results in bulging instability.[15] Instabilities and bulging lower the achievable resolution. Being the spread of droplets dependent on the surface energy of the substrate and on the surface tension of the fluid optimal drop spacing has to be found for each ink-substrate couple.

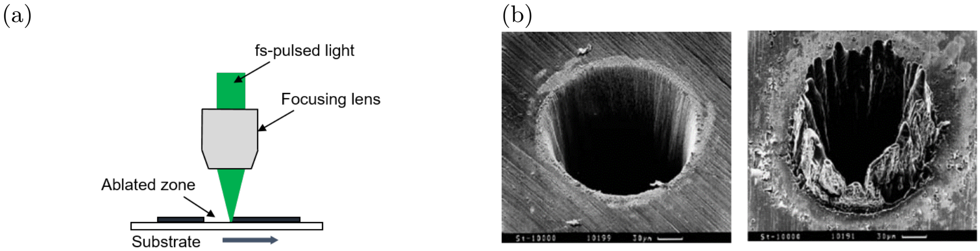

(a) femtosecond ablation (b) nanosecond ablation

Figure 1.3: (a) Scheme of femtosecond laser ablating a matarial deposited on a substrate. (b) Hole realized by femtosecond ablation ($\tau_p = 200fs$ at $780nm$) (left) and nanosecond ablation ($\tau_p = 3.3ns$ at $780nm$) (right) on a steel plate.

Coffee stain effect It was demonstrated that the evaporation rate is higher at the borders than in the middle of a deposited droplet.[16] That is intuitive if one considers that at the sides the surface to volume ratio is maximized. When the contact line is pinned, e.g. because of substrate impurities, a neat flux of fluid will go from the centre to the borders to compensate the evaporated amount of solvent. If the solute is mobile enough it will be transported towards the side of the droplet where it accumulates. At the end of the evaporation process the deposited layer will have a typical ring profile with the central part so thin that pinholes may easily form. There are some strategies to reduce the coffee stain effect. One consist in the reduction of the evaporation rate difference between the centre and the sides by increasing the vapour pressure. Another way is to reduce material accumulation at the border is to slow the material movement by increasing the viscosity of the solution or adding an additive that leads to very fast evaportaion freezing the droplet on the substrate. Alternatively the evaporation driven flux can be counterbalanced with an opposite flux induced by the presence of two solvents with different vapour tensions, namely Marangoni flux.[1] In some cases coffee stain effect was exploited to obtain resolution below the limit imposed by printing technique.[17]

1.1.2 Femtosecond laser ablation

Femtosecond laser ablation is a micromachining process greatly exploited nowadays in medicine and opto-electronics fields.[18–21] It is a non-contact technique that is able to draw digital patterns on a substrate focusing on them light pulses from a femtosecond laser (fig. 1.3a). Progress done in femtosecond lasers improved the quality of products fabricated exploiting this technique. Femtosecond laser ablation makes use of ultrashort laser pulses ($\sim 100fs$) at intensities below the threshold of massive material removal.

While for continuous wave and pico/nanosecond regimes the minimum achievable resolution is of tens microns, for femtosecond ablation it is possible to obtain sub-micrometric features. The latter result is due to the fact that, in fs-regime, the principal light/matter coupling occurs via multiphoton absorption and avalanche ionization which are quicker than thermal transmission and electron-phonon coupling. To remove an atom from a material an energy that overcomes the atom binding energy has to be provided at the system. When electrons are freed by light absorption an electric field is induced by charge separation between them and the ionized atoms. If the electrons energy is above the atom binding energy the electric field becomes high enough to extract the ion from the material with plasma formation. Because multi-photon absortion is very efficient it is possible to work just above plasma threshold. On the contrary, in presence of linear absorption the free-electrons generation is due to thermoionic effect and emission plasma formation is a stocastic process. In order to ablate the material it is necessary to work much above plasma threshold increasing thermal and acoustical destructive effects (fig. 1.3b). With femtosecond laser ablation it is possible to machine selectively one point of the material leaving almost unperturbed the surroundings. A vast range of materials, even dielectrics transparent to visible light, can be ablated with a femtosecond laser going beyond diffraction limit.[22]

1.2 Light detection

Light can either carry a large amount of information when modulated in an electro-optical or photonic circuit, or can reveal specific features of a medium when used as a probe. In both cases, since information handling and storage is so far best accomplished by means of electronic computing, light has to be transduced into an electronic signal. This task is performed by a photodetector (PD). The specific applications of a photodetector vary according to the required sensitivity to light intensity, to the spectral response and to the speed response. The strong impact of photodetectors into nowadays technology can be easily deduced from their wide exploitation in our daily life. Besides being a fundamental building block for light-based telecommunication systems, they can be found in automated building gates and doors, light switches, DVD, blu-ray devices, or in the remote controls of our appliances for instance. The advanced use of light sensors further extend to a vast range of applications in information processing, photonic integrated systems, X-ray medical imaging and spectroscopy, alignment systems, position detection, industrial manufacturing, time and frequency measurements, short range plastic-fiber based transceivers, integrated sensors for Lab-on-a-chip reactors. The advent of Complementary Metal Oxides Semiconductors (CMOS) has enabled the development of image sensors fostering the growth of the rich market for digital cameras and other image sensors and scanners.

So far, the technology development in this field has mostly targeted the device miniaturization, the achievement of an increased responsivity, short time response, low noise and operational voltage and high dynamic range. Inorganic compounds have been playing a major role as active materials for light detection. Silicon is the mostly exploited one, enabling light detection in a wide spectral range going from the visible to the Near-Infrared (NIR), up to $1.1\mu m$. A main limit in silicon detectors technology is due to the relatively low absorption coefficient (e.g. silicon reaches $104cm^{-1}$ at $500nm$) imposing device thickness to be in the order of several microns to reduce transmission losses. For the light detection in the IR region, a quantum efficiency higher than 80% is achieved in GaAs PDs at $840nm$, only if the film thickness is higher than $1.8\mu m$.[23] One of the main strategies employed so far for enhancing photon absorption in PDs is the nanostructuring of the device layers to create waveguiding effects, but still this approach limits the device downscaling, and adds complexity to the fabrication process resulting in an increasing cost for the integrations of those nanopatterned structures into the large scale production of optoelectronic devices.[24]

As an alternative to high vacuum and high temperature techniques so far employed for inorganic materials deposition, solution based strategies, which mainly exploit organic semiconductors and more recently 1-D and 2-D materials, have been developed.[25] The formulation of materials into functional inks allows the fabrication of optoelectronic devices via printing techniques. This enables device fabrication scalability, integration with electronic components at lower production costs and opens the way to large-area applications. Among solution-processable semiconductors, organic conjugated materials quite easily lend themselves to printing, thanks to the possibility of tuning the formulations rheology and therefore of engineering inks for different printing techniques and applications.[12,24,26,27] Their low temperature processing ($< 150°C$) allows the devices fabrication on almost every substrate, rigid and flat as well as flexible and curved, opening the way for the development of non-fragile, conformable electronics.

Not only organic semiconductors allow the solution processability of the fabrication steps, but also their chemical tunability enables high selectivity over a large spectral range which goes from the UV-Vis to the NIR.[28] By a proper design of their molecular structure and thin-film packing motif, the optical bandgap and electronic transport properties can be tuned. Compounds with a highly selective, very narrow spectral response, as well as broad band absorbing materials can be synthesized.[29–31] Nevertheless, charge carrier mobility in organic semiconductors is generally lower than their inorganic counterparts, though recently improved mobility values ($10^{-3} cm^2/Vs$ for bulk transport at low charge density) have been obtained.[32] Importantly, organic semiconductors ensure long carrier lifetime and strong absorption coefficient (up to $105 cm^{-1}$).[33] Such strong absorption enables the use of very thin films ($< 100 nm$ thick), so that carrier transit times can be low despite the limited carrier mobility.[34] It has already been demonstrated that organic photodetectors can operate with bandwidths exciding $10 MHz$ up to $57 MHz$.[35–40]

Hybrid technology, which combines organic and inorganic semiconductors in particular nanowires and nanoparticles, is also very promising.[41] Solution processable inorganic nanoparticles have extended the operational window in terms of spectral response and the possibility to be operated in ambient conditions. For a review of the current studies on solution processable inorganic photodetectors the reader is addressed to previous reports.[42] The electronic structure of inorganic nanoparticles is strongly dependent on their dimension and shape. For a low number of atoms present in the nanoparticles cluster quantized states are observed due to particle size confinement effect. However, their coalescence into large clusters at the solid state has the main effect of removing this quantization and conduction and valence bands start being observed.[43] Quantum dots can be flexibly tailored in composition and size, offering a wide spectral response. Moreover they can be easily synthesized and deposited using high-throughput processes as inkjet printing[44] and spray coating.[45] While current NIR technologies relay on the epitaxial growth of film of inorganic semiconductors onto rigid substrates, quantum dots are so far between those solution processable semiconductors, which can allow light detection into the IR region up to $3 \mu m$[46] and even $5 \mu m$[47]. This can further foster the development in applications like passive night vision, safety sensors, bio-diagnostic and optical communications.[25]

An increasing number of printable organic semiconductors and nanoparticles employed as active materials in photodetectors are being shown in the literature, and this flourishing field is speeding toward scalability and industrial commercialization.

1.2.1 Working mechanism

Among the diverse light detecting devices and concepts which have been developed over decades of research,[48] the most widely exploited scheme is the one where light absorption leads to the generation of separated holes and electrons, which are subsequently collected to opposite electrodes. Such mechanism is typical of inorganic p-n junctions as also of donor-acceptor organic semiconductors.

The basic processes leading to the charge excitation, dissociation and migration to the electrodes are intrinsically dependent on the nature of the active materials (sec. A.4). The physics behind these processes in organic materials has been subject of deep studies in the past and for their specific application in photodetectors fully comprehensive reviews have already been reported. [42,49] A simple sketch of the electronic structure of organic semiconductors can be drawn by knowing the frontier π-orbitals of an isolated molecule, the HOMO and LUMO. A discrete broadening around those levels exists in the solid-state and it is mostly originated by morphological disorder. Importantly, the primary photo-excitation product is typically represented by a strongly bound $(0.1-0.5eV)$ molecular exciton, i.e. a highly localized and neutral state, which at room temperature does not dissociate efficiently into free charges. [50]

The main strategy employed to foster efficient charge dissociation in organic semiconductors has been to intermix donor and acceptor materials in solution, followed by their deposition into films where bulk D-A heterojunctions are formed (sec. A.4.2). By properly engineering the HOMO and LUMO levels of both D and A, excitons which are either photogenerated next to a D/A interface or have diffused there, can dissociate with high yield into electrons and holes. Differently from solar cells, in photodetectors exciton dissociation into free charges and their subsequent transport to the electrodes, can be further promoted by the electric field introduced by an external applied bias (sec. A.4.1). It has to be noted that an external bias results in a current flow due to the injection of carriers from the contacts even in absence of light (sec. A.5). This current, termed dark current, can be minimized by properly selecting the work-function of the contacts. According to the bias polarity a forward and a reverse bias can be distinguished. In forwards bias, a current can be easily injected and typically follows a space-charge limited behaviour. In reverse bias, suitable injection barriers strongly limit carrier injection in the active material (fig. 1.4). [51]

The path followed by those photogenerated charges is different in photodiodes and in photoconductors. In photodiodes excess carriers travel within the two active D and A phases directed towards their respective electrodes were they are finally collected: the holes at the anode and the electrons at the cathode. In photoconductors, one of the two charge carriers, either holes or electrons, is trapped into localized states. This carrier is therefore mostly unavailable for the charge transport, while the opposite carrier is mobile and, once collected, is re-injected at the opposite electrode - provided that contacts are ohmic - in order to maintain charge neutrality.

Although planar structures avoid the need for a transparent electrode and can be easier to realize than the vertical ones, they present a much larger distance between the electrodes (L) which is typically in the range of few to

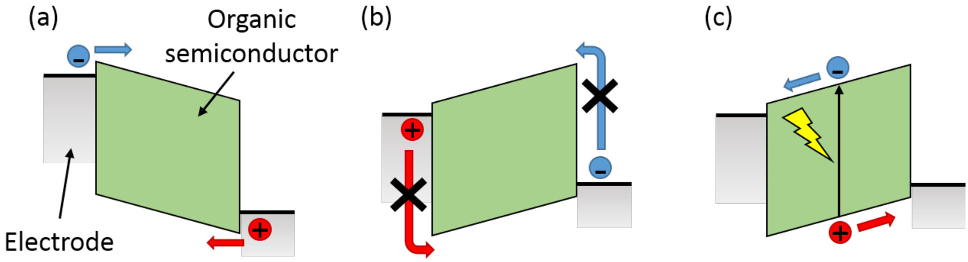

Figure 1.4: Scheme of charge injections from electrodes to demiconductor in direct bias (a) and reverse bias (b). (c) Photogenerated charges are separated and transoprted to the electrodes thanks to the electric field generated by the reverse biass appied to the detector.

tens of micrometers. Such length can drastically increase the carrier transit time, and its downscaling would require high resolution lithographic processes. Scaling of L is instead more easily achieved in a vertical structure, where the distance between the electrodes is defined by the thickness of a solution processed active layer, in the range from few tens to few hundreds of nanometers, providing much faster collection of charges. Both structures can either operate as a photodiode or a photoconductor (fig. 1.5).

In addition to two-terminal devices, also three terminal devices such as field effect transistors (FETs) can be employed as light sensors, typically with the scope of achieving very high responsivity. They are termed phototransistor since the channel conductance can be modulated by photogenerated charges in addition to the field effect exerted by the gate. Their working mechanism has been already described elsewhere.[42,49]

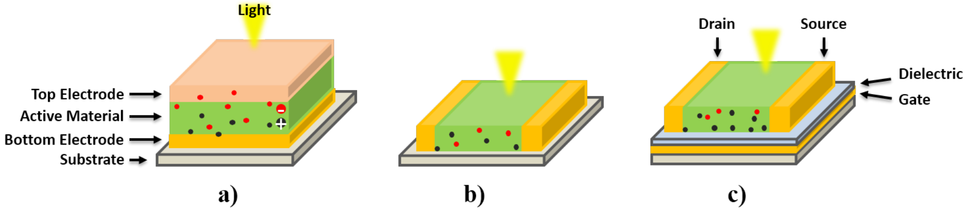

Figure 1.5: Sketches of the most common photodetectors structures: (a) vertical and (b) planar architectures. With the addition of a gate electrode and oxide, the planar structure can be turned into a three terminal photo-transistor device (c).

1.2.2 Figures of merit

Some figures of merit have to be taken into account in order to characterize and compare photodetectors. Here they are concisely highlighted, for a more detailed dissertation we refer to text books.[52,53] The conversion efficiency of impinging photons to photocurrent is measured by the External Quantum Efficiency (EQE) of the detector, given by the ratio between the number of charges collected per second at the electrodes and the number of incident photons per second. Excluding ionizing radiation detectors and avalanche multiplying mechanisms, in photodiodes the maximum quantum efficiency achievable is 100%, since per each photon absorbed the yield of hole-electron charge generation and dissociation cannot be higher than 1. For what concerns ionizing radiation detectors one must take into account that more than one electron-hole couple can be generated per quantum of radiation. In the photoconductive regime more than one charge per photon can flow through the device so that efficiencies can be higher than 100% according to the ratio between the lifetime of the trapped charge and the transit time of the mobile one.

Responsivity ($R, A \cdot W^{-1}$) can be used alternatively to the EQE, the relation among the two being:

$$R = \frac{EQE \cdot \lambda q}{hc} \tag{1.1}$$

where λ is the wavelength of interest, h the Planck constant, c the speed of light, q the elementary charge. R indicates the photocurrent which can be extracted per Watt of impinging radiation, at a specific wavelength. With respect to a plot of EQE vs.λ, the spectral shape of R vs. λ thus tends to favor longer wavelengths, where more photons compose the incoming signal at a specific power. Another important figure of merit to be considered in photodetectors is the ratio between the signal power and the noise power, termed signal to noise ratio (SNR). In order to calculate SNR the main sources of noise must be taken into account, and in particular the dark current shot noise and the photocurrent noise, which lead to a noise spectral density (S_n)

$$S_n = 2q(I_{dk} + I_{ph}) \tag{1.2}$$

where I_{dk} is the dark current and I_{ph} the photocurrent. Even if photocurrent is lower than dark current, a signal can still be detected provided that the root mean square of the fluctuation due to the noise is lower than signal value. In this case dark current shot noise is dominant with respect to the photocurrent one making the latter negligible. Also a frequency dependent noise component, namely flicker noise, could be present. The flicker noise is proportional to the inverse of the photodiode operational frequency. In this case the total amount of noise should be carefully measured in order not to underestimate its value. Specific detectivity (D^*) is usually used to express the capability of the device to detect small signals and it is proportional to the ratio between the responsivity and the noise spectral density. When the dark current is the main source of noise D^* can be written as:

$$D^* = \frac{J_{ph}}{I_{opt}\sqrt{2qJ_{dk}}} \tag{1.3}$$

where I_{opt} is the impinging optical power density and I_{ph} and I_{dk} are respectively the photocurrent density and dark current density. Keeping constant the responsivity (i.e. the ratio I_{ph}/I_{opt}) a photodetector with lower dark current density is able to detect smaller light signals and it has a larger D^*. Photodiodes are typically operated in reverse bias regime to limit dark currents and to improve the signal to noise ratio. Silicon photodetectors are characterized by a D^* above 10^13 Jones in the spectral range between $600nm$ and $1000nm$. In order to evaluate the photodetector speed, its response time is measured as the time in which the current, starting from the dark current value, reaches the steady value after the exposure to light. To be more specific the rise (fall) time is defined as the time needed for the photocurrent to grow(decay) from 10% (90%) to the 90% (10%) of ΔI, where ΔI is the difference between the steady state current upon a rectangular light stimulus and the dark current. In the frequency domain, the relevant figure of merit is the bandwidth, usually defined as the frequency at which the responsivity drops by $3dB$ with respect to its low-frequency value.

Because for photoconductors the efficiency can be higher than 100%, they are also characterized by a photoconductive gain (G), defined as the ratio between transit time of the flowing charge carrier (τ) and recombination time (τ_r).

$$G = \frac{\tau}{\tau_r} \tag{1.4}$$

Since the response time is proportional to the recombination time, there is a trade-off between the photoconductive gain and the response time.

When photodetectors are employed to detect X-rays quanta, the energies of which span from tens of keV to MeV, specific figures of merit exist. Performances of X-ray detectors are expressed in terms of sensitivity and detective quantum efficiency (DQE). The first one is defined as the charge produced by the detector per impinging X-ray quantum at a specified energy. The latter expresses the efficiency in transferring the signal to the output without adding noise to the one intrinsically associated to the Poisson distribution of the impinging quanta; high DQE values indicate that less radiation is needed to achieve the same output SNR. To evaluate X-ray imagers response time, the image lag is often used. It is defined as the ratio between the signal read at a certain time delay after the end of X-ray exposure and the signal read when the imager is exposed to radiation. At a fixed delay time, the smaller is the lag, the faster is the response time. In the case of phototransistors,[54,55] in addition to typical FETs figures of merit, such as mobility and threshold voltage, other figures of merit are used i.e., the photocurrent on/off ratio and responsivity (R_{pt}). The on/off ratio is defined as the ratio between drain current measured when the transistor is exposed to light and the one measured with the transistor kept into dark, while the responsivity of a phototransistor is defined as follows:

$$R_{pt} = \frac{J_{ph}}{I_{opt}} = \frac{J_{d,ph} - J_{d,dk}}{I_{opt}} \tag{1.5}$$

where$J_{d,ph}$ is the drain current density under illumination and $J_{d,dk}$ is the drain dark current density.

A summary of the main figures of merit reported above are reported in table 1.1

1.3 State of the art of inkjet printed photodetectors

The most common donor-acceptor blend employed in organic photodetectors is based on a mixture of poly(3-hexylthiophene) (P3HT) and [6]-phenyl C_{61} butyric acid methyl ester (PCBM), due to the extensive studies already performed on this blend in the photovoltaics field. Though the P3HT:PCBM blend is the most commonly employed to provide a proof of concept of the device fabrication feasibility, other photoactive materials are being explored to extend the optical window of inkjet printed photodetectors. We can find demonstration of photodetectors based on nanocrystals, J-aggregated cyanine dyes, graphene and polymeric blends.[45]

1.3.1 P3HT:PCBM based inkjet printed photodetectors

A first example of inkjet-printing of a P3HT:PCBM blend as photoactive layer in vertical photodetectors is shown by Lilliu et al.[56] The device structure featured a stack of glass/indium-thin-oxide (ITO) and spincoated poly(3,4-ethylenedioxythiophene) poly(styrenesulfonate) (PEDOT:PSS) as bottom electrode, a printed P3HT:PCBM blend, and evaporated calcium and silver as top electrode. They showed a responsivity of $0.32A \cdot W^{-1}$, corresponding to 63% EQE (fig. 1.6), and $D^* = 8 \cdot 10^{11}$Jones (at $5V$ in reverse bias).

Quantity	Symbol/Acronym	Unit	Definition/Physical meaning
Dark current	I_{dk}	A	Current flowing in absence of illumination
Photocurrent	I_{ph}	A	Current flowing under illumination
External quantum efficiency	EQE	—	Ratio between the number of collected charge carriers and the number of incident photons per second
Responsivity	R	$\mathrm{A\,W^{-1}}$	Ratio between the photocurrent and the optical power impinging on the device
Rise (fall) time	τ	s	Rise (fall) time is the time needed for the photocurrent to grow(decay) from 10% (90%) to the 90% (10%) of ΔI, where ΔI is the difference between the steady state current upon a rectangular light stimulus and the dark current.
Bandwidth	BW	Hz	Frequency at which responsivity drops by 3 dB with respect to low frequency value
Signal to noise ratio	SNR	—	Power ratio between the signal and the noise of the detector
Specific detectivity	D^*	$\frac{\mathrm{cm}\sqrt{\mathrm{Hz}}}{\mathrm{W}}$ (Jones)	Measure of the capability of the device to detect small signals. It is used to compare sensitivity of different detectors
Photoconductive gain	G	—	Ratio between transit time of the flowing charge carrier and recombination time
Photransistor on/off ratio	On/Off	—	Ratio between drain current measured when the transistor is exposed to light and the one measured with the transistor kept into dark
Phototransistor responsivity	R_{pt}	$\mathrm{A\,W^{-1}}$	Ratio between the variation of current in the channel upon illumination and impinging optical power
Figure of merit for x-ray detectors and imagers			
Sensitivity	S	$\frac{\mathrm{C}}{\mathrm{R\,cm^2}}$ R = (Roentgen)	The charge produced by the detector per impinging x-ray quantum at a specified energy
Detective quantum efficiency	DQE	—	Expresses the efficiency in transferring the signal to the output without adding noise to the one intrinsically associated to the Poisson distribution of the impinging quanta
Image lag	—	s	Ratio between the signal read at a certain time delay after the end of x-ray exposure and the signal read when the imager is exposed to radiation

Table 1.1: Figure of merit of photdetectors and phototransistors.

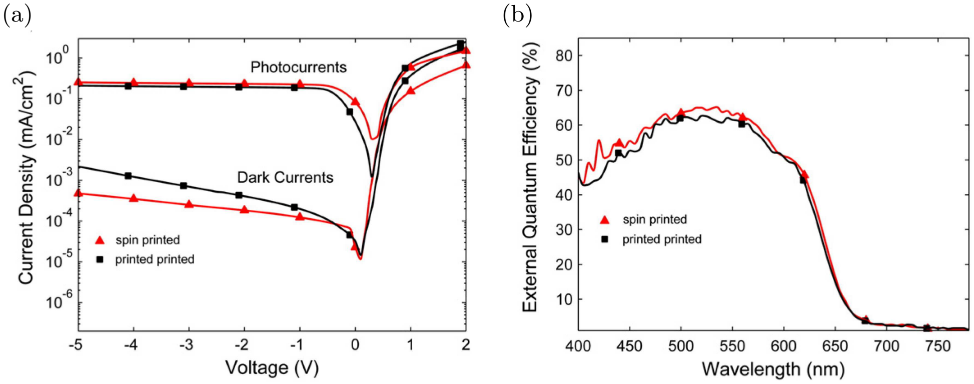

Figure 1.6: Comparison of the electrical characteristics and spectra sensitivity of OPDs fabricated with different layer deposition techniques by Lilliu et al.[56] (a) I-V measurements of dark currents and photocurrents. (b) EQE measurements. Note: “spin-printed” refers to the techniques used to fabricate the hole conducting and the bulk heterojunction layer, respectively.

In the same work, the authors replaced the spincoated PEDOT:PSS layer with an inkjet printed one, though it showed slightly worse characteristics ($R = 0.27A \cdot W^{-1}$, $D^* = 3.4 \cdot 10^{11}$Jones). Similarly, by changing the top electrode with an evaporated aluminum contact, Wojciechowski et al., realized a photodetector capable of working at low reverse bias ($100mV$) with a R of $0.25A \cdot W^{-1}$ (at $532nm$) and high $D^* = 1.4 \cdot 10^{13}$Jones.[57] This device was successfully integrated into a miniaturized biosensor.

Printing methods not only allow the printing of the active materials but also of the electrodes, paving the way for the fabrication of all inkjet-printed photodetectors. The first example was published by Lavery et al.[58] who succeeded in stacking silver nanoparticles (bottom electrode), a $\sim 1\mu m$ thick blend of poly(9,9’-dioctylfluorinene-co-bis-N,N’-(4-butylphenyl)-bis-N,N’-phenyl-1,4-phenylenediamine) (PFB) and poly(9,9’-dioctylfluorene-co-benzothiadiazole) (F8BT) as active material and PEDOT:PSS as top electrode, depositing each layer by inkjet printing. A fluorosurfactant was added to PEDOT:PSS ink in order to allow the printing of PEDOT:PSS directly on top of the blend otherwise affected by dewetting phenomena. The photosensor was developed to work at high luminance ($\sim 100to400 \cdot 10^3 lux$) and showed an EQE peak of 5.9% at $400nm$, dark current density of $1nA \cdot cm^{-2}$ and $D^* = 1 \cdot 10^{12}$Jones (at $1V$ reverse bias).

1.3.2 Inkjet printed photodetectors based on other photoactive materials

HgTe-nanocrystals (NC) resulted as good candidates due to their response in the far and near IR and their long time stability in films. HgTe-NC dispersed in chlorobenzene form an inkjet printable solution suitable for fabrication of photodetectors. By printing this ink on interdigitated Ti/Au electrodes, Boberl et al.[45] achieved a maximum $D^* = 3.2 \cdot 10^{10}$Jones, under $1nW$ of illumination at $1.4\mu m$. By changing NC size, the responsivity spectrum can be tuned, allowing the extension of the device response up to $3\mu m$. Wu et al.[59] presented a thin film NC photodetector printed on paper with an office inkjet printer.

Yang et al.,[60] incorporated three different cyanine dyes into PEDOT:PSS to form a solution ink which was printed on top of an ITO substrate. A thin Al layer was evaporated on the PEDOT:PSS-dye blend. The red-shifted and sharp absorption spectra indicated the formation of dye's J-aggregates dispersed into the PEDOT:PSS matrix. The open-circuit voltage measurements showed a change when the light probe wavelength was around the dye absorption peak, demonstrating the possibility to detect light signals emitted from a solid-state laser. Though examples of printed organic solar cells can be found in the previous literature,[61] this work represented a first example of an inkjet printed photodetector operating on a flexible polyethylene terephthalate (PET) substrate.

A titanium (IV) bis(ammonium lactate) dihydroxide (TBA) and graphene oxide (GO) nanosheets ionic solution was formulated and inkjet-printed on coplanar graphene-based electrodes, realizing a planar photodetector by Manga et al.[62] This ink overcomes the issues related to poor solubility of GO in ethanol based solutions and the rapid hydrolysis of titanate by aqueous solutions, while having a proper viscosity to allow inkjet printing. Sintering of the composite was obtained by thermal annealing. The resulting device showed a peak EQE of 85% and $D^* = 2.33 \cdot 10^{12}$Jones around $325nm$. The detector was also responsive in the visible region up to $750nm$ but with D^* quickly decreasing for wavelength longer than $375nm$ to values lower than 10^{12}Jones.

In the literature inkjet has been explored also to fabricate all-printed detectors with inorganic active layers and carbon based electrodes. An example is given by Finn et al.[63] who fabricated a planar all inkjet-printed photoconductor by using a dispersion of N-methyl pyrrolidone (NMP) exfoliated MoS_2 nanosheets as photoactive semiconductor and NMP-exfoliated graphene for the interdigitated contacts. The detector, fabricated at temperatures below $70°C$ on a commercial PET substrate, showed a 10-fold current increase when exposed to $640mW \cdot cm^{-2}$ incident illumination.

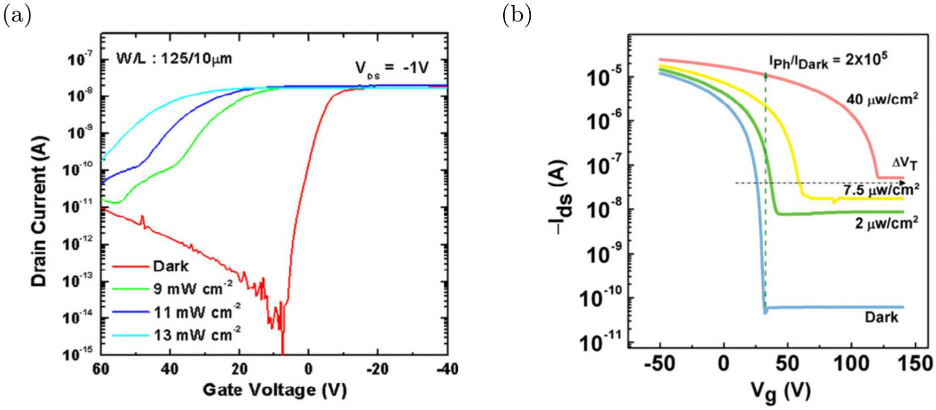

Figure 1.7: (a) The transfer characteristics of a printed TIPs-pentacene phototransistor with a steady-state light illumination (at $V_{DS} = -1V$). The light power density was varied as 9, 11, $13 W \cdot cm^{-2}$; channel length of $10\mu m$ and width of $125\mu m$. (b) Transfer characteristics of the PDPPTzBT transistor under illumination compared with dark transfer curve.[17]

1.3.3 Inkjet printed phototransistors

In the following we will describe a few examples where inkjet printing has been adopted for the fabrication of organic semiconductors phototransistors.

A film of 6,13-bis(triisopropylsilylethynyl) (TIPS) pentacene was deposited by inkjet printing as the semiconducting material in phototransistors based on a suspended top-source and drain contacts structure (with a channel length of $10\mu m$ and a width of $125\mu m$)[64]. Under a steady-state white light intensity between 9 and $13 mW cm^{-2}$, the phototransistor produced a photocurrent over dark current ratio exceeding 10^6 and $R = 0.11 A \cdot W^{-1}$ at $-10V$ of gate voltage and $1V$ of drain-source polarization (fig. 1.7a).

Polymer phototransistors have also been realized by inkjet printing a diketopyrrolopyrrole-thiazolothiazole copolymer (PDPPTzBT) over a bottom gate bottom contact structure, where also a short-channel ($0.7\mu m$) was patterned by inkjet-printing.[17] To obtain such a short channel poly(methylmethacrylate) (PMMA) resist was spin-coated and patterned by inkjet printing pure solvent. Through the reduction of inter-droplet interval, a sub-micron width line of PMMA. Subsequently adhesion layer and gold were deposited. Lift-off of PMMA leaves a short-channel gap, corresponding to PMMA-ridge, between gold electrodes. Such devices showed very high responsivity ($10^6 A \cdot W^{-1}$) under weak illumination intensity ($700 nW \cdot cm^{-2}$ at $650 nm$ of wavelength, fig. 1.7b). Upon irradiation, the drain current of the phototransistor increased within $1s$. However, when the light was turned off the drain current was not decaying to the off value but remained in a steady state for at least 10000 s

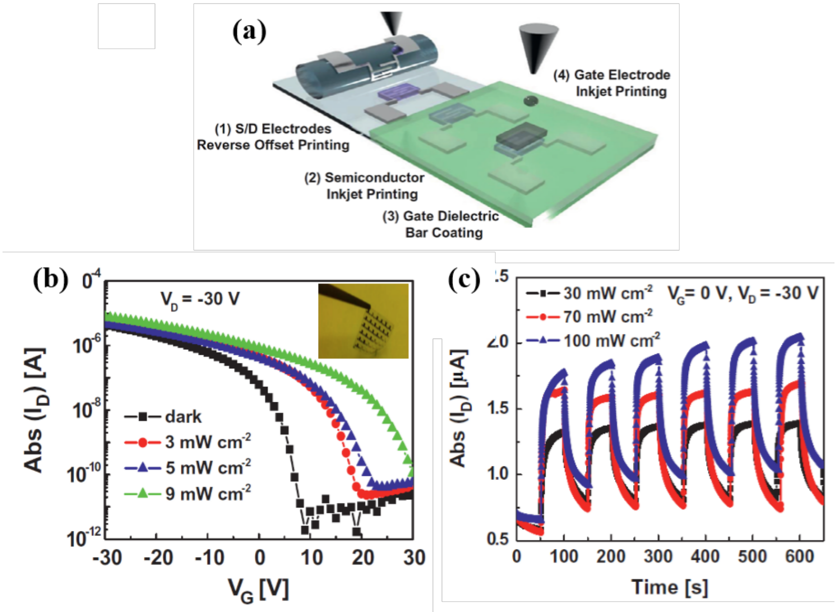

Figure 1.8: (a) Schematic of the combination of printing methods employed for the organic phototransistor fabrication; (b) transfer characteristics in the dark and under illumination at different light intensity at $V_D = 30V$ (inset: photograph of devices on flexible substrate); (c) Time-resolved photo-response characteristics upon different irradiation ($V_G = 0V$ and $V_D = 30V$).[65]

showing a light triggered memory effect.

Recently, Kim et al.[65] reported all-printed phototransistors where inkjet was adopted to pattern the organic semiconductor and the gate electrode. In this work, the authors showed a combination of printing methods to the purpose of applying the most ideal printing technology to the desired pattern and solution formulation: besides inkjet, they adopted reverse offset printing,[66] which allows for a higher lateral resolution, to pattern source and drain electrodes with a channel length of $20\mu m$ and channel width of $1000\mu m$; a simple bar-coating technique was instead adopted to achieve a uniform blank deposition of a polymeric dielectric (fig. 1.8).[67] The all printed phototransistors showed a responsivity of $0.11 A \cdot W^{-1}$ ($V_G = -10V$ and $V_D = 1V$).

Different inorganic light sensitive materials have been adopted to develop phototransistors with inkjet printed active layers, comprising indium doped zinc oxide (IZO)[68] and MoS_2,[69] both exhibiting a photoresponse in the UV region. IZO-FET showed a current modulation of four orders of magnitude in the steady state and when exposed to a UV light pulse and showed turn-on and turn-off times of $5ms$ and $10ms$ respectively.

A blend of carbon nanotubes and nanocrystal particles was employed as hybrid active layer for the fabrication of an organic phototransistor. Carbon nanotubes were deposited via inkjet printing, while NCs were absorbed by dipping the printed substrates in a dispersion of cadmium telluride (CdTe).[70] While the device was exposed to light, the drain-source voltage variations were measured keeping constant the drain current at $1mA$. The ratio between voltage variation and impinging power was found to be $20mV \cdot W^{-1}$ and $15mV \cdot W^{-1}$ for a phototransistor with and without NCs respectively.

The examples reported so far confirm the very promising use of the inkjet printing in the realization of photodetectors, allowing the achievement of good electro-optical properties comparable with other non-printing and conventional techniques, such as vacuum evaporation and spin coating. The versatility of this technique stands out clearly from the reported examples where different materials, structures and patterns were used after a proper formulation of the ink. Further developments of the technique should face the improvement in fabrication yield, resolution and throughput, to the purpose of fostering its wider exploitation into electronic industry.

1.3.4 Outlook

Solution processable organic and inorganic semiconductors allow combining the advantages related to their peculiar physical chemistry with the ease of processability, enabling the preparation of printable inks and therefore the exploitation of printing technologies for the fabrication of large-area, printed, opto-electronic systems. The possibility to tailor their optical and electrical response by chemical design can give access to applications currently precluded or hardly addressable by standard inorganic detectors. The low production costs and the use of chemical synthesis methods to produce large amount of active materials, especially for the case of carbon based inks, make printed photodetectors highly competitive. As an example, current inorganic electronics based on CMOS chips is generally still too expensive for disposable components.

Solution processed semiconductors can be printed on a wide variety of substrates, including ultra-thin substrates, fostering the development of conformable electronics. Therefore there is a consistent industrial effort to the development of printing technologies to produce low cost, flexible, light weight photodetector arrays. New large area conformable organic image sensors on plastic and transparent backplanes, fabricated combining printed OPD with a plastic organic transistor backplane, have been already demonstrated (flexible sensor with a $4 \times 4cm^2$ active area, $175\mu m$ pixel size, $375\mu m$ pitch and

$94 \times 95 = 8930$ pixel resolutions).[71]

While printed photodetectors are comparable to the non-printed ones, both organic and inorganic, in terms of responsivity and EQE, their operating speed doesn't exceed $1MHz$. These results point out that there is still more optimization to be done to reach at least the higher values reported for the organic non-printed counterpart.[36–40]

Also in most of the works presented on printed OPDs, D^* was extrapolated by assuming that the dominant contribution to the noise was uniquely arising from the dark current shot noise. There are only limited reports of actual measurements of the real noise in photodetectors required for the proper estimation of their detectivity.[45,72,73] In particular flicker noise (frequency dependent noise) is likely to be dominant for low frequency applications and so this aspect should be investigated in a deeper way in order to make a more reliable characterization of the device performances. Another issue which has still to be addressed is related to the uniformity of printed electronic devices and the yield of production over large areas. For many application a strict requirement which has yet to be fulfilled, is the further downscaling of device's pattern to enable the integration into more complex electronic arrays, a challenge that is being currently investigated. Also it is essential to assess and improve the stability of the printed materials, in particular their possible degradation upon exposure to ambient conditions. If such limitations are successfully overcome, in the near future we may witness the adoption of printed photodetectors in a large range of new applications such as digital image sensing,[73] smart packaging and sensors for medical equipment and biomedical diagnostics,[74] security and mobile electronics commerce.

Part I

Direct-Writing Organic Devices: Towards Passive Pixels for Plastic Large-Area Imagers

Chapter 2

Inkjet printed P3HT-based photodetectors

In this chapter the realization of inkjet printed detectors will be presented. We developed fully-inkjet printed and semitransparent photodetectors which can be easily integrated with other optoelectronic components. Aiming for integrability and reverse dark current reduction the first prototype was modified. Going through the fabrication and the characterization of different structures of inkjet printed photodetectors it will be shown that the bottom electrode and its functionalization play important role in determining the photodetector performances. In the last part devices features are compared and perspective of future studies outlined.

2.1 Introduction

Solution processability, chemically tailorable properties, abundance of primary materials, mechanical flexibility are key features offered by organic semiconductors that can be exploited to develop innovative devices.[75] Functional inks made with organic materials are suitable to be printed by mean of additive, cost-effective, scalable techniques (e.g. roll-to-roll, inkjet printing, screen printing, spray coating) paving the way to large-area, distributed, complex optoelectronic systems.[24,76] Among the others inkjet printing has the advantage to transfer a digital pattern image directly and without contact on a variety of substrates easily allowing customization.[77] In the field of light sensing some examples of printed photodetectors with interesting performances were reported (sec. 1.3), but only few examples are meant for integration with other optoelectronic devices.

Here we report the realization of fully-printed, all-organic photodetectors for digital imaging applications and X-ray indirect sensing (chap. 3). Lightweight and flexibility foster us to choose polyethylene naphthalate (PEN) as substrate. Through inkjet printing the fabrication exploits a layer-by-layer deposition approach. Functional materials were precisely placed on the substrate with a resolution of tens of μm.

2.2 Fabrication

Every inkjet printed layer, apart from the photoactive blend one, was realized using Fujifilm Dimatix DMP2831 with $10pL$ LCP nozzles cartridge loaded with a properly formulated ink. Microfab JETLAB 4 equipped with a $40\mu m$ diameter DLC nozzle was used to inkjet print the blend.

The devices have a vertical topology with the photoactive layer sandwiched between two conductive stripes.

PEN purchased from DuPont was used as substrate after rinsing with acetone and isopropyl alcohol (IPA). We make use of commercially available conductive inks to fabricate the electrodes. Three conductive inks were tested for bottom electrode realization: TEC-IJ-010 (InkTec), CCI-300 (Cabot) and Clevios P JET 700 N (Hereaus). The first two are silver based inks and were filtered with a $0.2\mu m$ PTFE filter before loading the cartridge while the third is PEDOT:PSS based, filtered with $0.2\mu m$ PVDF filter. Moreover another formulation of CCI-300 was tried further diluting it with ethanol and ethylene glycol $(1 : 0.3 : 0.7)$, filtered with $0.2\mu m$ PTFE filter. Silver electrodes require a sintering step to become conductive: TEC-IJ-010 at $130°C$ for $10min$ and CCI-300 at $70°C$ for $10min$ followed by $50min$ at $130°C$; everyone is performed in air. A number of annealing temperatures and times were explored. The P JET 700 N was backed in air at $100°C$ for $10min$.

As second step a functionalization of the bottom electrode is performed spincoating polyethylenimine ethoxylated (PEIE) (Sigma Aldrich), polyethylenimine branched (PEI) (Sigma Aldrich) or poly[(9,9-bis(3'-(N,N-dimethylamino)propyl)-2,7-fluorene)-alt-2,7-(9,9-dioctylfluorene)], namely PFN, (Ossila). PEIE solution was prepared according to reference[78] and spincoated over the substrates at $5000rpm$ for $1min$ $(1000rpm/s)$. Then the samples were heated up to $100°C$ for $10min$ and rinsed in deionized water for $1min$. For devices with PEDOT:PSS bottom electrode this last step was skipped. PEI was diluted in 2-methoxyethanol to $0.1wt.\%$ concentration and spin-coated over the bottom contacts for $1min$ at $5000rpm$ $(1000rpm/s)$. PFN was dissolved in a mixture of methanol $(99.6vol.\%)$ and acetic acid $(0.4vol.\%\ )$ to obtain a $1mg \cdot mL^{-1}$ solution which was filtered with a $0.2\mu m$ PVDF filter and deposited by spincoating at $2500rpm$ for $1min$ with an acceleration of $1000rpm/s$. PFN was also formulated in a printable ink dissolved at $1mg \cdot mL^{-1}$ in a solution of water, isopropyl alcohol, ethilene glycol $(1:1:0.2)$ to which was added $0.4vol.\%$ of acetic acid. After being filtered with a $0.2\mu m$ PVDF filter it was deposited with the DMP2831 on the electrode.

P3HT ($RR = 96.6\%$, $Mw = 65500$) was purchased from Merck, and $PC_{61}BM$ (purity $> 99.5\%$) was purchased from Solenne, and they were both used as received. A blend solution of P3HT:$PC_{61}BM$ (1:1) at $30mg \cdot mL^{-1}$ was obtained by mixing 1,2-dichlorobenzene ($68vol\%$) and mesitylene ($32vol\%$), both purchased from Sigma Aldrich. The blend was stirred overnight, then heated at $80°C$ for $10min$ and filtered with a $0.2\mu m$ PTFE filter before printing.

Zonyl FS-300 fluorosurfactant was added to Clevios P JET 700 N ($10wt\%$). The solution was heated up to $80°C$ for $10min$ and filtered with a $0.2\mu m$ PVDF filter before loading the cartridge. It was used to print the top electrode.

After the last deposition samples were moved inside a nitrogen filled glovebox and annealed at $100°C$ for $1h$.

We carried out every deposition in ambient conditions with UV-filtered light. Layers profile was measured by stylus profilometry (KLA Tencor Alpha-Step IQ). In order to measure organic layers absorbance, stripes made of PEDOT:PSS only and of P3HT:PCBM only were printed on PEN and their transmittance was measured with a Varian Cary 50 Spectrophotometer. Absorbance of P3HT:PCBM in the actual device was estimated taking into account the different thickness of the blend layer printed on PEN ($200nm$) and on Ag stripe ($120nm$). Atomic Force Microscopy (AFM) images were acquired with an Agilent 5500 microscope. I-V in dark and under white light ($6400K$, about $3mW \cdot cm^{-2}$) and EQE measurements were performed in glovebox; where specified optoelectronic characterizations were performed in vacuum ($5 \cdot 10^{-6}mbar$). I-V curves were acquired with an Agilent B1500A Semiconductor Parameter Analyzer; EQE spectrum was measured at an incident power density of about $1mW \cdot cm^{-2}$ with a custom setup. The cathode was biased at positive voltage while the anode was connected to the virtual ground of a DHPCA-100 transimpidance amplifier by means of a probe station. The gain of the pre-amplifier was set in order to maximize the signal without incur in saturation (bandwidth $1MHz$). The output was sent to a Tektronix MSO2014 oscilloscope. A series of LEDs with different emission peaks was driven by an Agilent 81150A waveform generator and optically coupled to the pixel by means of a plastic optical fibre ($2mm$ diameter, 02-551 Edmund Optics) placed $2.5mm$ away from the substrate. Impinging optical power was measured with a BPX-65 (Osram) silicon photodetector and used to calculate photocurrent and EQE. Response time was measured on photocurrent decay

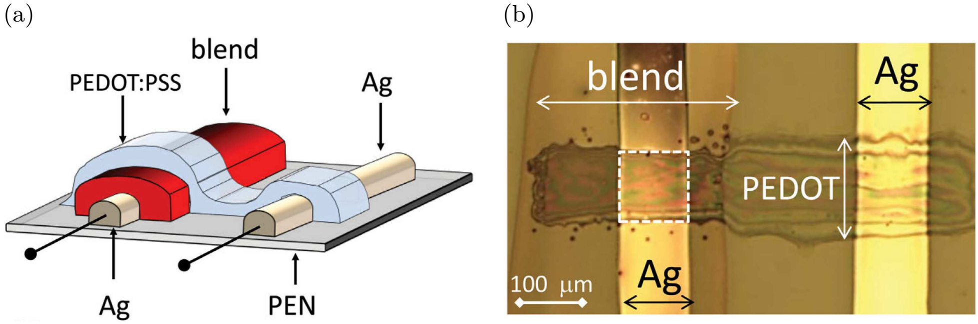

Figure 2.1: (a) Sketch of the inkjet printed photodetector. To minimize resistive losses, electrical contact to PEDOT:PSS layer is taken by means of an additional Ag stripe. (b) Optical micrograph of a printed device: vertical Ag stripes are $113\mu m$ wide; the horizontal stripe is PEDOT:PSS; on left the blend stripe is visible. The overlap between Ag stripe under the blend layer and PEDOT:PSS stripe defines the device active area (dashed square).

waveforms. Frequency measurements were acquired by means of an Agilent E5061B network analyser which provided also the small signal sinusoidal stimulation superimposed on LED bias.

2.3 Characterization

Aiming at large-area imaging applications in the field of visible light or X-ray digital imagers, at first we focused on devices with an active area of about $100 \cdot 100\mu m^2$.[79–81] A top illuminated architecture, where silver is the bottom electrode (TEC-IJ-010) and the semi-transparent PEDOT:PSS is the top electrode (fig. 2.1), was firstly tested and deeply analysed. This choice was taken to avoid the interaction of the solvent present in the silver-based ink formulation with the active layer that could be damaged.[82] As photoactive layer we chose the very well-known blend of P3HT and PC$_{61}$BM, which represents a good model bulk heterojunction and showed no degradation when exposed to high X-ray dose in previous studies.[83,84]

2.3.1 TEC-IJ-010 and PEIE based device

The printing of the Ag-based bottom contact onto the PEN substrates was optimized by tuning the voltage waveform at the piezo head and the distance between the deposited droplets. We obtained well controlled printed stripes, $110\mu m$ large on average, about $80nm$ thick, with scallope-free edges and a sheet resistance as low as $5\Omega/\square$. On top of the Ag contact PEIE was deposited in order to tailor the Ag energetics. Without PEIE, we found that the

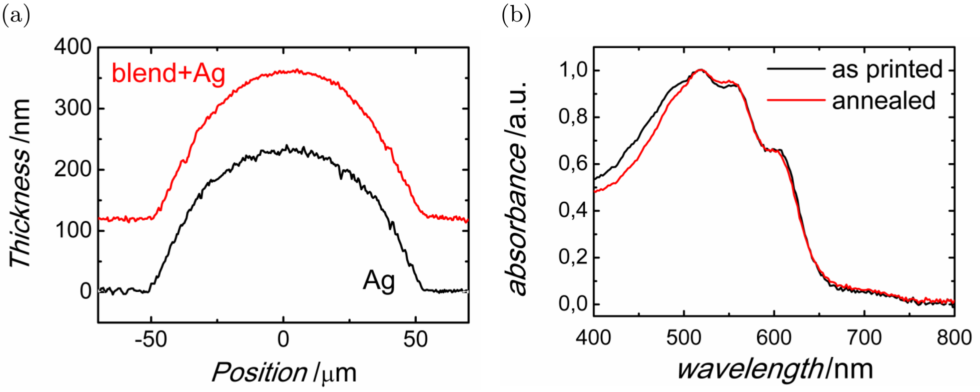

Figure 2.2: (a) Stylus profilometry of an Ag stripe and of P3HT:PC$_{61}$BM active layer deposited onto the Ag stripe. The blend average thickness is of 120nm. (b) Normalized absorbance spectra for P3HT:PC$_{61}$BM printed on PEN; as printed (black line) and after thermal annealing at 120°C for 1 hour (red line). Upon thermal annealing no sizeable change in the spectra shape, at least in the region of wavelengths $> 500nm$.

external voltage polarity to achieve forward or reverse biasing of the device was unpredictable, and that the open circuit voltage (V_{OC}) was very small, in the range of few tens of mV. We ascribe this behaviour to the fact that, generally speaking, Ag work function (W_f) can increase by $0.6 - 1.0eV$ with respect to its nominal value of $4.26eV$ due to oxygen chemisorption,[85] thus becoming close to the W_f of PEDOT:PSS (about $5.0eV$). Thanks to PEIE treatment, effective in reducing the silver W_f, the device polarity was made reproducible, with the Ag contact properly acting as electron collecting contact when positively biased with respect to PEDOT:PSS.

As to the P3HT:PC$_{61}$BM blend, we adopted an ink formulation suitable for inkjet printing. It is well known that inks based on a single solvent often lead to highly non-uniform films, much thicker at the periphery than in the centre (coffee stain effect sec. 1.1.1.2). To solve this issue, we adopted the strategy of mixing two suitable solvents to exploit the Marangoni effect,[12,86,87] in order to counterbalance the solute migration towards the droplet borders with a surface tension gradient. Following ref.[11] we selected 1,2-dichlorobenzene and mesytilene as the two solvents for the blend. After optimizing the blend concentration (20, 24 and $30mg \cdot mL^{-1}$), we chose $30mg \cdot mL^{-1}$ as the one yielding the best device performance.[88] We were able to print stripes fully covering the silver lines (necessary to avoid short circuits between electrodes), with an average thickness of about 120nm and a coffee stain free profile (fig. 2.2a). Looking at the absorbance spectral shape and focusing on the region where P3HT dominates the absorption ($450nm - 650nm$), we observe the presence

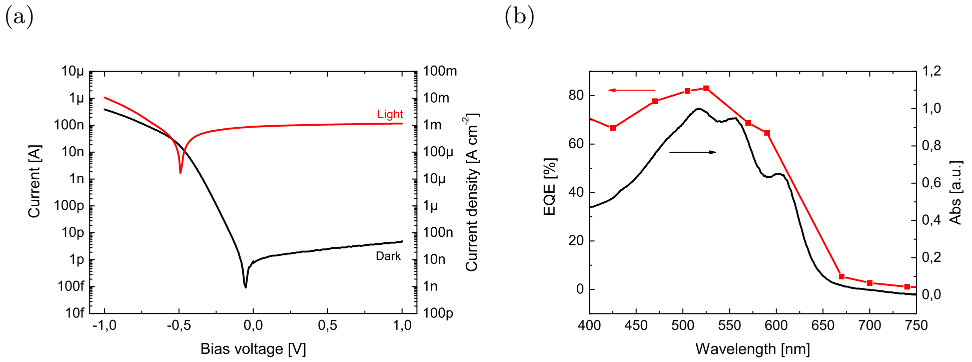

Figure 2.3: (a) Photodetector dark current (black line) and photocurrent (red line, incident power density $3mW \cdot cm^{-2}$). (b) EQE spectrum (squares) measured at $0.9V$ reverse bias under an incident power density of $10mW \cdot cm^{-2}$ and normalized active layer absorbance (black solid line).

of a well-developed shoulder at $610nm$ (fig. 2.2b), suggesting the presence of ordered regions of P3HT,[89] likely due to the use of a large fraction of a relatively high boiling point solvent in the ink formulation (1,2-dichlorobenzene boils at $180.5°C$).[90] For the deposition of the top semi-transparent electrode we adopted a highly conductive inkjet formulation based on PEDOT:PSS (Clevios P JET 700 N). The high hydrophobicity of the underlying blend layer prevented a reliable printing due to wettability issues. Since treating the blend surface by means of oxygen plasma as suggested in the literature[91] resulted in short-circuited devices, we modified the ink formulation by adding a fluorosurfactant (Zonyl FS-300), similarly to what previously done in ref.[58]. After tuning the weight percentage of Zonyl, we found that $10wt.\%$ allowed to obtain a good coverage of the blend area. The device active area (about $9000\mu m^2$ on average) was defined by the overlap between the mutually orthogonal silver stripe and PEDOT:PSS stripe. This latter was kept short (less than 10 squares) to avoid sizeable ohmic drops. A sketch of the device and an optical micrograph are reported in fig. 2.1. The sheet resistance is of $3k\Omega/\square$ on average and the transparency in excess of 98% (at $570nm$).

We obtained working devices with good yield, maintaining the incidence of faulty devices (because short circuited or because of erratic electrical behaviour) relatively low (about 15% over about 100 devices realized and measured). This suggests that in the majority of cases the printed blend layer is uniform enough to avoid the formation of direct contacts between Ag and PEDOT:PSS. The dark current and the photocurrent of a printed device are shown in fig. 2.3a. The dark current density is in the range of a few hundreds of $nA \cdot cm^{-2}$, whereas the rectification ratio (viz. the ratio between the for-

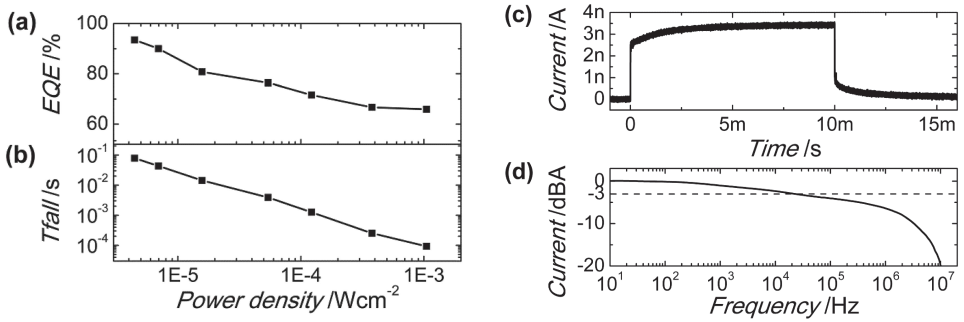

Figure 2.4: EQE (a) and t_{Fall} (b) as function of the incident power density (measured at $570nm$, at $1V$ applied bias). (c) Photocurrent response to a $10ms$ light pulse at $570nm$ with an incident power density equal to $0.1mW \cdot cm^{-2}$ ($1V$ applied bias). (d) Device bandwidth measured at $570nm$ at an incident power density of $0.1mW \cdot cm^{-2}$ ($1V$ applied bias). Measured in vacuum.

ward and the reverse dark currents) is close to $5 \cdot 10^4$ at $1V$: both figures of merit are comparable to what is reported in the literature for P3HT:PC$_{61}$BM spin-coated photodiodes with an inverted architecture.[92] The final thermal annealing is needed to achieve devices working properly: as-printed devices are characterized by exceedingly large dark currents resulting in a poor ratio between photocurrent and dark current (below 10), but after annealing at $100°C$ for 1 hour the dark current is largely suppressed and the photocurrent to dark current ratio is increased up to 3 orders of magnitude on average. Increasing annealing time or temperature (above $120°C$) rises reverse dark current and makes the devices prone to short-circuting themselves. In fig. 2b we report the External Quantum Efficiency (EQE) spectrum: the EQE exceeds 60% over a broad wavelength range up to $\sim 600nm$, with a peak of 83% at $525nm$. Not only is the EQE remarkable for a completely printed photodetector, largely exceeding the only previous example reported in the literature,[91] but also it is among the best performing P3HT:PC$_{61}$BM photodetectors, irrespective of the deposition technique.[92–96] The EQE values perfectly fit into the requirements for an X-ray imager (sec. 3.2.4). The device specific detectivity is around $10^{12} cm \cdot Hz^{0.5} \cdot W^{-1}$, comparable to the literature on inverted P3HT:PC$_{61}$BM spin-coated photodiodes.[92] We measured the EQE by varying the incident power density P (over a range of about three decades) and we found a very weak dependence on P (EQE $\propto P^{-0.065}$), as shown in fig. 2.4a: this rules out the space charge limited photocurrent regime (which is predicted to give EQE $\propto P^{-0.75}$) and suggests an almost balanced transport.[97]

As to the speed of response, we tested the device with a $1ms$ light pulse

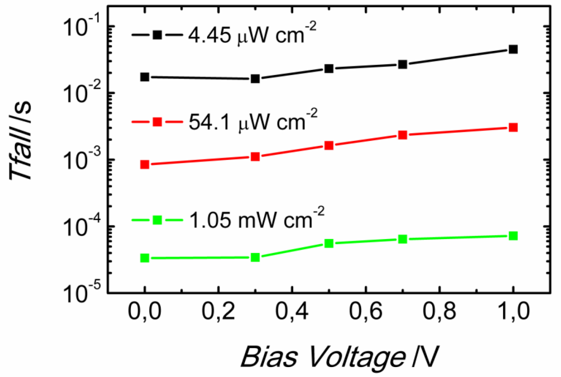

Figure 2.5: Dependence of t_{Fall} on applied bias voltage. Incident power density: $4.45\mu W \cdot cm^{-2}$ black line, $54.1\mu W \cdot cm^{-2}$ red line, $1.05mW \cdot cm^{-2}$ green line. Measured in vacuum.

at $570nm$ (fig. 2.4c). Looking at the photocurrent transient after switching off of the optical stimulus, we recorded a first fast decay of few μs during which the photocurrent drops by 64%, followed by a slower tail. Overall, the $90\% - 10\%$ photocurrent fall time (t_{Fall}) is of about $100\mu s$ (fig. 2.4b). The simultaneous presence of a fast dynamics and of a slow one in the time domain, in the frequency domain gives rise to a $-3dB$ bandwidth of about $20kHz$, followed by a slowly decreasing response ($-2dB/dec$), and a significant fall only at about $1MHz$ (fig. 2.4d). To investigate more in depth the device speed, we measured t_{Fall} (at $570nm$) varying the applied voltage V_{Bias} and the incident power density P (fig. 2.4b). t_{Fall} is almost independent of $Vbias$ (fig. 2.5): this rules out the transit time of photogenerated carriers as the leading mechanism affecting the device speed. On the contrary, a strong dependence of t_{Fall} on P is found ($t_{Fall} \propto P^{-1.2}$), which makes the device faster at higher incident power density: this is in agreement with a traps dominated scenario where capture and emission processes from trapping states are influencing photocurrent transients.[98,99] In fact, because of the interplay between relatively fast volume traps and relatively slow interface traps (located at the interface between PEDOT:PSS and P3HT:$PC_{61}BM$), at high P interface traps are completely filled and fast volume traps are dominating, while at low P slow interface traps are partially filled and come into play as well.

2.3.2 Sintering parameters, CCI-300 and PFN to reduce dark current

Thanks to a careful optimization of printing steps and active material ink formulation, we have been able to obtain good yield and reproducibility of devices fabrication, with EQE in excess of 80% at the peak of active material absorption. However, dark current density is still too high to fit into the requirement for an imager (sec. 3.2.4). Both reducing the roughness and increase the energetic barrier for the hole injection, i.e. further reducing the Ag workfunction, could positively affect the dark current density.[100] Because printed silver profile is strictly dependent on ambient conditions,[101] a change in sintering parameters was explored in order to smooth the bottom electrode. AFM images of printed Ag stripes reveal that increasing the sintering times above $10min$ results in negligible effect, while temperature affects the cluster size formed after the sintering step, but roughness is not significantly lowered.

On the other hand photodetectors were fabricated replacing TEC-IJ-010 with CCI-300 ink to investigate if the different formulation, based on dispersion of nanoparticles instead of clusters, allows to print smoother films with W_f closer to the one of bulk silver. The optimization of deposition parameters for CCI-300 ink allowed to print $\sim 150\mu m$ large and $200nm$ thick stripes, without scalloping. By diluting the formulation of the ink printed stripes thickness is almost halved. AFM topography on CCI-300 stripes do not show relevant differences with respect to TEC-IJ-010 both for the as-received ink and the diluted one. I-V measurements show a small reduction in dark current density for $1V$ reverse biased device that is not enough to satisfy the requirements (tab. 2.1).

In addition to the work done on the bottom electrode we focused on its functionalizer. As reported in the literature also for other polyelectrolytes,[102] PFN plays a significant role in charge injection and extraction at the interface between electrodes and organic semiconductors.[103] Spincoated PFN, with the recipe previously stated, results in a layer of $5-10nm$ thickness with the topography reported in fig. 2.9a. In spite of being a thin layer, we stress the fact that it is very different from the one formed by PEIE which is only physisorbed on the underlying surface.[78] Fig. 2.6b shows PFN absorption spectrum peaked around $390nm$. Its effectiveness in W_f reduction was investigated by kelvin probe measurements and was reported at sec. 5.3.1. The introduction of PFN in our devices led to a reduction in reverse dark current density which is kept below $100nA \cdot cm^{-2}$ (fig. 2.7a). Another premium feature of PFN functionalization is that reverse bias can be applied up to $9V$ without their breakdown and irreversible damage, while for PEIE-based it occurs even below $1.5V$. Despite the positive effect on dark current, being PFN a bad conductor,[104,105] holes have to cross an additional insulating layer to be extracted and reach the bottom electrode. Consequently photocurrent and direct current are lower than the one for PEIE-photodetectors. The effect is seen also on EQE spectrum which is lower than the one of PEIE-devices (fig. 2.7b). Devices EQE slightly depends on optical power ($\propto P^{-0.09}$), while

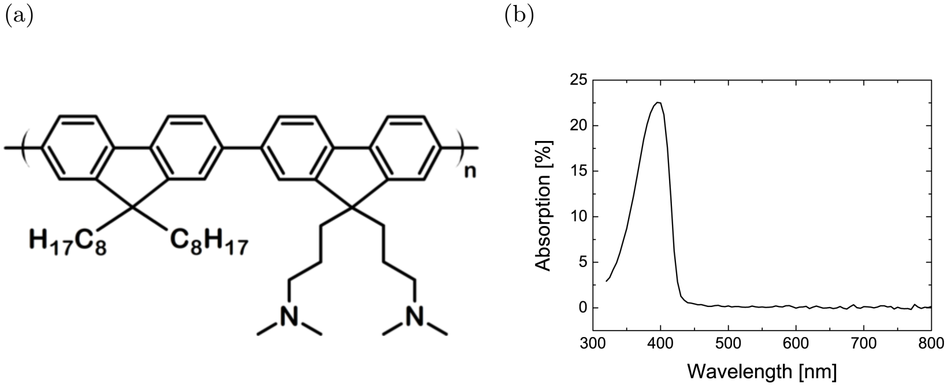

Figure 2.6: Chemical structure of PFN (a) and its absorption spectrum of PFN (b).

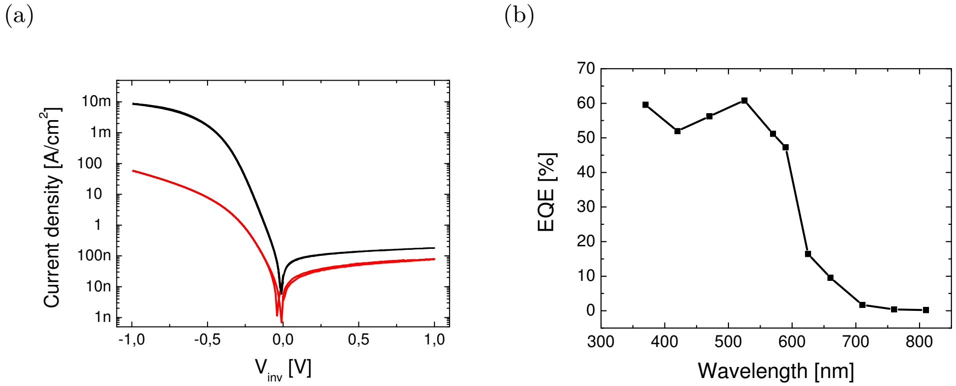

Figure 2.7: (a) Comparison between dark current I-V measurement of PEIE-functionalized (black) and PFN-fuctionalized (red) photodetectors with TEC-IJ-010 as bottom contact. (b) EQE spectrum of CCI-300/PFN/P3HT:PCBM/P JET 700 N+Zonyl acquired at $1mW \cdot cm^{-2}$, $1V$ bias.

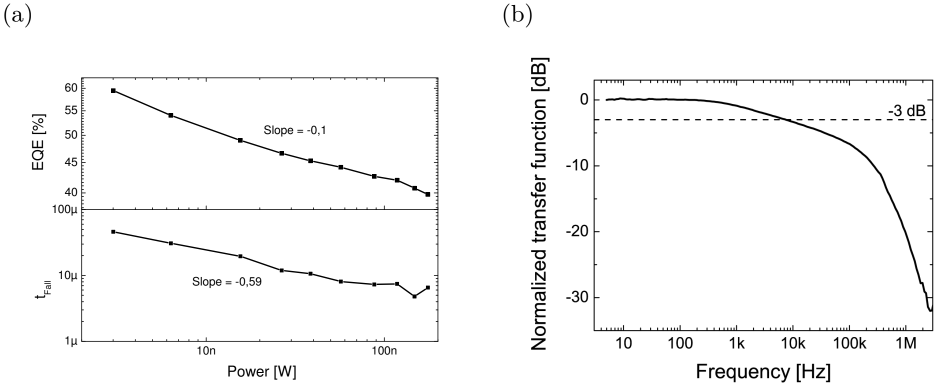

Figure 2.8: (a) PFN-based detector EQE and response time vs. impinging power meaured at $570nm$, $1V$ bias. Device bandwidth measured at $570nm$ at an incident power density of $0.1mW \cdot cm^{-2}$ ($1V$ applied bias).

response time dependence is mild and goes as $P^{-0.57}$ and lower than $10\mu s$ for high light levels. Frequency measurement exhibits $6.5kHz$ bandwidth (fig. 2.8).

2.3.3 Semi-transparent devices

So far we have demonstrated that it is possible to obtain highly efficient printed photodetectors with low dark current density suitable for X-ray detection through the engineerization of the device. To fully exploit the potential of organic printing technology, all-carbon based photodetectors with semi-transparent electrodes were printed on a flexible substrate.[106] To reach this goal the silver bottom contact was replaced with a PEDOT:PSS electrode, so that the only non transparent material would be the active blend for which the transparency could be modulated by varying the thickness. Not only this electrode allows for the semi-transparency of the device, but it also provides a very smooth interface with the organic semiconductor compared to the one of silver contacts (fig. 2.9b-c). Both PEIE and PFN were tried as interlayer. In fig. 2.10a it is shown that dark current density at $1V$ of reverse polarization is lower than the one exhibited by Ag-based devices suggesting that the smoother bottom electrode surface reduces instabilities due to the formation of leakage paths often observed with the rougher silver printed electrode. Kelvin probe measurements prove that the PEIE and PFN are effective in inducing asymmetry of W_f between top and bottom electrodes also for PEDOT:PSS contacts (sec. 5.3.1). Fig. 2.10b shows the EQE recorded illuminating the devices from top and from substrate side. For both the efficiency is above 40%

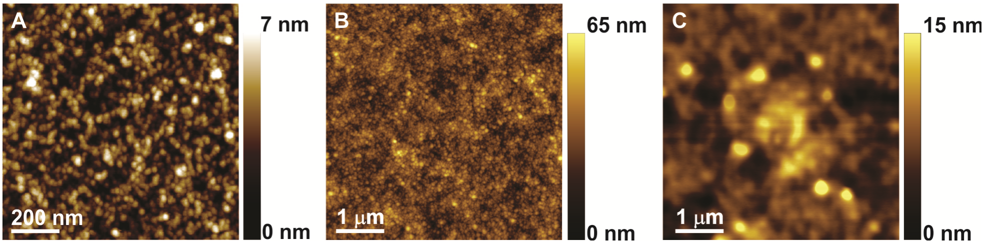

Figure 2.9: AFM images (a) PFN spin coated on glass, (b) CCI-300 bottom contact; (c) PEDOT:PSS bottom contact. Different sintering steps were tried for the silver ink obtaining comparable surface morphology features and roughness ($20 - 30nm$).

in the region of absorption of the active material. Substrate light absorption can be accounted for the difference between the two spectra.

2.3.4 Increasing photoactive area

In addition to dark current and EQE also photodetector capacitance is an important parameter to be taken into account. It is related to the maximum amount of photogenerated charge that can be detected by the pixel, to capacitive coupling when the switch is commuted and to noise considerations.[79]

Considering the architecture of an imager (sec. 3.2) the row-addressing signal couples through parasitic switch capacitances changing the voltage across the photodetector of:

$$\Delta V_{PD} = \Delta V_{Row} \frac{C_P}{C_P + C_{PD}} \tag{2.1}$$

where ΔV_{Row} is the maximum voltage swing of the row, C_P the parasitic capacitance between row line and photodetector, C_{PD} the photodetector capacitance. This effect could be detrimental for the readout process and should be minimized by increasing C_{PD}/C_P ratio. Regarding the parasitic capacitances of the addressing transistor they are around $0.5 - 1pF$ (sec. 3.3.1), while for the switching diode $\sim 1pF$. Kept constant the thickness of the layers that give good static performance, the values of the parasitic capacitances are strictly related to the limit in resolution capability of inkjet printing and they are difficult to be lowered without changing processing techniques. Consequently, the easiest approach to reach the goal is to increase the photodetector capacitance. This can be done by enlarging the photoactive area (eq. 3.1), turning down the achievable resolution. Due to subtle relation between drying dynamics and layer morphology this step is far from being trivial, e.g. the fabrication of larger silver bottom contacts results in thicker

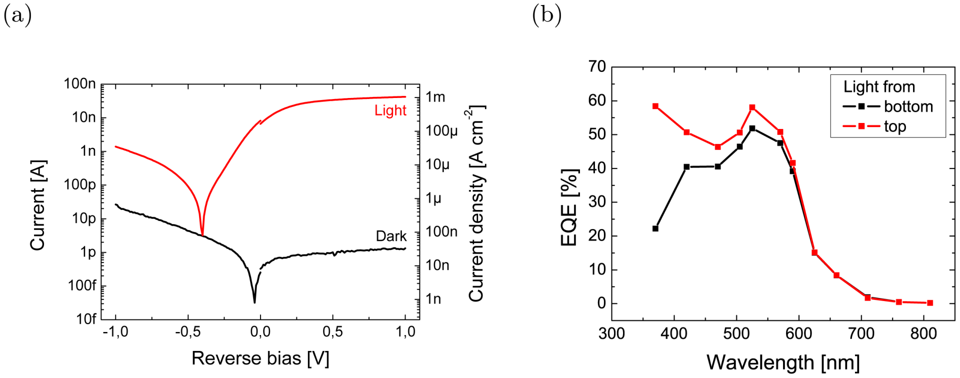

Figure 2.10: (a) I-V measurements in dark (black) and under white light (red) of a semitransparent PFN-based photodetector. (b) EQE spectra acquired shining from top (black) and from substrate side (red) light at $\sim 1mW \cdot cm^{-2}$, $1V$ bias.

and prone to cracking electrodes. Because of the cracks of silver bottom electrode we selected PEDOT:PSS bottom contacts for the following developments. We started realizing larger photodetectors simply extending patterns used for $100 \cdot 100\mu m^2$ devices to obtain $(200\mu m)^2$ and $(300\mu m)^2$ nominal areas. Despite the good coverage of the electrode pad by P3HT:PCBM blend dark currents are orders of magnitude higher.

The same worsening can be seen even for small devices where the PEDOT:PSS electrode was deposited using droplet of larger volume ($\sim 200pL$) that we realized. Even if the macroscopic properties of the top electrode are not sensitive to the variation of this parameter, on the contrary, post-processability and optoelectronic behaviour of devices do show a dependence on the PEDOT:PSS printing recipe. Most strikingly, large PEDOT:PSS droplets result in devices that are unable to withstand post-deposition thermal treatments: as-printed devices have a proper electric behaviour, but become short circuits after annealing at temperature as low as $90°C$. For this devices the EQE is larger than 40% over a broad wavelength range up to $\sim 600nm$. The specific detectivity is $2 \cdot 10^{11} Jones$ (evaluated at $570nm$, $1V$ applied bias): if compared to the literature on P3HT:PC$_{61}$BM photodetectors,[92–96] this is a relatively low value, as a result of relatively high dark current density (few $\mu A \cdot cm^{-2}$). These results suggest that the deposition of PEDOT:PSS on top of the blend layer is a delicate process step that can significantly change the performances.

Seen these results we fabricate photodetectors where top electrode is finger-like with stripes as narrow as the one used for $(100\mu m)^2$ detectors. The photosensitive area is given by the intersection of top fingers and bottom pad

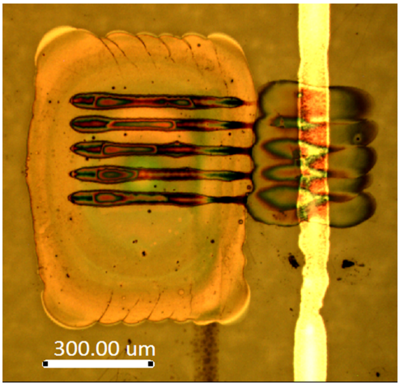

Figure 2.11: Optical micrograph of a large-area, semitransparent photodetector. Scale bar = $100\mu m$.

(fig. 2.11), and are around $180 \cdot 300 cm^{-2}$. Characterization done on large area devices realized in this way show negligible variations with respect to smaller one apart from the device capacitance which is increased up to $\sim 8pF$ almost direct proportionally to the area (tab. 2.1).

2.3.5 Fully-printed photodetectors

Having available an all-patterned device it would be a great advantage for its integration with different electronic components because it does not require deposition steps affecting the whole substrate. In previously presented devices bottom contact functionalization was still done by mean of spincoating. To address this point we formulated a printable PFN-based ink and printed it only on the bottom electrode.

In figure 2.12a are reported I-V plots measured on the best device with PFN printed on PEDOT:PSS bottom electrode. Reverse dark current density is the lowest of the fabricated devices and reaches $3nA \cdot cm^{-2}$ at $1V$ giving a light/dark ratio of $2.5 \cdot 10^5$. EQE exceeds 40% over a $200nm$ band of wavelength with a peak of 42% at $525nm$ (fig. 2.12b). The best value for calculated D^* is of $6.2 \cdot 10^{12}$Jones: the record among the ones we obtained. EQE is weakly dependent on P (EQE $\propto P^{-0.06}$) while the response time follows a power law on P with -0.91 as exponent (fig. 2.12c). The $90\% - 10\%$ photocurrent fall time is of about $100\mu s$ at $1\mu W$ of impinging power (fig. 2.12d).

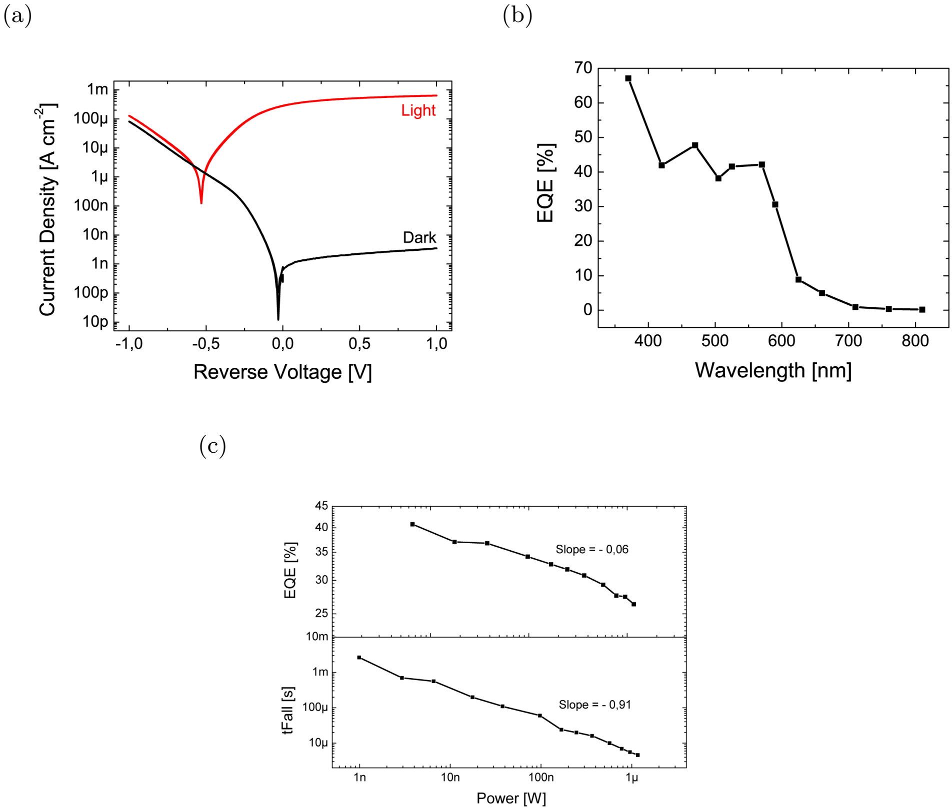

Figure 2.12: (a) I-V measurements in dark (black) and under white light (grey) of a fully-printed photodetector. (b) EQE spectrum acquired at $\sim 1mW \cdot cm^{-2}$, $1V$ bias. EQE (c) and t_Fall (d) as function of the incident power density (measured at $570nm$, at $1V$ applied bias).

2.3.6 Direct current increase

Work was done to increase direct current density motivated by the fact that a possible pixel architecture makes use of a diode as addressing element (a detailed discussion about pixel structure and its readout will be carried out later at sec. 3.3).

Aiming to a photodetector with a high rectification ratio, we tried to keep reverse current density as low as possible and to rise the direct current at the same time. We set aside PFN as interlayer because it introduces a high series resistance strongly affecting the direct current. Instead PEI was used to tailor bottom electrode W_f. We fabricated devices both with small ($50 \cdot 80 \mu m^2$) and large area ($250 \cdot 300 \mu m^2$).

I-V curves exhibit reverse dark current density mean value of $200 nA \cdot cm^{-2}$ (best device: $130 nA \cdot cm^{-2}$) (fig. 2.13a) and mean direct dark current density of $34 mA \cdot cm^{-2}$ (best $90 mA \cdot cm^{-2}$) ($-1V$ bias) which is among the best results obtained for P3HT:PCBM detectors.[89,107]

A EQE peak of 73% at $470 - 505 nm$ was recorded (fig. 2.13b). Calculated peak D^* results in $4.52 \cdot 10^{12}$Jones at $525 nm$ for the best device. Dark current density is aligned with PFN-based detectors while the EQE is slightly better (tab. 2.1).

Measuring photoresponse in fuction of impinging light power PEI-functionalized devices reveal a photoconductive behaviour with EQE > 1 for low light intensities (fig. 2.14a). Time response is power dependent: the $90\% - 10\%$ response time goes from its lowest value at the higher illumination ($426 \mu s$ at $130 nW$) to higher ones, reaching the value of $8.5 ms$ at $745 pW$ (fig. 2.14b). We stress the fact that in the presented way it is possible to realize the two different components of the diode-addressed passive pixel at the same time, without addition of process steps.

2.3.7 Other photodetector structures

We printed P3HT on top of the blend in a PEI-based device because it might help to reduce dark current and to tailor the interface with the top contact.[98,99] Dark current density and direct current density are lower than for reference one, i.e. without the P3HT interlayer; EQE is comparable. A preliminary characterization was done changing the light intensity. Both behaves as photoconductor in the region of high impinging light intensities, but they differ going towards low light regimes. Decreasing impinging optical power the detector with P3HT interlayer turns out to be slower than the reference. Further investigation should be done to in depth understand the modification of the interface and consequent effects on devices performances.

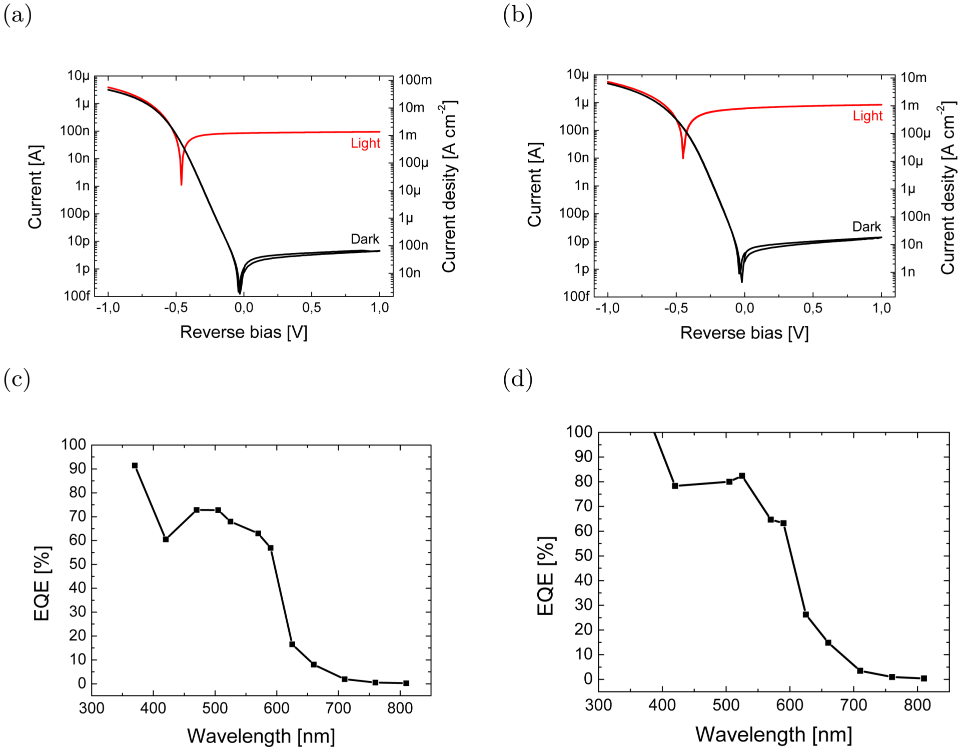

Figure 2.13: I-V curves of a small photodiode in dark (black) and under white light (red) (a) and of a large photodector realized with the same process (b). EQE spectra measured at $1V$ reverse bias under $\sim 1mW \cdot cm^{-2}$ light for swD (c) and PD (d).

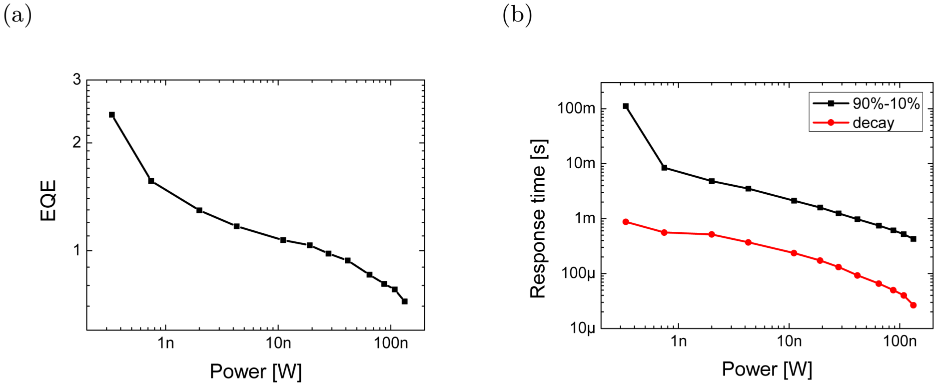

Figure 2.14: EQE (a) and response time (b) as function of the incident power density (measured at $570nm$, at $1V$ applied bias).

Also other photodetectors structures were fabricated and tested, e.g. devices with interlayer deposited on top of P3HT:PCBM or other injection blocking materials (vanadium oxide and zinc oxide), but not fully characterized because preliminary results obtained on I-V measurements do not show better performances compared to the ones already obtained. Gathered data are reported in table 2.1.

2.3.8 Air exposure and shelf life measurements

After being annealed and tested the first time some of the P JET 700 N / PEIE-based devices were exposed to air for 1 hour, then moved again inside a glovebox and measured. No significant change in current densities was seen.

Shelf-life measurements were performed. Some CCI-300 / PFN- and P JET 700 N / PEIE-based devices were kept inside a glovebox for 9 and 10 month respectively. I-V curves acquired show no variation compared to the first measurement pointing out that the photodetectors are pretty stable in controlled environment.

2.3.9 Encapsulated photodetector and noise measurement

We also measured photodetector noise in order to estimate the minimum detectable signal. For this purpose semi-transparent, large area, PEI-funtionalized photodetectors were encapsulated by spincoating PMMA in acetonitrile and IPA (sec. 3.3.1 for details on PMMA formulation) on top of the devices and glueing the whole substrate between two glass slides by means of epoxy resin. We recorded I-V curves of the encapsulated photodetectors finding only little difference with the non-encapsulated ones (fig. 2.15a). Leaving them in air for 20 days dark current characteristics remained unchanged demonstrating the encapsulation effectiveness. The device impedance was acquired with an LCR meter and results in a capacitive component of $15pF$ with series resistance of $40k\Omega$ due to PEDOT:PSS access lines (fig. 2.15b).

Noise power spectra were measured with a cross-correlation spectrum analyser[108] keeping the device in dark and polarizing it at different reverse bias voltages. The instrument returns the parallel noise spectral density in a band from $0.1Hz$ to $10kHz$ (fig. 2.16a). At higher frequencies amplifiers series noise is coupled through device capacitance making it impossible to measure the photodetector noise. This effect is quantitatively in accordance with the measured impedance of the device (fig. 2.15b).

When $1V$ is applied to the photodetector a huge of $1/f$ noise dominates over the white dark current shot noise ($S_{n,I_{dk}} = 2qI_{dk} \sim 8.25 \cdot 10^{-29} A^2/Hz$). Noise corner frequency is around $10kHz$ with $1V$ bias. Decreasing the re-

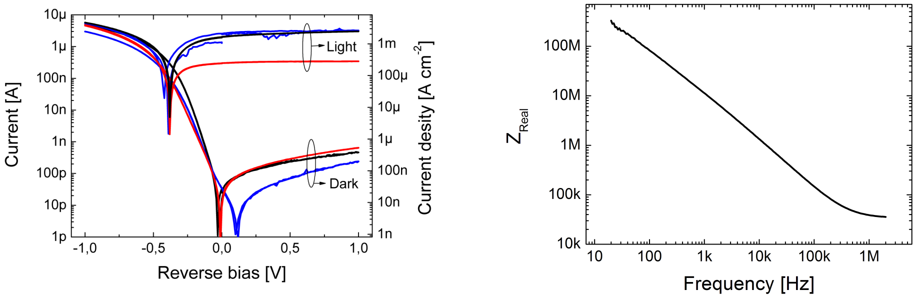
(a)

(b)

Figure 2.15: (a) I-V curves for photodetector in dark and under light ($6400K$, $\sim 1mW \cdot cm^{-2}$) before (black) and after encapsulation (blue). After 20 days of permanence in air I-V curves were measured again (red) (non calibrated light). (b) Real part impedance of the encapsulated device vs. frequency. At low frequency capacitive part is dominating while at high frequency the device impedance is clamped to electrode resistance.

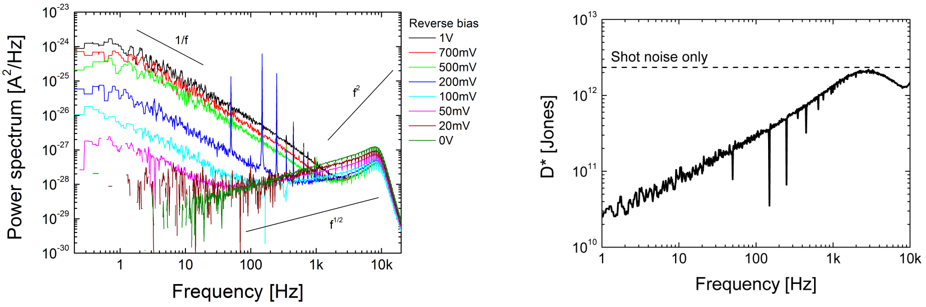
(a)

(b)

Figure 2.16: (a) Noise spectral density of an encapsulated photodetector recorded in dark conditions. The reverse bias was varied from 0 to $1V$. D^* vs. frequency evaluated on the basis of the noise measured on the device biased at 1V.

verse polarization $1/f$ noise diminishes completely vanishing when zero bias is applied, as expected for thermodynamical reasons. At the same time a component proportional to $f^{0.5}$ rises. Further investigation and device modelling must be done to give a physical meaning to this contribution.

In presence of Flicker noise the expression for D^* given in sec. 1.2.2 looses its validity because the noise spectral density is no more white. D^* becomes dependent on frequency and bandwidth at which the photodetector is operated. Let's consider that photodetector signal is sharply filtered by the acquisition system between a frequency f_i and a higher one f_f. The minimum detectable signal (at SNR= 1) is given by the square root of the noise power:

$$S_{min} = \sqrt{\int_{f_i}^{f_f} S_n df} \tag{2.2}$$

where S_n is the noise power spectral density and f the frequency.

In our case, being the photodetector cut-off frequency of about $5.5kHz$ there is no reason to operating the device above this frequency. A bandwidth between 1 and $5.5kHz$ is a reasonable choice. In this situation we can compare S_{min} obtained considering the measured noise spectral density and the one calculated taking into account only the shot noise. In the first case $S_{min} = 2.9pA$ while for the latter $S_{min} = 0.67pA$. The dominant Flicker noise exhibited by the photodetector under test worsens the SNR performance as expected.

D^* in presence of non-white noise can be rewritten as follows:

$$D^*(f) = \frac{\lambda q}{hc} \frac{\text{EQE}\sqrt{A}}{\sqrt{\frac{1}{1Hz} \int_{f}^{f+1Hz} S_n(\bar{f}) d\bar{f}}} \tag{2.3}$$

where λ is the wavelength of impinging light, q the elementary charge, A the area of the photodetector, h the Planck constant, c the speed of light. In fig. 2.16b the D^* vs. f for the measured device is reported and compared with specific detectivity for shot noise only.

In most of the works presented on organic photodetectors, D^* was extrapolated without measuring noise power density (sec. 1.3.4). Therefore, to compare our results with the works reported literature we keep on using D^* calculated on the base of shot contribution only.

2.4 Conclusive remarks

Table 2.1 summarizes the results obtained and presented in this chapter. Overall, we have demonstrated the possibility to fabricate photodetectors with good optoelectronic performances via cost-effective and additive inkjet printing technique. Silver based photodetectors show worse performances with respect to PEDOT:PSS ones or because dark current density is higher or because of poor EQE. Additional key features as semi-transparency and fully-patternability of the realized PEDOT:PSS-based devices offer advantages for their integration in complex electronic systems. With a calculated specific detectivity that reaches $6.2 \cdot 10^{12}$Jones in the best case, the inkjet printed photodetectors realized in this work are not only among the best of printed photodiodes reported in literature so far but compete also with their inorganic counterpart (sec. 1.3).

A careful optimization led to achieve photodetector and switching diode with parameters values that fulfil the requirements for the fabrication of a photosensitive pixel based on these kind of detectors (sec. 3.2.4).

Future developments should investigate deeply the temporal dynamics and find ways to improve the inkjet printed photodetector speed. Noise analysis and its reduction could be interesting topics too.

Device structure	**Dark current density** [nA cm^{-2}] At 1V bias	**Direct current density** [mA cm^{-2}] At -1V bias	**Photocurrent density** [mA cm^{-2}] At 1V bias	**Peak EQE** % (wavelength)	**D*** [Jones] (D* max)	**Number** of measured devices	**Comments**
TEC-IJ-010 / PEIE	5169 13614 56	0.65 0.36 1.08	1.32 0.32 2.00	83 (525 nm)	$2.73 \cdot 10^{11}$ $(2.62 \cdot 10^{12})$	48	Unstable for $V_{Rev} > 1.5V$
TEC-IJ-010 / PFN	171 142 56	0.03 0.02 0.07	0.67 0.44 1.26			8	Stable for $V_{Rev} < 9V$
CCI-300 / PEIE	1910 4961 19	0.19 0.28 0.81	1.22 0.15 1.47			24	Unstable for $V_{Rev} > 1.5V$
CCI-300 / PFN (after 9 month)	192 (131) 281 (73) 31 (66)	0.21 0.15 0.66	0.73 (0.74) 0.31 (0.36) 1.60 (1.40)	29 (525 nm)	$4.95 \cdot 10^{11}$ $(1.22 \cdot 10^{12})$	24	Stable for $V_{Rev} < 9V$
CCI-300 thin / PFN	1948 6310 40	0.59 0.67 2.17	0.51 0.24 0.95	62 (525 nm)	$3.32 \cdot 10^{11}$ $(2.32 \cdot 10^{12})$	19	$C_{PD} = 1.1$ pF

Table 2.1: Summary of the fabricated devices performances. For current densities mean values, standard deviation, best value are reported in this order. Where non specified photoactive (P3HT:PC$_{61}$BM) and top electrode (P JET 700 N + Zonyl) were kept constant: the device structure refers only to bottom layer and its functionalizer.

Device structure	**Dark current density** [nA cm^{-2}] At 1V bias	**Direct current density** [mA cm^{-2}] At -1V bias	**Photocurrent density** [mA cm^{-2}] At 1V bias	**Peak EQE** % (wavelength)	**D*** [Jones] (D* max)	**Number** of measured devices	**Comments**
CCI-300 thin / PFN printed	245 217 127	0.07 0.04 0.12	1.64 0.93 2.71	48 (525 nm)	$7.24 \cdot 10^{11}$ $(1.01 \cdot 10^{12})$	5	Fully-printed
P JET 700 N / PEIE (after 8 month)	86 (84) 43 (12) 24 (59)	$2.33 \cdot 10^{-3}$ $2.53 \cdot 10^{-3}$ $18.0 \cdot 10^{-3}$	0.69 (0.33) 0.56 (0.40) 2.05 (0.97)	58 top 52 bottom (525 nm)	$1.47 \cdot 10^{12}$ $(2.78 \cdot 10^{12})$	22	Unstable for $V_{Rev} > 1.5V$
P JET 700 N / PFN	120 4 117	0.04 0.01 0.04	0.39 0.07 0.44			2	
P JET 700 N / PFN Large area	27 14 16	0.02 0.02 0.06	1.25 0.38 1.63			7	$C_{PD} = 7$ pF
P JET 700 N / PFN printed Large area	191 243 3	0.04 0.08 0.32	0.60 0.70 2.38	42 (525 nm)	7 $7.18 \cdot 10^{11}$ $(6.21 \cdot 10^{12})$	19	Fully-printed

Device structure	Dark current density [nA cm^{-2}] At 1V bias	Direct current density [mA cm^{-2}] At -1V bias	Photocurrent density [mA cm^{-2}] At 1V bias	Peak EQE % (wavelength)	D* [Jones] (D* max)	Number of measured devices	Comments
P JET 700 N / PEI	202	34.42	1.83	73 (525 nm)	$1.25 \cdot 10^{12}$ ($2.45 \cdot 10^{12}$)	16	
	74	30.51	0.41				
	65	90.30	3.04				
P JET 700 N / PEI	175	6.42	1.16	82 (525 nm)	$1.46 \cdot 10^{12}$ ($4.52 \cdot 10^{12}$)	22	C_{PD} = 8 pF
Large area	277	5.95	0.50				
	18	20.33	1.83				
P JET 700 N / PFN	118	$4.95 \cdot 10^{-3}$	0.42			7	
Large area	51	$5.61 \cdot 10^{-3}$	0.12				
Printed on PMMA	42	$17.1 \cdot 10^{-3}$	0.67				
CCI-300 / Blend / PFN /	297	0.06	2.04			6	Inverted Cathode and Anode
	257	0.04	0.23				
P JET 700 N	126	0.11	2.30				
P JET 700 N / Blend / PFN /	109	1.72	2.14			6	Inverted Cathode and Anode
	16	0.60	0.48				
P JET 700 N	91	2.42	3.04				

Device structure	Dark current density [nA cm^{-2}] At 1V bias	Direct current density [mA cm^{-2}] At -1V bias	Photocurrent density [mA cm^{-2}] At 1V bias	Peak EQE % (wavelength)	D* [Jones] (D* max)	Number of measured devices	Comments
P JET 700 N / PEI / Blend / V_2O_5 / P JET 700 N	372 328 77	4.51 0.84 5.34	0.97 1.02 1.96			4	Top and bottom interlayers
P JET 700 N / PEI / Blend / P3HT / P JET 700 N	40 30 19	2.61 0.42 2.90	1.82 0.58 2.23	74 (525 nm)	$2.75 \cdot 10^{12}$ ($4.03 \cdot 10^{12}$)	2	Top and bottom interlayers
P JET 700 N / PEI spinned at 2500 rpm	37 27 17	4.60 2.75 7.53	1.17 0.14 0.91			9	
P JET 700 N / PEI spinned at 1000 rpm	96 89 33	5.97 4.28 10.05	1.17 0.25 0.65			9	Low reproducibility
Encapsulated	212 20 198	3.11 0.93 2.45				2	

Chapter 3

Direct-written passive pixel for digital imaging integrating inkjet printed organic photodetectors

Hereby it is reported on the fabrication and the characterization of passive pixels realized by inkjet printing and femtosecond laser ablation integrating an all-organic photodetector and an all-organic switch. Solutions to process integration issues are discussed. Thanks to the versatility of the fabrication approach used, three different pixel architectures were realized and here described. Their performances are presented and compared. At the end the fabrication of a matrix of pixels is reported together with its characterization.

3.1 Introduction

Many applications can take great advantages from a mechanically flexible, lightweight and non-fragile imaging device with a large pixelated photosensitive area in the fields of industrial non-destructive testing, medical imaging, homeland security, nuclear safety, solar energy harvesting and smart surfaces.[2,109,110]. Specifically, due to the lack of convenient ways for focusing X-ray radiation, digital panels are required to be as large as the objects for what they are designed to image.[111] Large area coverage can represent an issue in terms of manufacturing cost in the case of crystalline semiconductors while amorphous silicon and organic semiconductors can cope with that need.[112]

Hydrogenated amorphous silicon (a-Si:H) and standard CMOS based-backplanes were used for the addressing indirect X-ray imagers.[73,113–118] Although a-Si:H-based sensors deposited at low temperature ($150°C$) were reported,[119,120] those backplanes result brittle and limited in flexibility.[121] Different materials can be exploited to realize flexible imagers on plastic substrates at room temperature, but vacuum thermal evaporation and photolithographic steps are required.[110,122–124] The approach followed in cited examples relies in the uniform coverage of an addressing backplane with a photoactive layer. In spite of a great simplification of the process a non-pixelated photosensitive layer could be prone to optical cross-talk.[49,73] On the contrary, monolithically integrated pixels were proposed consisting in a photodetector and a transistor side by side on the same foil. The disadvantage is the reduction of geometrical fill factor, i.e. the ratio between the photoactive and the pixel areas.[125,126] Also in these examples vacuum depositions are used.

Here we report the realization of fully-direct-written, all-organic passive pixels for digital imaging applications and their organization into a matrix. Polyethylene naphthalate (PEN) was chosen as the substrate for device fabrication due its light weight and flexibility, which might be premium features in large area applications. Our approach is based on the layer-by-layer deposition of films through additive inkjet printing technique combined with femtosecond laser ablation to selectively remove materials to open sub-micrometric gaps. With respect to the presented state of the art, these techniques have a number of advantages: no need of vacuum equipment for manufacturing; films can be directly deposited on almost whatever substrates without the need of masks; they have low material consumption, produce almost no waste and can pattern large areas (sec. 1.1). Not only these techniques introduce improvements in terms of fabrication process, but also allow to realize different pixel structures and layouts.

3.2 Large area organic imager architecture

The well-known structure for an imager is a 2-D array of photosensitve pixels, organized in rows and columns, that spatially sample the impinging light signal and convert it into an electrical charge that is read through a properly designed amplifier. To reduce the cost of the system the readout circuit is shared by more than one pixel. Generally speaking, after the exposure, pixels are read line by line by means of line drivers that activate row by row an addressing element present in each pixel. The charge stored in each pixel is sent by columns to the readout amplifiers. Every pixel has three functions: conversion of light into charge, temporary storage the photogenerated charge

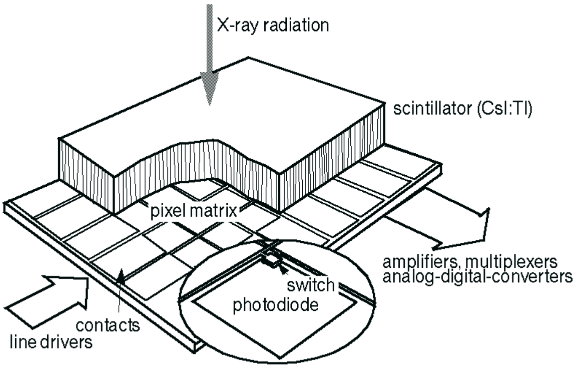

Figure 3.1: Schematic drawing of an X-ray imager.

with low losses and to transfer the charge to the readout amplifier when the pixel is addressed (fig. 3.1).

Another way to acquire a large imaging field is to scan with a 1-D image receptor the other dimension. In principle a single line detector and a very highly collimated light beam could be used for this approach. Despite the excellent rejection of scattered radiation can be achieved, this method is highly inefficient in the utilization of the output of the lamp so that much energy is wasted (in the case of X-ray imaging a full scan would result in an enormous heat led on the X-rays tube). Moreover moving parts and reconstruction algorithms must be employed.

The focus of this work will be a 2-D matrix architecture. A charge-sensitive pre-amplifier or a transimpedence amplifier (which maintain their input at virtual ground) are used as external circuitry to read flat-panel detectors.

3.2.1 Light conversion into charge

The conversion from visible photons to charge was presented in sec. 1.2. Being the X-ray imaging a feasible application the focus of this paragraph will be on the conversion mechanism related to this field. X-rays can be converted to charge either in direct or indirect way. Due to their low density and atomic weight, organic compounds are typically unsuitable for the direct collection of X-rays, whose absorption depth decreases with the atomic number Z of the material as Z^{-n}, where $n \sim 3 - 4$.[127] The direct conversion of ionizing radiation into electric charge by means of organic materials would require unrealistically high thickness of the detectors active layer. In indirect conversion high energy X-quanta are collected and converted into visible light by scintillating materials and sent to a photodiode responsive to visible radiation.

In literature there is a number of studies concerning the evaluation of scintillators parameters.[79,118,127–129] Solution processable scintillators were also proposed.[98] Common materials for scintillating screens are thallium doped cesium iodide (CsI:Tl) and Gd_2O_2S:Tb, namely GOS, both emitting in green region, at $560nm$ and $545nm$ respectively.

Regarding to this thesis work CsI:Tl was taken as reference, but the development of scintillator-pixel matrix coupling was left to further studies. For a prototype flat-panel imager with CsI:Tl as scintillator operated under mammographic conditions ($26kVp$ beam at exposure comprised between 0.5 and $19mR$) El-Mohri et al.[128] derived from simulations a X-ray fluence per unit exposure of $46520\frac{X\text{-}quanta}{mR \cdot mm^2}$ and a mean number of optical quanta emitted by the scintillator per impinging X-ray of $312\frac{photons}{X\text{-}quanta}$. These data lead to an estimation of the number of visible photons impinging on the detector operating in mammographic conditions which turns out to be in the range of $10^6 \div 10^8$ per mm^2. Similar calculation could be done for data provided by Gelink et al.[84,110] for a RQR5 radiation obtaining $\sim 10^7 \div 10^9 \frac{photons}{mm^2}$. Pixel photoresponse should cover these ranges in order to be considered for X-ray medical-imaging.

3.2.2 Charge storage

The photogenerated charge collected at PD electrodes should remain stored on the physical capacitance of the device while waiting that the other lines are read. In general, the intrinsic capacitance of the device can be described by a parallel plate capacitor model:

$$C_{PD} = \varepsilon_0 \varepsilon_r \frac{A}{d} \tag{3.1}$$

where ε_0 is the permittivity of free space ($8.85 \cdot 10^{12} F \cdot m^{-1}$), ε_r the relative dielectric constant of the intrinsic semiconductor (for organics $\sim 3 - 4$), A the geometric area, and d the thickness of the active material. During the time between the exposure and the readout dark current flows through the photodetector pushing it towards saturation. The leakage must be negligible respect to the nominal signal in order to allow dark image subtraction without reduction of the dynamic range. The noise due to dark current must be small compared to the readout noise. The maximum amount of charge that can be stored on the photodetector is its capacitance times the initially applied reverse bias voltage, typically in the order of some pC.

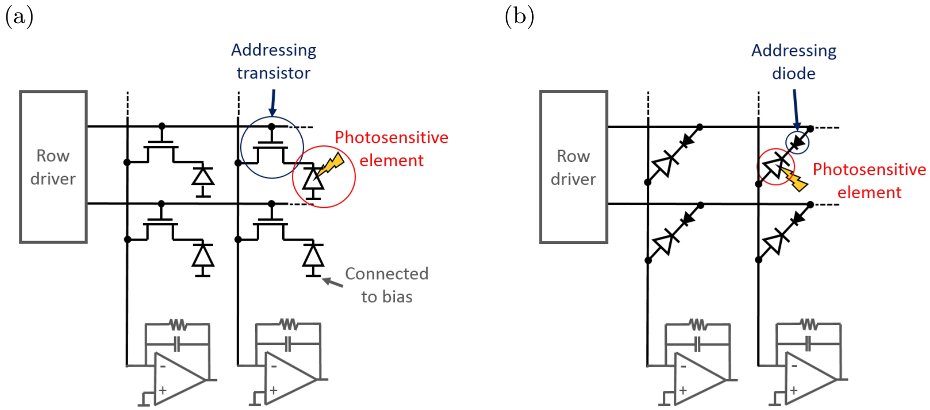

Figure 3.2: Matrix structures with TFT (a) and swD (b) as switching element.

3.2.3 Charge readout

Among CMOS pixel structures X-ray panels generally implement the passive one because it is more simple to be fabricated and maximizes the geometrical fill factor despite it is a slower, more noisy and destructive way of reading compared to active approach.[130] This is the choice also for this thesis work.

In passive pixels only two building blocks are present: a photodetector and a switch. The transfer of the photogenerated charge to the readout circuit is done thanks to the switch that can be either a thin film transistor (TFT) or a diode (swD) implementing the structures reported in fig. 3.2. In first case each pixel is a three-terminal device with the transistor gate connected to the row driver and the other two terminals connected one to the bias line and the other to the column amplifier. For what concerns the latter the two terminal pixel, comprising diodes back-to-back connected, is placed between the row driver and the readout amplifier. The fabrication of both photodetecting and addressing diodes at the same time reduces the number of process steps and therefore the complexity of the manufacturing and thus should improve the device yield.

All the switches along a row are connected together with a control line. This allows the external driver to change the state of each switching element along the row at a time. Every row requires a separate control line. The output terminals of the pixels of a column are connected to a single read out amplifier so that the matrix is read line by line.

Fig. 3.3 explains the timing of the acquisition of signal from a pixel of the imager. The matrix is initialized during a so-called reset phase in which the photodetector capacitance is pre-charged to a certain reverse bias. This is obtained keeping the switching elements in their conductive state (*on*) and

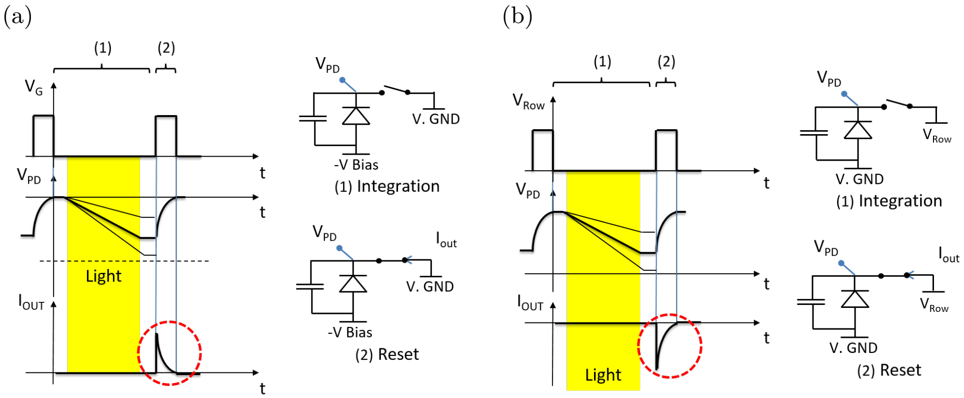

Figure 3.3: Simplified image acquisition process for TFT pixel (a) and swD pixel (b). Gate voltage/diode drive voltage, reverse bias and pixel output current are schematically depicted. The yellow region correspond to the exposure time.

then switching them back off leaving the photodetector floating. During the exposure time the photocurrent is integrated on the photodetector discharging its capacitance. When exposure is finished the subsequent reset pulse is applied a current flows through the column amplifier. Being the integral of this current proportional to the amount of charge needed to restore the reset condition it is possible to calculate the number of impinged photons. The electronics external to the matrix stores and digitizes the signal.

In absence of other spurious limitations, the time needed to transfer the charge from the pixel to the pre-amplifier is determined by the discharge rate of the photodetector capacitor through the *on*-resistor of the switch, giving a time constant of $C_{PD} \cdot R_{ON}$. While for TFT switch resistance in *on*-state remains constant with respect to source-drain voltage, with diode switches the situation is more complicated because the resistance increases (in principle exponentially) as the voltage across the diode switch reduces. This problem can be solved moving the zero signal level far from the high-resistance regime of the switching diode. To do that the row pulse for signal reading is larger than the one to reset the pixel. In this way a offset charge is read allowing to work outside the high-resistance regime of the swD. To assure that the pixel is correctly reset light must be shone between read and reset pulses, otherwise the reset one cannot properly switch on the diode. The timing diagram of the described procedure is shown in fig. 3.4.

It is worth to notice that the simple picture presented above differs from a real imaging devices because of charge-coupling transients present whenever the switching element is changed from one state to the other. The small but finite leakage current through the switch in its off-state makes the system

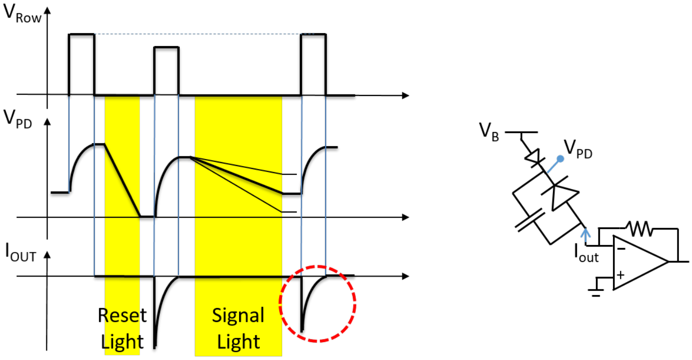

Figure 3.4: Timing scheme for switching diode pixel with optical reset. This is obtained by a succession of two row pulses per cycle with different amplitudes with an optical exposure in between.

unideal too. Both the charge injection and the leakage of the switching element during the off-state result in an offset in the read charge that must be taken into account when reconstructing the signal provided that injection does not saturate the amplifier and leakage does not delete the signal before the readout. More detailed models for pixels are reported in fig. 3.5. For a matrix where TFT is the switch charge coupling occurs through gate parasitic capacitances and off-current pushes the photodetector to reset situation. On the other hand, using a switching diode its intrinsic capacitance is the reason for charge coupling and its leakage forces the detector to saturate, acting as the photodetector dark current.

3.2.4 Passive pixel requirements

Taking into consideration a radiographic imaging system Blakesley et al.[79] have predicted that a photodiode EQE greater than 25%, dark current density around $10nA \cdot cm^{-2}$ and a TFT on/off ratio of 10^7 are required to operate a prototype imager at high exposures. For a detector operating across the radiographic exposure range, quantum efficiency above 40%, dark current density of less than $1nA \cdot cm^{-2}$ and a TFT on/off ratio in excess of 10^8 would be required. Tab. 3.1 summarizes the requested values for parameters of a good pixel. In order to neglect charge injection coupling capacitors must be at least an order of magnitude lower than photodetector one. This is achieved working on gate overlap with source and drain electrodes for TFT or keeping the switching diode area much smaller than photodetector one.[79,111] In order to be operated under X-ray exposure the photodetector has to exhibit radiation hardness.

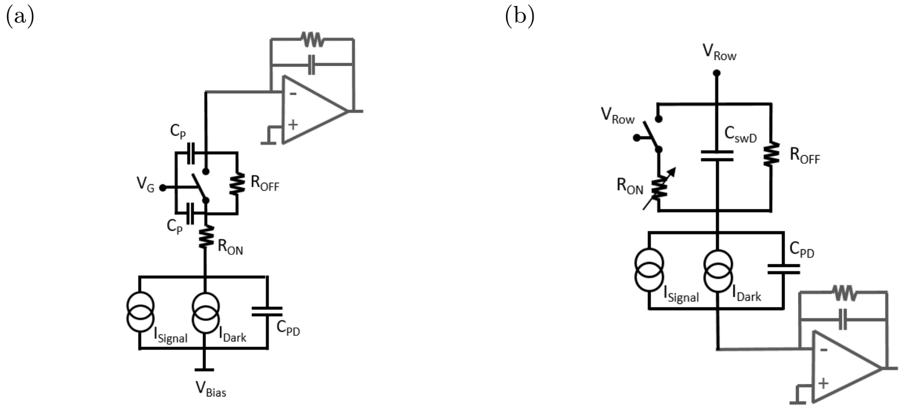

Figure 3.5: Schematic circuit diagram of a refined model for TFT-based (a) and swD-based (b) pixels. Finite R_{OFF} and R_{ON} and presence of parasitic capacitors are included.

Parameter	Value
Photodiode EQE	$> 25\%$
Photdiode dark current density	$< 100nA \cdot cm^{-2}$
Phodotiode capacitance	$\sim 2pF$
Pixel pitch	$\sim 200\mu m$
R_{ON}	$< 10^{7}\Omega$
R_{OFF}	$< 10^{14}\Omega$
Parassitic capacitance	$\ll 1pF$

Table 3.1: Parameters requirementes for a good pixel.

3.2.5 Peripheral electronics

Auxiliary circuitry is needed to operate the imager supplying the required voltages, amplifying the signals from pixels and digitising them for their elaboration and storage. The peripheral electronics also includes the logic for synchronization of driving and reading. These are parts of the system that must be carefully designed tailoring them for each particular image sensor and can have a significant effect in the imaging performances. Every peripheral component can potentially be a noise source tending to reduce the quality of the final image. The most critical one is the pre-amplifier. The standard configuration is a charge-integrating amplifier where the signal charge from the pixel is transferred to the feedback capacitor which determines the electronic gain. Usually a reset switch is used to blank out the charge on the feedback capacitors before the pixel is addressed. An other way to reset feedback capacitor is to place a resistor in parallel to it. In order to cope with charge injection through parasitic capacitors pre-amplifiers must be extremely linear and have a suitable dynamic to absorb this charge.

3.2.6 Noise components

An imager shows noise intrinsic sources that add to poissonian distribution of impinging photons and to the noise of the peripheral electronics. In the case of radiography noisy X-ray sources and fluctuation in the scintillator conversion processes must be considered too. A number of studies discuss noise sources for flat panel imagers.[131,132] In principle the approach used by Maolinbay et al.[131] can be extended to organic imagers. Therefore is possible to compute the system performances in terms of electronic noise also in this case, provided that every useful parameter is known. Here we list the main noise components related to pixel operation (fig. 3.6).

Two unavoidable noise sources are the shot and $1/f$ noises associated with the dark current of the photodetector (sec. 1.2.2) that acts both when the switch is off, integrating itself on photodetector capacitance, and when the switch is on, going directly to the pre-amplifier. This latter contribution is negligible because the time during which the photodetector is addressed is usually a small fraction of the one while the pixel is in off-state. Also the TFT channel resistance gives rise to two kind of noise: thermal and $1/f$ both in *on*- and off-state. Another source of noise is kTC noise due to the thermal noise of the *on*-resistance of the switching element. While active pixels can delete this component through double correlated sampling, in passive pixels it is unavoidable.

For what concerns the peripheral circuitry in addition to the effect of

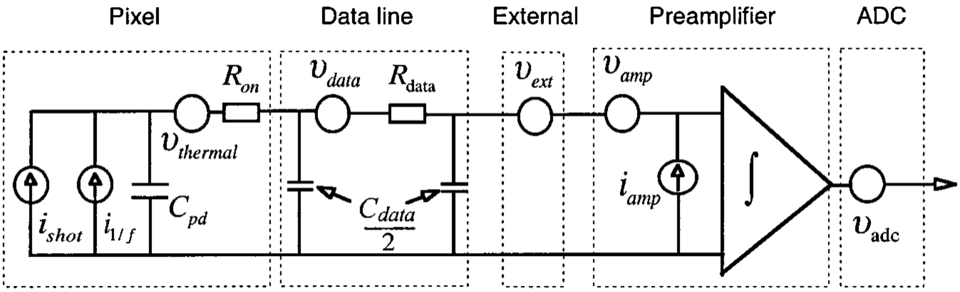

Figure 3.6: Schematic illustration of the generalized additive noise model of a flat-panel imaging system descibed in ref.[131]. The model consists of five noise components: pixel noise; data-line thermal noise; externally coupled noise; pre-amplifier noise and digitization noise of the ADC.

pre-amplifier noise, attention should put on the effect of the distributed resistance of the conductive lines on the array that acts as a source of thermally generated noise. Fluctuations of supply voltages can couple with the signal. This is manifested as line-correlated noise and can be largely lowered carefully designing the peripheral system. At last digitization noise related to the analog-to-digital converter (ADC) has to be taken into account especially for low resolution ADCs.

3.3 Direct-written organic pixel

The integration of two different devices is a non-trivial task that requires the ability to deposit materials on a defined pattern in a precise way. Moreover each deposited layer must withstand all the following process steps without a significant degradation of its properties. Consequently the two devices fabrications become interdependent, therefore particular care must be taken for actions that affect the whole substrate such as spincoating depositions and annealing steps.

Three different pixel architectures were realized taking into account results on photodetectors presented in chap. 2. Transistor development was not the purpose of this work.[1]

---

[1] Sadir G. Bucella and Mario Caironi are acknowledge for providing direct-written TFTs and for the work done to tailor their characteristics for specific needs of this work.

3.3.1 Pixel structures and realization

Within the realized pixel structures two make use of a TFT as addressing element, the other one is a double diode pixel. One of the TFT+PD and the swD+PD have coplanar photosensor and switch, viz. fabricated on the substrate, while for the third the photodetector is printed on top of the gate dielectric and connected by a vias to the transistor (fig. 3.7 and 3.8). In the following we will refer to the pixel as 'coplanar', 'double diode' and 'stacked' respectively.

3.3.1.1 Coplanar pixel

For the coplanar structure at first silver reference marks were printed and sintered. Then a first part of TFT fabrication was done: P JET 700 was printed, covered by spincoated PEI and ablated transversally to obtain source and drain contacts; P(NDI2OD-T2) N2200 (from Polyera) was printed over the channel and annealed at $120°C$ overnight. This choice was taken because the overnight annealing results in lowering detector performances due to increased dark current or shortcircuiting their electrodes (sec. 2.3.1). Subsequently a large-area, semitransparent photodetector with printed PFN as interlayer was realized as reported (sec. 2.2 and 2.3.5). After that the TFT dielectric is realized by spinning PMMA dissolved in acetonitrile (AcN)-isolpropyl alcohol (IPA) $(7:3)$ at $65 mg \cdot mL^{-1}$. PMMA solution was carefully selected to preserve photodetector performances. Standard solvents used for PMMA, i.e. n-butil acetate and methyl ethyl ketone, damage the photodetectors shortcircuiting top and bottom electrodes as can be clearly seen from I-V of photodetectors on top of which solvents under investigation were spincoated (not shown). As reported in literature they are good solvents for PCBM.[133] This evidence suggests that PCBM is ridissolved leaving a photoactive layer full of pinholes that fosters the collapse of the top electrode on the bottom one. From optical micrograph damaged spots due to solvent spinning can be seen in fig. 3.9a. Cytop dielectric (from Bellex) resulted in PD damage too. A single PMMA solvent that is orthogonal to P3HT and PCBM is hard to be found. PMMA co-solvents were considered and according to Hansel's parameters we selected AcN and IPA solution to be orthogonal for the blend and verified this hypothesis by spinning it on top of a photodetector.[134] We optimized AcN:IPA ratio and the spinning parameters to obtain a $350 - 450nm$ thick film as flat as possible. To fabricate transistor PMMA was spinned at $6000rpm$ for $1min$, obtaining a layer of $425nm$ with a waviness of $\pm 25nm$ (fig. 3.9b). To close the TFT gate electrode was printed with P JET 700. At the end the pixel was moved inside a glovebox and annealed at $100°C$ for $1h$.

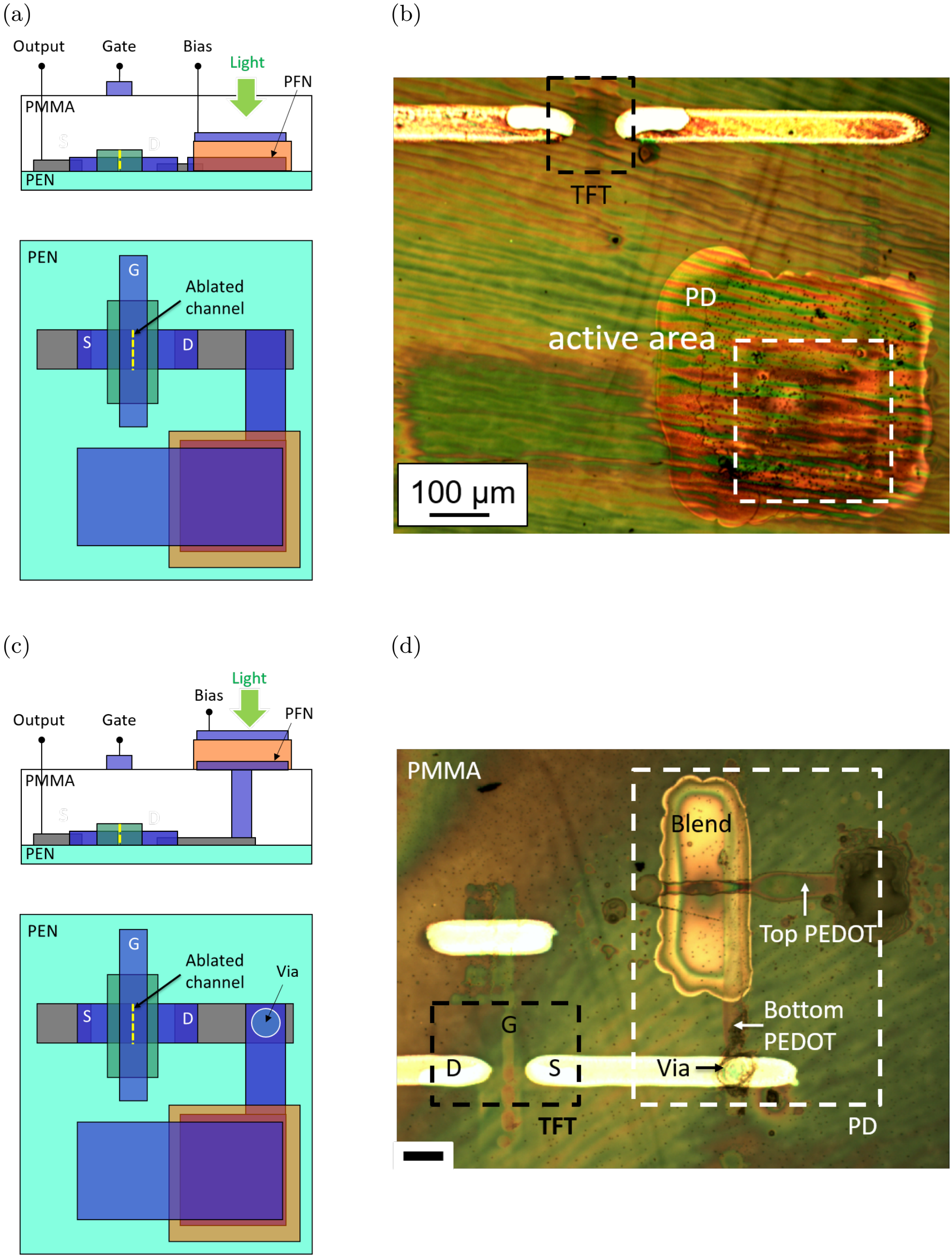

Figure 3.7: Side view (top) and top view (bottom) of the layouts for pixels realized with TFT as switch: coplanar (a) and stacked (c). In blue is depicted PEDOT:PSS, in grey silver, in orange P3HT:PCBM blend, in green N2200. Optical micrograph micrograph for coplanar (b) and staked pixels (d). Locations of pixel components is highlithed with dashed rectangles. Scale bar = 100μm.

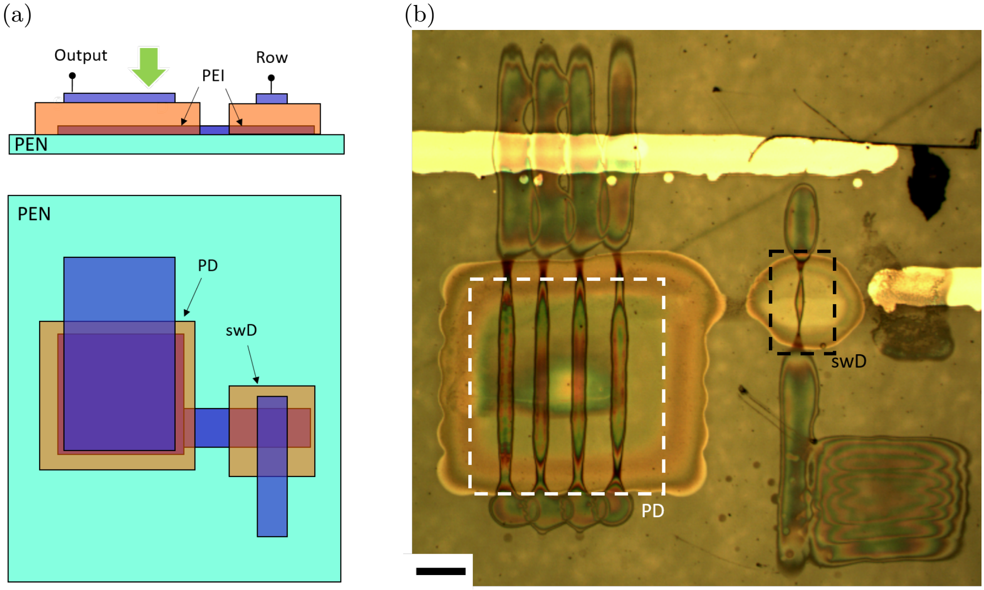

Figure 3.8: (a) Side view (top) and top view (bottom) of the layouts for the double pixel realized. In blue is depicted PEDOT:PSS, in grey silver, in orange P3HT:PCBM blend, in green N2200. (b) Optical micrograph micrograph of the pixel with locations of pixel components highlithed with dashed rectagles. Scale bar = $100\mu m$.

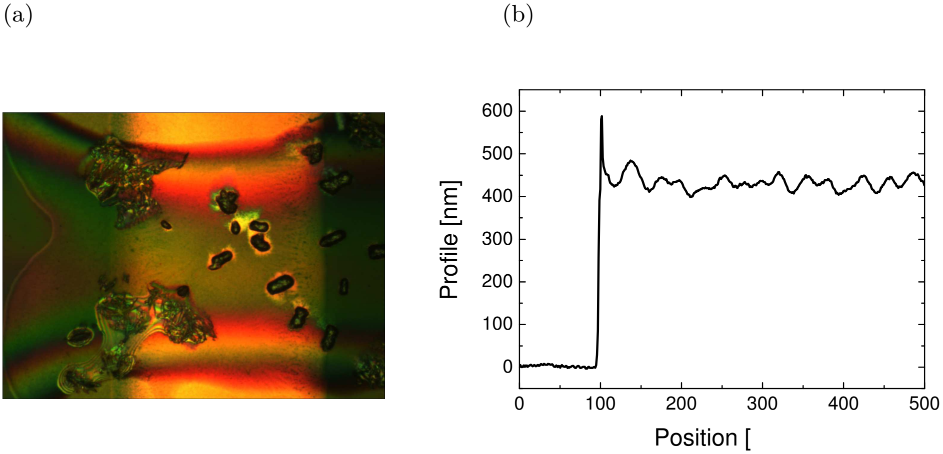

Figure 3.9: (a) Optical micrograph of a printed photodetector on which n-butil acetate was spincoated. Damaged spots can be clearly seen. (b) Profile of PMMA film spincoated on PEN following the recipe described in the text.

3.3.1.2 Stacked pixel

To obtain a direct-written TFT with the good performances n-butil acetate should be used as PMMA solvent and an overnight annealing at $120°C$ performed after the dielectric deposition.[67] Both are steps that lower or even permanently damage performances of the printed PD. A way to solve this integration issue is to fabricate the photodetector when the TFT is finished and annealed, on top of PMMA dielectric. Exploiting a bottom contact transistor, TFT electrodes and PD ones lie on different planes separated by an insulating layer. The electrical connection between TFT and PD is done by opening a via hole in the PMMA layer printing a number of chlorobenze droplets on the same position. To realize the stacked pixel a TFT was fabricated as described in the following. At first silver reference marks were printed and sintered. Then P JET 700 was printed, covered by spincoated PEI and ablated transversally to obtain source and drain contacts; N2200 was printed over the channel and annealed at $120°C$ overnight. After that PMMA at $65mg \cdot mL^{-1}$ in n-butil acetate was spincoated as TFT dielectric. To close the TFT gate electrode was printed with P JET 700 over the channel region. Thereafter a vias was opened on a silver pad that was connected with a PEDOT:PSS electrode of the transistor and filled with P JET 700 N. Then a semitransparent photodetector with printed PFN as interlayer was realized as reported (sec. 2.2 and 2.3.3). The area of the PD is of $2500\mu m^2$. At the end an annealing at $100°C$ for $30min$ and then $120°C$ for $1h$ was done in glovebox.

3.3.1.3 Double diode pixel

Double diode is the simplest structure for the pixel. It was realized by printing two semi-transparent, PEI-functionalized photodetectors, one with large area ($250 \cdot 300\mu m^2$) and the other one small ($50 \cdot 80\mu m^2$), connected by the bottom electrode (sec. 2.3.6). In this way there were fabricated two photodetectors connected back-to-back by the cathode electrode.

The fact that switching diode is sensitive to light too does not introduces issues on the working mechanism of the pixel: dark current and photocurrent of the switch act in parallel to the ones of the photodetector. Keeping their areas unbalanced by a factor 10 or more the main dark and light contributions come from the photodetector.

3.3.2 Results and discussion

Single devices, isolated from each other, but subject to the whole pixel fabrication process were tested in order to verify the correct behaviour at the end of the realization. It is worth to be noticed that the direct-written TFTs employed in this work must be able to operate well in linear regime, i.e. at low drain-source voltages with respect to the conventional ones used to characterize organinc TFTs. This constrain is due to the ability of the realized photodetectors to withstand only a limited range of reverse biases (around $1V$, sec. 2.3). Figure 3.10 and table 3.2 report characteristics and parameters for each kind of photodetector, transistor and switching diode. From these data one can derive information about the maximum signal before pixel saturation, parasitic capacitive coupling, expected readout time and maximum delay time before signal loss due to leakage becomes too large.

The comparison with requirements (sec. 3.2.4) points out that for every structure EQE fully satisfies the specific being higher than 25% at $525nm$. One must notice that for the coplanar structure the photodetector EQE is lower with respect to the others. This can be assigned to the presence of the PMMA layer on top of the PD. The dielectric, which has a wavy profile, can scatter part of the impinging radiation. Regarding the dark current density it is lower than the required $40pA$ of the specific $(= 100nA \cdot cm^{-2} \cdot (200\mu m)^2)$. The PD capacitance is in the order of the requested one. Parasitic capacitors are esteemed taking into account the overlap between gate and source/drain contact ($\sim 50 \cdot 80\mu m^2$) for the transistor and supposing a parallel plate model with dielectric constant of 3. Their reduction costs some effort in order to stabilize printing jet and shrink as much as possible TFT electrodes width. We succeed in achieving values around $250\text{f}F$, almost negligible with respect to detector one, as requested. Resistances of the switches were roughly calculated as the ratio between the voltage across the switch and the current flowing through it. The ratio between *on*- and off-resistances of the switching element does not satisfy the specification for all the three structures. Only the double diode architecture has a R_{ON} in specific, but it is valid only at the starting point of the readout process. It is worth to notice that also for TFT the *on*-resistance decreases during the readout with the reduction of V_{DS} (fig. 3.11). Time constants related to readout and maximum delay time were calculated (tab. 3.2). Even if *on*- and off-resistances afflict predicted values for readout and maximum delay time, reasonable results are expected for a pixel. Thus we proceeded with pixel characterization.

The pixels are evaluated in terms of output current, measured photocharge vs. number of impinging photons and charge loss varying the delay between light exposure and readout. The minimum time needed to correctly read all the charge, i.e. the time for which the switch must stay in the on-state, can be derived from the output current measurement looking at the time constant of the decaying waveform. The second kind of measure points out the range of detectable signals and the IN/OUT calibration plot. Fixed an acceptable error due to charge loss mechanisms and a readout time for the pixel, the

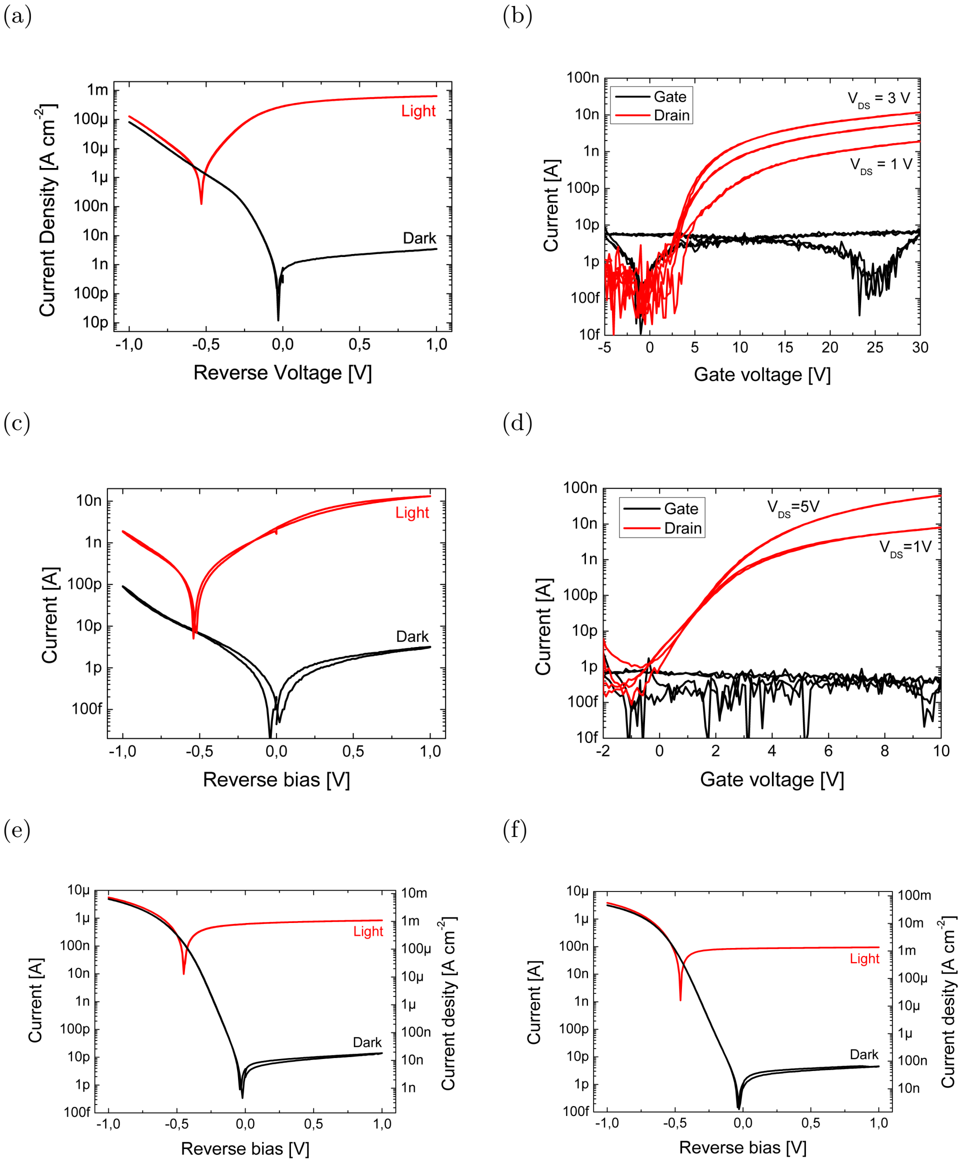

Figure 3.10: I-V characteristics in dark (black) and under white light (red) and transfer characteristics (drain current: red; gate leakage: black) of the single devices realized in parallel to pixels fabrication for coplanar (a)-(b), stacked (c)-(d) structures. I-V characteristics in dark (black) and under white light (red) of PD (e) and swD (f) for double diode structure.

Parameter	**Coplanar Pixel**	**Stacked Pixel**	**Double diode Pixel**
Dark current [pA] at 1V	10	2	20
EQE [%]	27	42	82
C_{PD} [pF]	8	0.6	8
R_{ON} [MΩ] at 1V	1000	100	0.33
I_{OFF} [pA]	0.5	1	4
Parasitic capacitance C_P [pF]	0.25	0.25	0.4
Gate voltage swing ΔV_G (min and max values) [V]	15 (-5 ; +10)	10.2 (-0.2 ; +10)	2 (0 ; +2)
Expected readout time $\tau_{read} = 5 \cdot R_{ON} \cdot C_{PD}$ [ms]	40	0.3	0.013 (*)
Expected maximum delay $\tau_{Delay} = 0.1 \cdot C_{PD} / I_{Dark}$ [ms]	80	30	70 (**)
Expected coupling $= \Delta V_G \cdot C_P / (C_P + C_{PD})$ [V]	0.454	3.1	0.09

Table 3.2: Summary of the fabricated devices performances. Expected values are calculated as indicated in the table. Specifically the maximum delay is determined by photodetector dark current being higher than TFT leakage. Photodetectors are considered biased at $1V$ in reverse condition after the reset. (*) Readout time for the double diode pixel is longer than the one reported here because of the increasing of R_{ON} approaching reset value. (**) For double diode pixel $\tau_{Delay} = 0.2 \cdot C_{PD} \cdot I_{OFF}$ because the PD is polarized around $2V$.

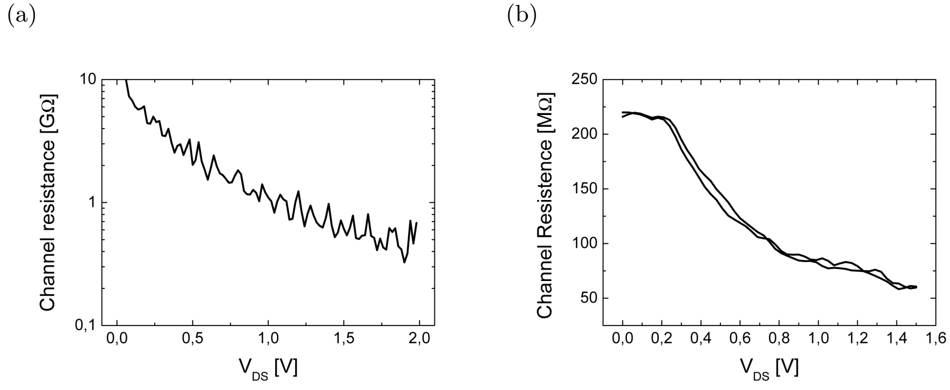

Figure 3.11: Channel resistance of TFT in coplanar (a) and stacked pixel (b) vs. drain-source voltage ($V_G = 10V$).

latter measurement gives a hint on the maximum number of rows that the sensors array can have without losing the information stored in each pixel.

In TFT-based architectures PDs have the anodes biased at $-1V$ with respect to ground. The output of the pixel was connected to the virtual ground of a DHPCA-100 transimpedance amplifier by means of a probe station. The gain of the pre-amplifier was set in order to maximize the signal without incur in saturation. The output was sent to a Tektronix MSO2014 oscilloscope. Dark reference subtraction and post processing were done by software. A LED with emission peak at $525nm$ was driven by an Agilent 81150A waveform generator and optically coupled to the pixel by means of a plastic optical fiber ($2mm$ diameter, 02-551 Edmund Optics). Impinging optical power was measured with a BPX-65 (Osram) silicon photodetector and used to compute the theoretical charge as the number of photons impinging on the sensitive are times the elementary charge.

3.3.2.1 Coplanar pixel

For a coplanar pixel the results are reported in fig. 3.12. The expected charge coupling is small, neither in measurements it turns out to be a problem. The readout time constant is around $7ms$, therefore the TFT must stay on more than $35ms$, which is in accordance with the predicted readout time. The range of detectable signal goes from $200fC$ ($1.25 \cdot 10^6$photons) to $300pC$ ($1.8 \cdot 10^9$photons). Being the active area of $7.5 \cdot 10^{-2} mm^2$, the minimum signal corresponds to $1.7 \cdot 10^7$photons $\cdot\, mm^{-2}$ which partially covers the requirement for mammography (sec. 3.2.1). The maximum measured charge is $\sim 6pC$ approaching the maximum limit imposted by the saturation ($1V \cdot 8pF = 8pC$)

If a 10% error on the measured charge could be accepted, the delay cannot be longer than $1ms$. However, the expected value was around $80ms$. After the measures we isolated single devices and tested them separately. No significant difference was found on the I-V characteristics fostering to exclude that single devices performances degraded while the pixel was measured. The low value for maximum delay is still an unclear point. It must be noticed that if more than one line has to be addressed, e.g. in a imaging matrix, the system will be subject to a trade-off between non-complete reading and the loss of charge.

3.3.2.2 Stacked pixel

Stacked pixel measurements are shown in fig. 3.14. Being the photodetector unoptimized regarding capacitance coupling, viz. its capacitance is comparable to the parasitic one, charge injection affects heavily the measurements. PSpice simulations are performed to verify the aforementioned statement. The circuital scheme reported in fig. 3.13a was implemented and the ratio between photodetector and parasitic capacitances changed. Simulated output current is reported in fig. 3.13b and clearly show that for C_{PD}/C_P ratios below 3 the readout is far from being ideal. In these cases the voltage at the node between the PD and TFT rises so high during the TFT switch on that a clipping situation is reached. From that moment on the signal is completely lost. Simulation foster to conclude that $C_{PD}/C_P \geq 10$ are desirable for the pixel correct behaviour. The stacked pixel situation is not in the latter range, thus the output current corrected by dark measurement does not have a proper shape and the readout time can not be extracted. Nevertheless, the time at which the clipping is reached depends on voltage present at the node between the PD and TFT before the switch on transition, thus related to the amount of impinged charge. Therefore it was possible to acquire the measured charge vs. the theoretical one finding that the range of detectable signal goes from $5 \cdot 10^8 \text{photons} \cdot mm^{-2}$ to $5 \cdot 10^{10} \text{photons} \cdot mm^{-2}$ (from $200fC$ to $20pC$). Mammographic range is not addressed (sec. 3.2.1), but anyhow a proof of concept for the stacked pixel realization was produced. For sure the realization of a large area PD would improve the performances and may lead to the fulfilment of the requirements.

3.3.2.3 Double diode pixel

From I-V measurements R_{ON} and R_{OFF} are respectively $\sim 500k\Omega$ and $100G\Omega$ (calculated at -1 and $1V$). Among the three structures double diode pixel exhibits the best ratio between *on* and off states ($2 \cdot 10^5$) because of relatively low R_{ON}. This result leads also to an expected fast readout compared to the

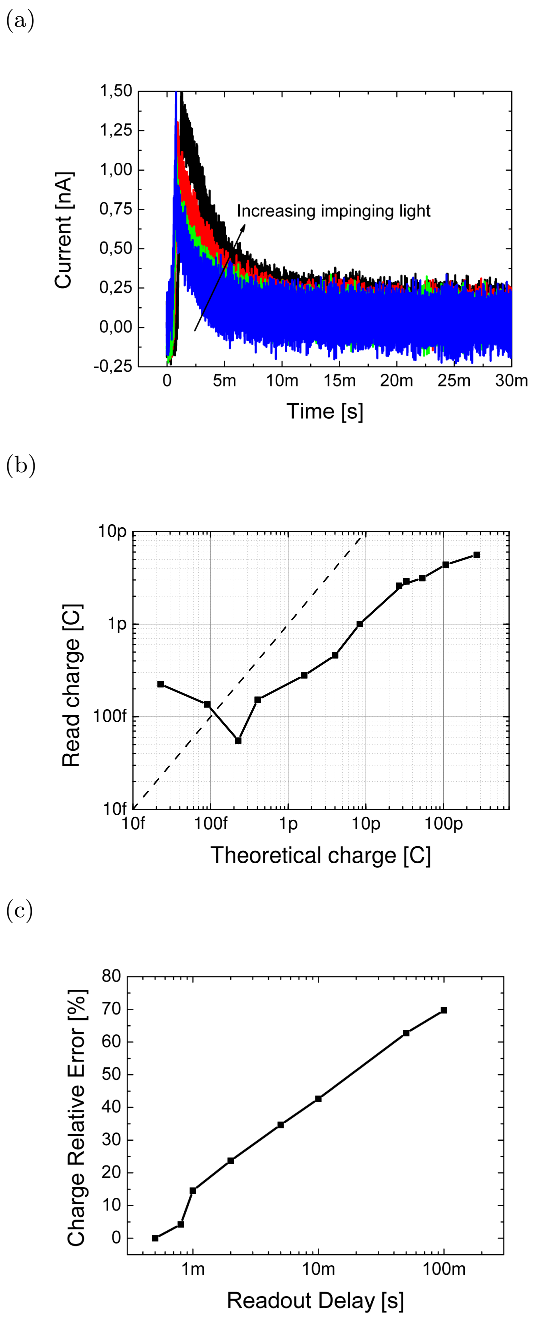

Figure 3.12: Output current at differnt light intensities (a), measured photocharge vs. theoretical (b) and charge loss varying the delay between light exposure and readout (c) for a coplanar pixel. Dashed line represents the 1:1 input/output relation.

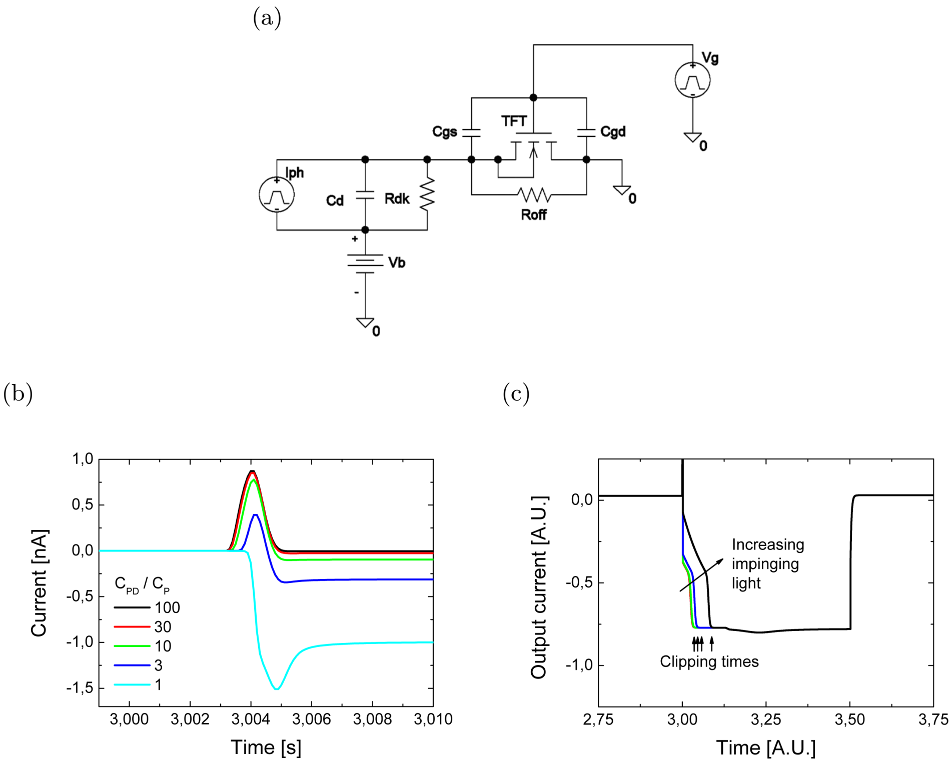

Figure 3.13: Circuital scheme used for capacitive coupling simulations. (b) Output current simulated at differen C_{PD}/C_P ratios. (c) Output current in the case of $C_{PD}/C_P = 1$ changing the amount of impinging light.

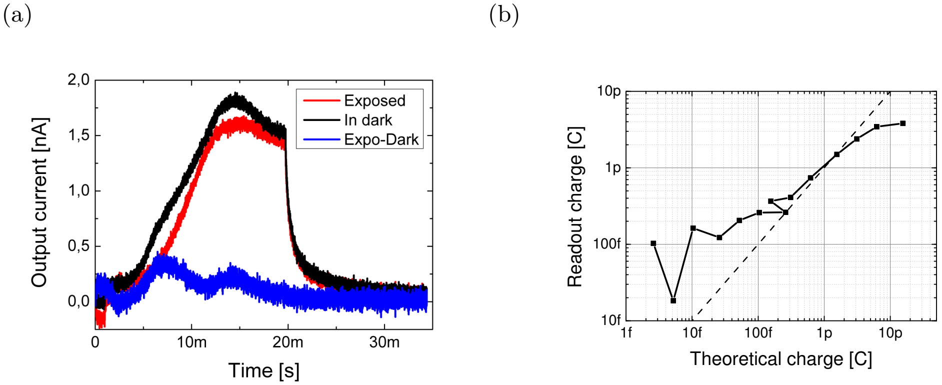

Figure 3.14: (a) Stacked pixel output current kept in dark (black) and after exposure to light (red); dark is substracted from light and the modulus of the waveform correspontng to the neat photogeneration plotted in blue. (b) Measured photocharge vs. number of impinging photons for a stacked pixel. Dashed line represents the 1:1 input/output relation.

other kind of pixels.

Double diode pixel performances are reported in fig. 3.15. The duration of the output current peak is dominated by the speed of the row pulse ramp which was kept of $100\mu s$ to control the charge coupling. The readout time constant is around $50\mu s$, consequently the addressing pulse must be longer than $250\mu s$. Expected time for readout does not consider the increasing of the *on*-resistance, thus it is reasonable that measured values are higher than what predicted. The range of detectable signal spans over almost 4 orders of magnitude and the minimum is of $1.1 \cdot 10^6$photons$\cdot mm^{-2}$. In the central range of light signals the input/output characteristic is almost linear and there is a 1:1 relation between the measured and the theoretical charge. If a 10% error on readout charge could be accepted the readout delay does not constitute a problem until $10ms$: 40 lines of double diode pixels can be read. These results perfectly fits into the requirement for mammography (sec. 3.2.1) paving the way to the realization of a fully-inkjet printed and semi-transparent organic imager.

3.3.3 Conclusions

We designed layouts of pixels selecting proper architectures that allow both to realized a direct-writing as the only approach and to explore different scenarios. Thanks to a careful control of the deposition steps, we succeeded in the realization of photodetectors, transistors and switching diodes that can be integrated in one of the described pixel structures. A new recipe for gate dielectric deposition was developed. It can be easily implemented in a wide range of device manufacturing where the only alcohols or nitriles are borne. Direct-written, semitransparent organic pixel were fabricated on a flexible substrate and characterized. In particular double diode architecture not only is the simplest but also exhibits noteworthy performances. The results show that is possible to explore the realization of an imager composed with the presented pixels. An optimized stacked structure should be fabricated in order to properly compare it with the other two kinds. Some effort should be put in understanding of discrepancy between prediction and result of maximum acceptable delay. Being the switch resistances far from specifics future work should be devoted to the optimization of direct-written addressing elements.

3.4 Direct-written matrix

Basing on the good results shown so far an attempt to build a direct-written matrix was done. The direct-writing approach makes it easy to replicate the same unit many times without increasing process complexity. Consequently a

(a)

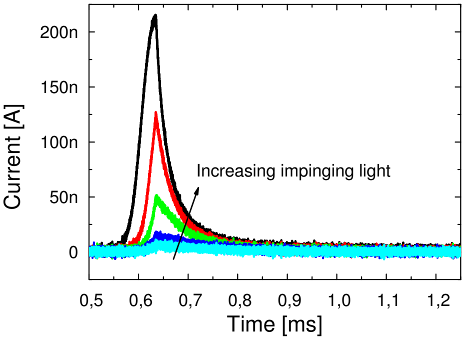

(b)

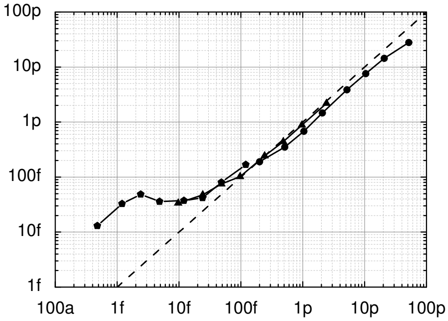

(c)

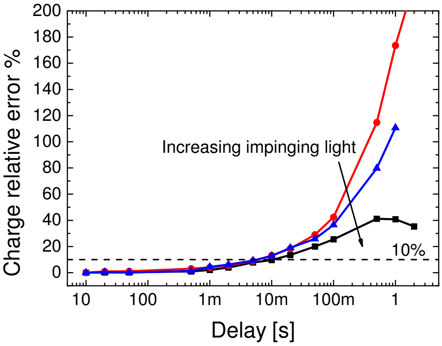

Figure 3.15: Double diode output current at different impinging light powers (a), measured photocharge vs. number of impinging photons (b). Dashed line represents the 1:1 input/output relation. (c) Charge loss varying the delay between light exposure and readout for a double diode pixel. Delay measurement was done at three different amount of photogenerated charge: $6.5pC$ (red), $9.4pC$ (blue) and $14.9pC$ (black).

direct-written pixel as the one presented before (sec. 3.3.1) can be replicated easily in a matrix structure without the need of further optimization. We adopted the coplanar as pixel structure.[2]

In order to realize an image sensor pixels have to be connected as explained before (sec. 3.2). Inkjet printing can cope with the realization of interconnections too. Where horizontal and vertical lines cross parasitic capacitors are present: an attention should be put on those areas because they could be source of leakage and raise capacitive coupling and system noise.

Modulation transfer function (and DQE for X-ray applications) should be evaluated after a careful design of the whole system because strictly related to the pixel geometry and arrangement, the overall front-end electronics (and the scintillator). The optimization modulation transfer function (MTF) and detective quantum efficiency was not the purpose of this study which focuses mainly on obtaining a correct behaviour from the image sensor.

3.4.1 Matrix building

Before pixel fabrication vertical silver lines were printed and sinterd using TEC-IJ-010 ink. They will serve as column lines, connecting transistor drain electrode to the column pre-amplifier, and common polarization lines, to keep the detector anode biased negatively with respect to amplifier virtual ground. Being these lines quite long ($\sim 1cm$) the adoption of silver ink to print vertical interconnections allows to maintain low the parasitic line resistance. Then we realized a 5×5 matrix of coplanar pixels spaced by $2.2mm$ in both directions. Before connecting the gate electrodes 6 layers of PMMA dissolved in polycarbonate (PC) and IPA ($7:3$) at $40mg \cdot mL^{-1}$ were inkjet printed on crossing points in order to strength the dielectric and to reduce the parasitic capacitance resulting from lines overlap. Each layer was printed $180s$ after the previous one, viz. when the antecedent is partially dried. Then gate connections were printed horizontally with P JET 700. After moving the image sensor inside a glovebox we performed a thermal annealing of $1h$ at $100°C$. A row and a column of isolated pixels and single devices were realized in parallel to the matrix fabrication for check tests. Figure 3.16 shows the complete layout of the fabricated direct-written matrix and a photo of the final product.

The matrix was exposed to LED light at $525nm$ coupled by mean of a plastic optical fibre ($2mm$ diameter, 02-551 Edmund Optics) placed $\sim 1cm$ apart from the matrix in order to have a light spot as large as the matrix. An 8-channels waveform generator (WFG600 from FLC electronics) was used as row driver. Four charge pre-amplifiers with feedback capacitor $C_f = 1pF$ and

---

[2] Even if double diode pixel is outperforming the others it was developed at last, thus there was no time to fabricate a matrix based on this architecture.

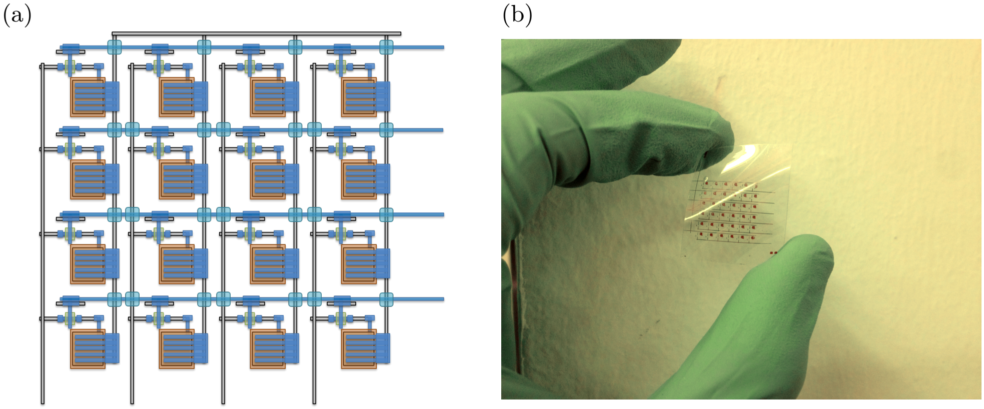

Figure 3.16: Layout (a) and photograph (b) of the direct written matrix realized. In blue is depicted PEDOT:PSS, in grey silver, in orange P3HT:PCBM blend, in green N2200 and in bluish green PMMA thikenings.

resistance $R_f = 100M\Omega$ were used in parallel to read columns output. Preamplifiers were biased between $6V$ and $-6V$, virtual ground stays at $-3.2V$ in polarization. The pole of the amplifier has a time constant equal to $100\mu s$. We wrote a LabView program controlling signal timing and acquisition. Dark reference subtraction and post processing were done by software.

3.4.2 Results and discussion

3.4.2.1 Preliminary tests

First of all, single devices were checked to validate the process. Photodetectors dark current is around $100pA$ corresponding to $160nAcm^{-2}$, being devices areas of $(250\mu m)^2$. Its EQE is above 40% for wavelengths below $600nm$. The transistors exhibit off-current of $\sim 100pA$ and $R_{ON} < 200M\Omega$. The comparison between this test devices and the ones realized with single pixel process (tab. 3.2) shows some differences: dark current and EQE are higher for the matrix test structures while for transistor R_{ON} and R_{OFF} is the opposite.

PD capacitance value is around $14pF$ (eq. 3.1). With these values the estimated readout time is of $14ms$ (calculation performed as in tab. 3.2). PD dark current and TFT channel leakage current have almost the same value but acting in opposite way, the first discharging the latter recharging PD intrinsic capacitor, they tend to cancel out. In this situation it is not trivial to determine the maximum delay time by simple calculation.

In fig. 3.17 optical micrograph and profile of strengthen isolations are reported. The thickness of the printed PMMA exceeds $500nm$ with an almost

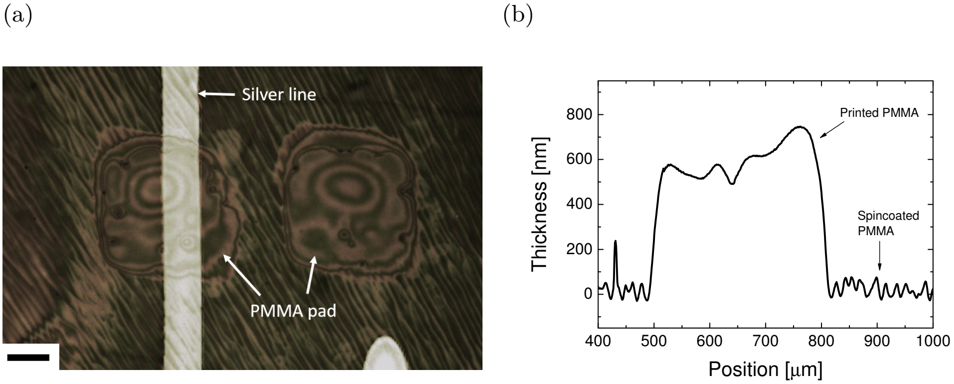

Figure 3.17: Optical micrograph (a) and profile (b) of a PMMA two pads printed to strengthen the dielectric a crossing point of horizontal and vertical lines. Scalebar = $100\mu m$.

rectangular profile. P JET 700 horizontal lines present no issues to climb over the printed PMMA pad without breaking up. The $500nm$ of the thickening add to the $450nm$ of the spincoated dielectric separating horizontal lines from vertical one of almost $1\mu m$. Thickened crossing points are able to sustain $10V$ without leakages and have a capacitance of $\sim 450\text{f}F$ in accordance with the estimate of $500\text{f}F$ assuming an approximation of parallel plates capacitor.

The matrix has a non-optimized pixel pitch of $2.2mm$ which results in an optical cut-off frequency of $\sim 0.22\text{cycles} \cdot mm^{-1}$. It must be noticed that the overall pixel dimensions were not as shrunk as possible, therefore the geometrical fill factor is very poor and the pixel pitch large. Nevertheless, this allows to partially relax the request on layer-to-layer registration preferring to focus the attention on devices electrical performances.

3.4.2.2 Matrix readout

To readout the matrix we polarized gates at $-8V$ and at $10V$ to keep TFTs in off- and *on*-state respectively. PDs anode is biased at $-4.5V$, i.e. $-1.3V$ with respect to pre-amplifier virtual ground. Gates are driven with trapezoidal pulses with $5ms$ as *on*-time and rise and fall time of $2.5ms$ each. Between the switch off of a line and the switch on of the following there are $100\mu s$, which are negligible compared to pulse width. Before exposure to light, all pixels are reset by applying a gate pulse on every row at the same time. This operation puts the matrix in the correct starting state (sec. 3.2). To remove the offset due to dark/leakage currents and charge couplings dark signals are acquired and subtracted from light acquisitions.

Among the 25 pixels of the matrix only 6 operate properly detecting im-

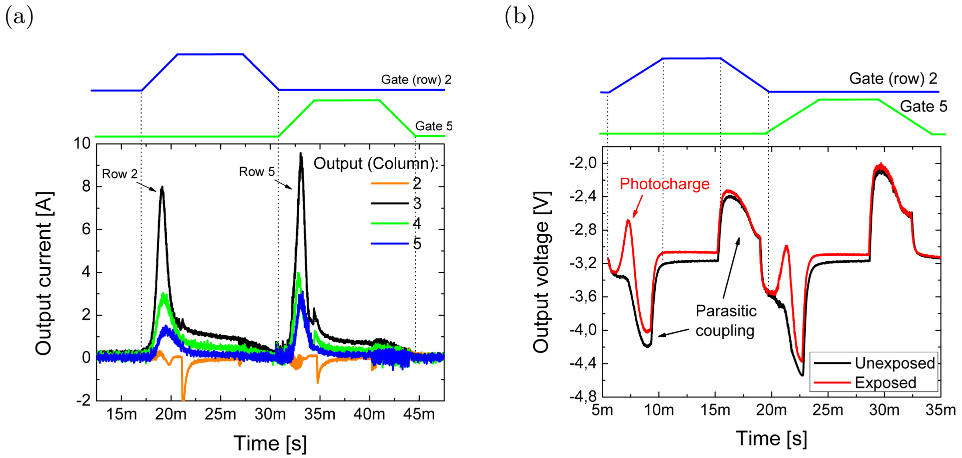

Figure 3.18: (a) Current waveforms recorded during the matrix readout process corrected for the ones measeured keeping the matrix in dark condition by dividing the pre-amplifiers output voltage by R_f. (b) Voltage waveforms recorded at pre-amplifiers output during two matrix readout processes one with the matrix kept in dark and the other subjected to light exposure. When gate voltages rise the charge coupling through parasitic capacitors can be seen affecting the signal.

pinging light, while for one, even if it shows a response to light, the gate pulse causes pre-amplifier saturation leading to non-ideal signal reconstruction. This large coupling cannot be explained with an increase of the overlapping area between gate and source/drain being the three electrodes as wide as the others. A dielectric local imperfection might be the reason for the increased parasitic capacitance. Of the non-working pixels two were damaged by dust particles, one resulted unconnected because of misaligned gate printing and the others had large gate leakage. In order to preserve the behaviour of the others they were manually isolated scratching their interconnection with probe station tips. For sure, an improvement of the process yield must be an aim of future developments.

Pre-amplifier output voltage waveforms corrected for dark are reported in fig. 3.18a. The first and the second peaks correspond to the readout of the two rows while the three different traces are the columns outputs. Each pixel is subjected to an unknown amount of impinging photons thus it is not possible to draw the measured vs. theoretical charge plot with complete certainty.[3]

---

[3] Measures here reported were taken employing a setup still under development. In that arrangement optical fibre and matrix were not fasten to a common frame and the light beam not collimated. An improved version of the measurement system was designed and produced to solve these issues. Impinging light was calibrated finding that the intensity of the collimated beam is of $0.35 mW \cdot cm^{-2}$.

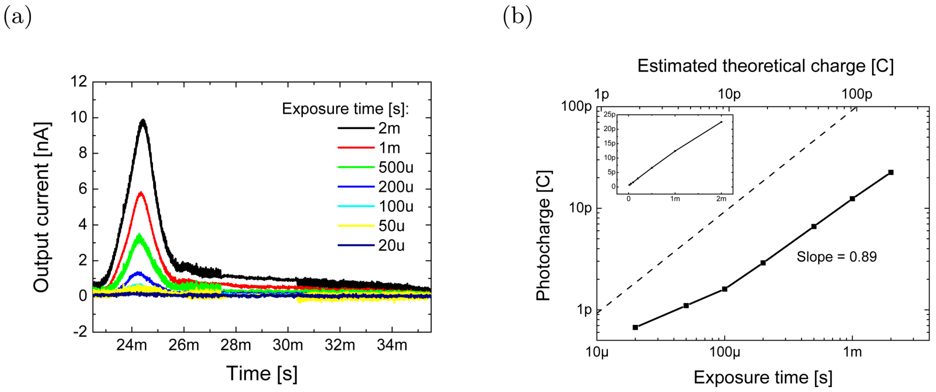

Figure 3.19: Voltage waveforms recorded at a pre-amplifiers output during the matrix readout process changing the exposure time (a) and corresponding measured charge (b) vs. duration of exposure.

For sure the statistical spread of pixel characteristics has a role in differences between displayed waveforms.

Even if in a matrix more parasitic effects come into play, it is worth to notice that they do not compromise the signal readout. Specifically, capacitive coupling is not detrimental for columns 3, 4 and 5 (fig. 3.18b). On the other hand column 2 is affected by pre-amplifier saturation caused by charge coupling as stated before: a small signal is visible but its shape denotes the reaching of saturation and then the recover to acceptable range. During the readout of one row when the addressing elements switch on a peak is seen for each column and then a charge flows with a slower dynamic. The current returns to zero after almost $20ms$ which is of the same order of what predicted (sec. 3.4.2.1).

The exposure time was changed from $2ms$ down to $20\mu s$ and a column output was recorded to check the sensitivity to light (fig. 3.19a). Time-integrating the output current the measured charge vs. exposure time is derived finding a sublinear dependence between them for the whole range of exposures tested (fig. 3.19b). A consistent signal was recorded from all-over the two orders of magnitude large range of signals tested. Basing on the measured light intensity of the second version of the setup a rough esteem the theoretical charge is reported on the top x-axis. Relaying on this approximation the readout charge results below the theoretical one as it was also found for the single coplanar pixel (fig. 3.12b). The range of detected signals spans from 2 to $200pC$ ($1.2 \cdot 10^7 - 1.2 \cdot 10^9$ photons). This range is not suitable to enable organic mammographic screen. The non-linearity of the input/output characteristic is not a problem at first approximation: once calibrated the system

(a)   (b)

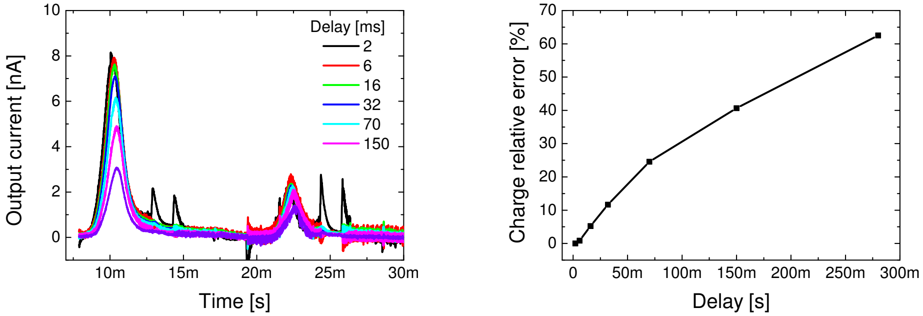

Figure 3.20: Voltage waveforms (a) recorded at a pre-amplifiers output during the matrix readout process changing the delay between the exposure to light and rows readout and corresponding measured charge (b) vs. delay. Spurious peaks clearly visible for the black curve are unrelated with matrix behaviour. They are due to unwanted step signals that sometimes appear at the output of the gate driver when driving voltage has to sharply change its slope.

acquiring its input/output curve for whatever measured charge is possible to derive the impinged amount of photons.

The signal loss increasing the delay between the exposure to light and a row readout was experimentally derived (fig. 3.20). As already noticed for single pixels coplanar structure has readout times in the order of tens of ms. The same is found for matrix readout (no limitation is introduced by the pre-amplifier): from fig. 3.18 it can be clearly seen that after $10ms$ the current is still higher than the zero value, therefore gate pulses should be extended more. However, this results in an increased readout delay for the following row which will be affected by a larger error. Keeping the reading time $10ms$ long allows to read almost correctly the second line too (fig. 3.20). Assuming a 10% maximum acceptable loss three more lines can effectively be addressed if the process yield would be higher.

3.5 Conclusive remarks

This work demonstrates the possibility to fabricate an imager prototype of interconnected semitransparent organic pixels realized by inkjet printing and femtosecond laser ablation. The versatility of the fabrication approach used was a great advantage for the improvement of performances and to achieve the goal. The overall thermal budget is limited (maximum temperature of $120°C$) and the material waste low. No vacuum technique or mask was used. The flexibility and lightweight of the substrate are other key features. Fabrication yield and characteristics of single components were enough to operate the matrix and to acquire signals from 6 pixels covering two order of magnitudes of impinging light intensity.

The further development of this research could benefit industrial non-destructive testing, medical imaging and homeland security fields. In particular it should be put effort on increasing the spread between *on*- and off-state resistance of the addressing element in order to speed up the readout and to allow to read a larger number of rows. Then the process yield should be increased and overall pixel dimensions shrunk. MTF and DQE must be evaluated.

Part II

Organic Photodetectors for specific needs

Chapter 4

Inkjet printed polymeric electron blocking and surface energy modifying layer for low dark current organic photodetectors

The reduction of dark current is required to enhance the signal-to-noise ratio and decrease the power consumption in photodetectors. This is typically achieved by introducing additional functional layers to suppress carrier injection, a task that proves to be challenging especially in printed devices. In this chapter we report on the successful reduction of dark current below $100nA \cdot cm^{-2}$ *in an inkjet printed photodetector by the insertion of an electron blocking layer (EBL) based on poly[3-(3,5-di-tert-butyl-4-methoxyphenyl)-thiophene] (poly-PT), while preserving a high quantum yield. Furthermore, the EBL strongly increases the surface energy of the hydrophobic photoactive layer, therefore simplifying the printing of transparent top electrodes from water based formulations without the addition of surfactants. We will describe the fabrication of photodetectors and the features of the electron blocking layer will be analysed with respect to the ones presented so far.*

4.1 Introduction

Nowadays photodetectors are used in many electronic systems ranging from telecommunications, imaging and security fields. In particular, emerging wearable and disposable applications require low cost manufacturing, large area fabrication, mechanical flexibility and lightweight which are features hard to be obtained with silicon technology. Additive, cost-effective, scalable printing techniques (e.g. roll-to-roll, inkjet printing, screen printing, spray coating) are perfectly suitable for to develop large-area, distributed, complex optoelectronic systems.[49,135] Among printing technologies, inkjet offers the capability of transferring a digital pattern directly and without contact on a variety of substrates and it is an easily customizable technique.[77] In order to develop printed devices that cope with aforementioned needs functional inks of organic materials are good candidates, thanks to their peculiar features such as solution processability, chemically tailorable properties, abundance of primary materials, mechanical flexibility.[75] In the field of light sensing, some examples of printed photodetectors have been already reported,[136–139] yet the constraints related to the inkjet printing manufacturing resulted in some issues and/or in a trade-off between device complexity and device performances. Indeed, in addition to the photoactive layer(s) and to the charge collecting electrodes, a photodetector ideally requires additional layers – termed hole and electron blocking layers (HBL and EBL) – in order to suppress the injection of dark current, which otherwise limits the minimum detectable signal and increases power consumption.[3,49,78,140–145] The development of printable HBLs and EBLs is a non-trivial task, because each ink has to be tailored with proper rheological characteristics, and come from orthogonal solvent respect to the underlying layer, in order to wet but not to dissolve/damage this latter.

Here we exploit a suitably synthesized polythiophene derivative to develop an EBL that both reduces the dark current and strongly increases the surface energy of the hydrophobic photoactive layer used. As a result of the introduction of such EBL, we demonstrate a reduction of the dark current density below $100nA \cdot cm^{-2}$ while preserving a high quantum efficiency above 65%. Moreover, thanks to the increased surface energy, the top anode contact can be directly printed from a water a based poly(3,4-ethylenedioxythiophene):poly(styrenesulfonate) (PEDOT:PSS) formulation. This is advantageous because PEDOT:PSS water-based inks poorly wet the usually hydrophobic underlying photoactive layer. To overcome this issue a surfactant is often added,[58] even in high amount,[136] but this complicates the ink formulation and in addition the surfactant effects on PEDOT:PSS electronic and mechanical properties and ultimately on the device performance are still poorly understood.[13]

4.2 Experimental

Reference samples were prepared similarly to the ones reported in ref.[136]: polyethylene naphthalate (PEN) (DuPont) was used as substrate, silver TEC-IJ 060 (InkTec) ink was printed with Dimatix DMP2831 with $10pL$ nozzle and sintered in air at $140°C$ to realize aligning reference marks and easy contactable electrical probe points. Clevios P Jet 700 N (Hereaus) PEDOT:PSS ink was filtered with $0.2\mu m$ PVDF filter and printed with DMP2831 $10pL$ cartridge. The HBL was realized using polyethylenimine branched (PEI) (Sigma Aldrich) diluted in 2-methoxyethanol to $0.1w\%$ concentration and spin-coated over the bottom contacts at $5000rpm$ ($1000rpm/s$) for 1 minute. Poly(3-hexylthiophene) (P3HT) ($RR = 96.6\%$, $MW = 65500$) was purchased from Merck, and [6,6]-phenyl-C61 butyric acid methyl ester (PCBM) (purity $> 99.5\%$) was purchased from Solenne. Both were used as received. P3HT:PCBM (1:1) blend was dissolved in 1,2-dichlorobenzene ($68vol\%$) and mesitylene ($32vol\%$) solution and stirred overnight. The blend solution was heated at $80°C$ for 10 min and filtered with a $0.20\mu m$ PTFE filter and inkjet printed with a Microfab JETLAB 4 equipped with a $40\mu m$ diameter DLC nozzle. Clevios P Jet 700 N was printed over the blend with Zonyl FS-300 fluorosurfactant (Sigma Aldrich) added to the fluid ($10wt\%$).

For the EBL poly[3-(3,5-di-tert-butyl-4-methoxyphenyl)-thiophene][146] (poly-PT) was synthesized by Letizia Colella. For the fabrication of devices with EBL, $4mg$ of poly-PT, extracted with n-hexane, were dissolved in $1mL$ of n-butanol:ethylene glycol (9:1) and heated at $70°C$ for 1 hour. The ink was heated at $80°C$ for 10 minutes before use and filtered with a $0.45\mu m$ PVDF filter. Poly-PT was printed on P3HT:PCBM by means of a DMP2831 inkjet printer equipped with $10pL$ nozzles on top of the active blend or spin-coated in three steps ($200rpm$, $100rpm/s$, $6s$; $1000rpm$, $200rpm/s$, $80s$; $5000rpm$, $1000rpm/s$, $60s$). On top of poly-PT, Clevios P Jet 700 N was printed with or without Zonyl FS-300. We realized the following device configurations by keeping the bottommost layers fixed, viz. PEDOT:PSS/PEI/P3HT:PCBM and changing the topmost ones (fig. 4.1d):

(a) ../poly-PT spin-coated/PEDOT:PSS

(b) ../poly-PT printed/PEDOT:PSS+Zonyl

(c) ../poly-PT spin-coated/PEDOT:PSS+Zonyl

(d) ../PEDOT:PSS+Zonyl

(e) ../n-butanol:ethylene glycol/PEDOT:PSS+Zonyl

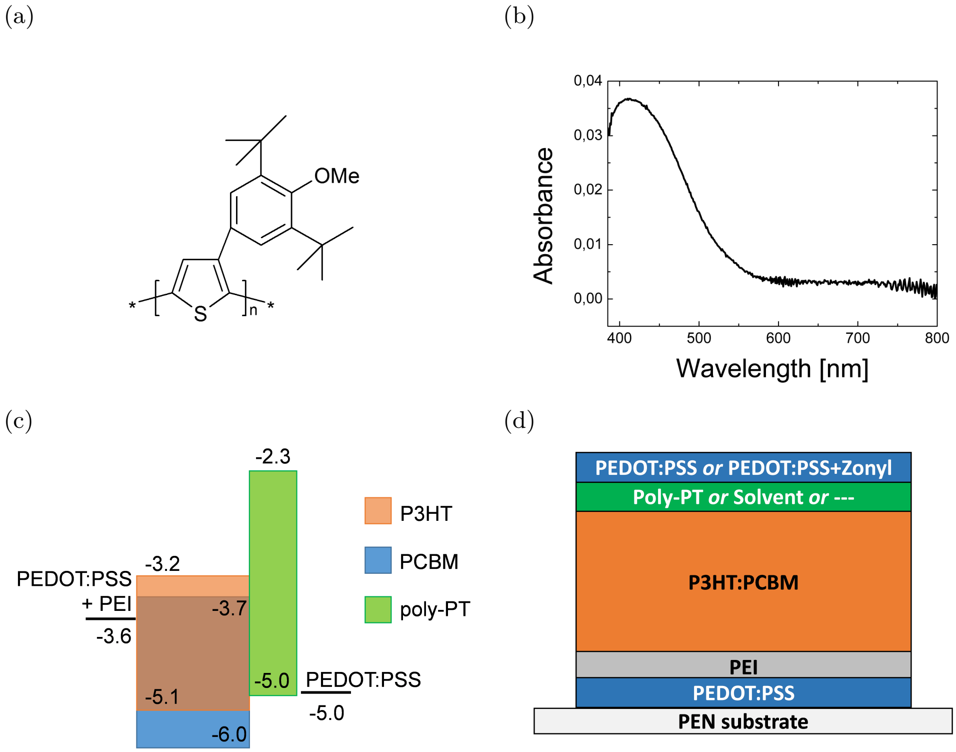

Figure 4.1: Chemical structure (a) and absorption spectrum (b) of LC153 polymer. Energy levels scheme (c) and structure of the device (d).

The entire manufacturing process was carried out in ambient condition. Poly-PT was characterized through Bruker NMR ARX400. Profiles were measured by stylus profilometry (KLA Tencor Alpha-Step IQ). A Varian Cary 50 Spectrophotometer was used to measure layer absorbance. Contact angles were measured using a Dataphysics OCA 15EC. Current-Voltage (I-V) measurements were recorded in a nitrogen-filled glove box in dark and under white light ($6400K$, about $3mW \cdot cm^{-2}$) on 9 devices, voltage bias applied to the bottom contact. External Quantum Efficiency (EQE) spectra were recorded at about $1mW \cdot cm^{-2}$ in glovebox. EQE spectra and power dependences were taken with the device under test reversed biased, grounding the top electrode and applying $1V$ to the bottom one.

All depositions were carried out in ambient condition. Profiles were measured by stylus profilometry (KLA Tencor Alpha-Step IQ). A Varian Cary 50 Spectrophotometer was used to measure layer absorbance. I-V in dark and under white light ($6400K$, about $3mW \cdot cm^{-2}$) and external quantum efficiency (EQE) measurements were performed in glovebox, positive polarization applied to bottom contact. EQE spectra were recorded at about $1mW \cdot cm^{-2}$. EQE spectra and power dependences were taken applying a reverse bias of $1V$ on the devices.

4.3 Results and discussion

The poly-PT was chemically engineered to act as an EBL for a P3HT:PCBM blend based photodetector in the device configuration showed in fig. 4.1. On one hand the presence of the bulky 3,5-di-tert-butyl-4-methoxyphenyl induces distortion of the backbone, thus leading to a short conjugation length (i.e. large energy gap) and a LUMO level (lowest unoccupied molecular orbital) at $-2.3eV$; on the other hand the HOMO level (highest occupied molecular orbital) is located at $-5.0eV$, in order to allow efficient holes collection from P3HT.

The raw poly-PT obtained by precipitation from methanol was fractioned by hot extraction with two different solvents (i.e. n-hexane and chloroform). The fraction of poly-PT recovered from n-hexane was chosen as it was soluble in many organic solvents. A proper solvent choice allowed the formulation of a printable ink orthogonal to the P3HT:PCBM-based blend. Different classes of solvents have been tested to assess possible dissolution or modification of the P3HT:PCBM layer. N-alkanes and ethers led to a decrease of the photoactive layer thickness, whereas alcohols have demonstrated to be a convenient choice. Among these, isopropanol and hexanol were ruled out for the device fabrication because the low boiling point of the former led to nozzle clogging related to fast solvent evaporation at the orifice, while the high boiling point of the latter left the deposited layer wet even after two hours at room temperature. These two issues were overcome using n-butanol as main solvent and obtaining an ink with boiling point in between the isopropanol and the hexanol ones.

The devices were fabricated in a vertical structure with the photoactive blend sandwiched in between two printed PEDOT:PSS-based electrodes. Both the top and bottom electrodes are transparent, making possible to imping with light from both sides.[138] In this work devices were tested by shining light from the top side. HBL (EBL) was placed between the bottom (top) electrode and the photoactive material. A reference sample, namely (d), fabricated according to such architecture without the presence of the EBL, shows an EQE peak of 73% at 470 - $505nm$ (fig. 4.2a). The same device displays a dark current density with an average value of $200nA \cdot cm^{-2}$ (best device: $130nA \cdot cm^{-2}$) (fig. 4.2b). Calculated peak specific detectivity (D^*), assuming the shot noise as the dominant component of the dark current, results to be

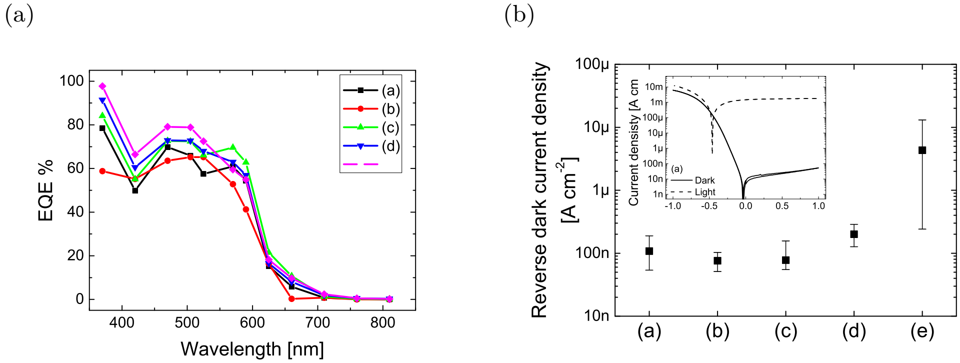

Figure 4.2: (a) EQE spectra of devices (a), (b), (c), (d) and (e) reversed biased at $1V$. (b) Dark current density statistics for fabricated devices measured with a reverse bias of $1V$. Bars indicate maximum and minimum measured values. (Inset) I-V characteristics are reported of the best (a) device in dark (continuous line) and under $3mW \cdot cm^{-2}$ $6400K$ white light (dashed line).

$1.45 \cdot 10^{12}$ Jones under $505nm$ light. EQE and dark current density of these detectors are comparable with the previously reported examples of printed photodetectors and among the best P3HT:PCBM based detectors irrespective of the fabrication technique.[89,94,136,147,148]

Firstly, we investigated the role of the additional layer of poly-PT, either printed or spincoated, comparing devices (b) and (c) to the reference (d) keeping constant the recipe for the other layers, e.g. fluorosurfactant is added to top electrode ink of the three device kinds. For all (b), (c) and (d) devices EQE spectra show values in excess of 65% between $450nm$ and $525nm$ and no significant difference in spectral shapes (fig. 4.2a). This indicates that poly-PT: i) does not sizably affect light absorption, in agreement with its high transmittance in the visible range;[146] ii) does not hinder hole collection, thanks to its HOMO being well aligned with P3HT HOMO. In fig. 4.2b statistical data on dark current density are reported: when the EBL is present, either spin-coated or printed, dark current density is reduced more than twice reaching a mean value of $75nA \cdot cm^{-2}$ (best device: $55nA \cdot cm^{-2}$), with $1V$ reverse bias applied. Calculated peak specific detectivity (D^*) results to be $2.2 \cdot 10^{12}$ Jones for (b) and (c) at $505nm$ light which is 1.5 times higher than the reference (d). We would like to stress that poly-PT improves D^* also when it is inkjet printed, allowing the fabrication of an all-printed device.

In order to discriminate the effect of poly-PT solvent alone from the one of the polymer itself we realized devices (e) by spin-coating n-butanol:ethylene glycol (9:1) instead of the poly-PT solution, setting the same spincoating parameters used for EBL layer deposition. These devices exhibit a dramatic

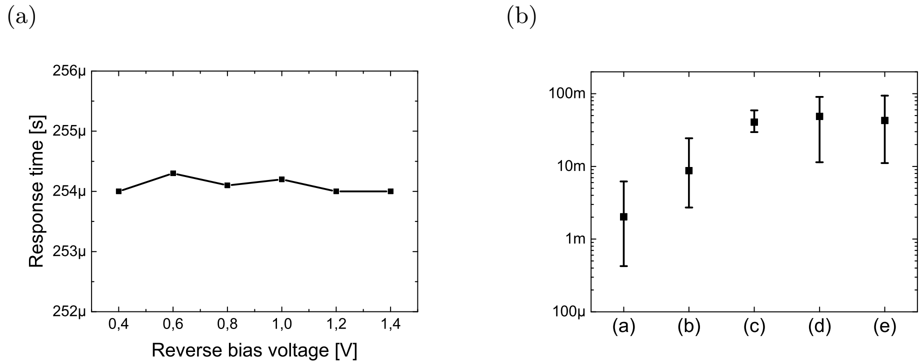

Figure 4.3: (a) Response time measured on device (c) at different reverse bias voltages (impinging light $570nm$, $1.7mW \cdot cm^{-2}$). (b) Dark current density statistics for fabricated devices measured with a forward biased of $1V$. Bars indicate maximum and minimum measured values.

increase of the dark current density mean value and dispersion: these observations highlight that the positive effect on dark current density is due only to the electron blocking polymer and is not related to solvent effect.[148–152]

We have completed the electrical characterization of the aforementioned devices by measuring their response time, extracted as the 90% - 10% photocurrent fall time upon the application of a light pulse. In spite of the improvement on D^*, the detectors with poly-PT layer are slower than the reference sample: the response time is $106\mu s$ for reference devices (d), $136\mu s$ for those with inkjet printed poly-PT (b) and $254\mu s$ for those with spun poly-PT (c). Devices (c) show response time independent of the applied bias (fig. 4.3a). This evidence rules out the transit time as the main limitation to device speed and suggests that those devices operate in a photoconductive regime as confirmed by their EQE being above unity at low light intensity (fig. 4.4a).[153] In printed P3HT:PCBM blends electrons are expected to have larger mobility with respect to holes one.[97] As a tentative explanation for the slower response time of (b) and (c) compared to (d), we hypothesize that poly-PT increases the density of interfacial trapping states for electrons.[98] The difference in response speed of devices (b) and (c) could be possibly related to a different morphology of the printed poly-PT layer compared to the spin-coated one.[154] The choice of printing the EBL instead of relying on spincoating as poly-PT deposition technique has the advantage of faster photodetector response.

I-V curves of device (c) exhibit a dark current density of $40mA \cdot cm^{-2}$ in average ($1V$ forward bias) (fig. 4.3b), which is the same as the reference (d) and ranging among the best P3HT:PCBM based detectors.[89,107] Instead, the forward current density of detector (b) in dark is almost one order of mag-

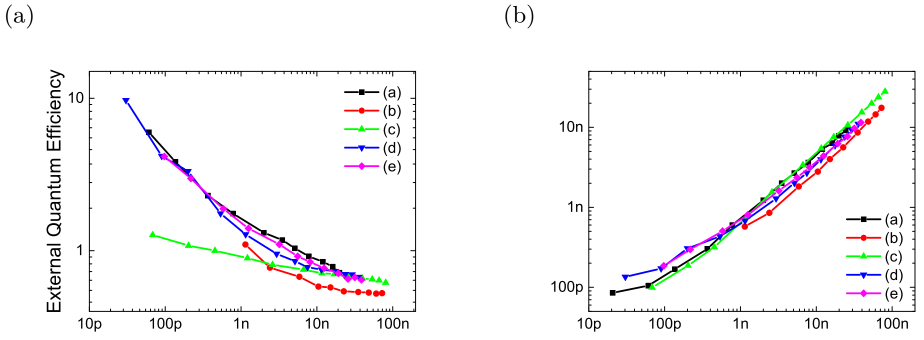

Figure 4.4: EQE (a) and photocurrent (b) versus impinging optical power (measured at 570nm, 1V reverse bias).

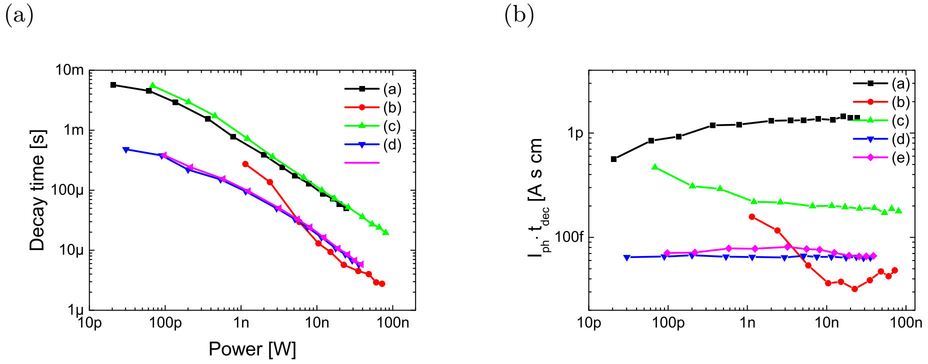

Figure 4.5: Decay time, i.e. the time needed to reduce the photocurrent by a factor e, (A) and photocurrent-decay time product (B) versus impinging optical power (measured at 570nm, 1V reverse bias).

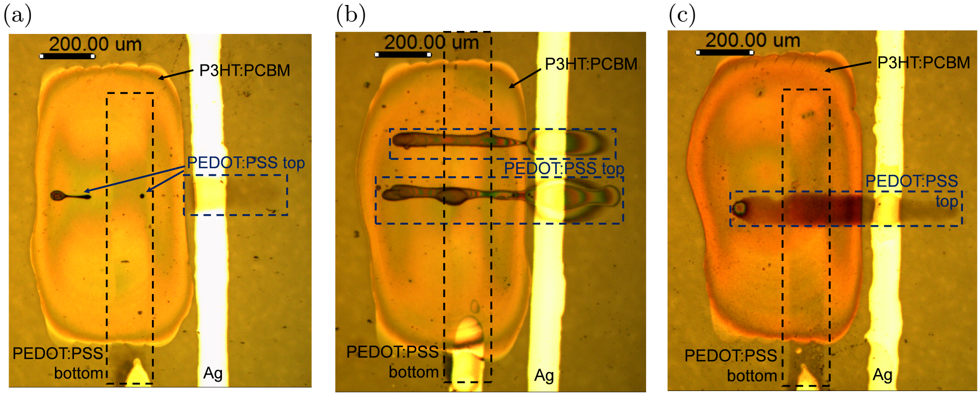

Figure 4.6: Optical micrographs of photodetectors realized without poly-PT nor Zonyl addition (a), without poly-PT with Zonyl addition (b), with poly-PT without Zonyl addition (c). Scale bar 200μm. Dashed lines highlight PEDOT:PSS bottom (black) and top (blue) contacts.

nitude lower. The worse hole injection through the printed poly-PT is likely related to a different thickness or morphology of the printed EBL compared to the spin-coated one.[154]

Finally, we verified that the presence of poly-PT simplifies the deposition of the top anode thanks to its superior wettability with respect to bare P3HT:PCBM blend. Optical micrographs show that Zonyl addition is mandatory to realize a continuous top electrode for photodetectors realized without poly-PT (fig. 4.6a and b), while with poly-PT a continuous top PEDOT:PSS contact can be obtained even without the Zonyl addition (fig. 4.6c). Fig 4.7a and b show the side view of 1μL P JET 700 N droplet dispensed on bare P3HT:PCBM and on the stack P3HT:PCBM/poly-PT. The contact angle is 16° in presence of the EBL while it is 36° without it, demonstrating that bare P JET 700 N can be printed more easily on poly-PT than on P3HT:PCBM. We verified that poly-PT solvent (n-butanol:ethylene glycol (9:1)) alone is not effective in modifying the wettability. We point out that there is no significant difference between samples with (c) and without Zonyl (a) in terms of EQE (fig. 4.2a), reverse dark currents (fig. 4.2b) and response time (fig. 4.5a). Conversely, the absence of Zonyl affects the forward current density that is reduced by a factor 10. These results lead to the hypothesis that different top electrode adhesion is the cause for a worse injection of holes from top contact.

Shelf life was measured for device with printed poly-PT (b) kept in the dark and in nitrogen atmosphere inside a glovebox. I-V curves were measured after 15 months from device fabrication (fig. 4.8). Not only the photocurrent

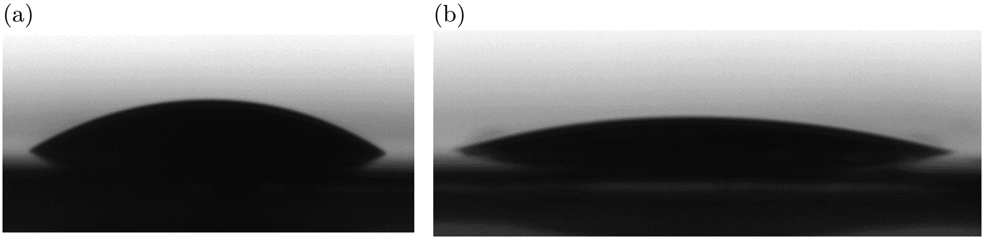

Figure 4.7: PEDOT:PSS droplet on bare P3HT:PCBM (a) and on P3HT:PCBM/poly-PT (b). Contact angles are of 35° and 16° respectively. For contact angle measurements P3HT:PCBM was spincoated on PEN at $1000rpm$, $500rpm/s$, for $60s$.

remains unchanged, but reverse dark current density is reduced reaching the value of $34nA \cdot cm^{-2}$. The light to dark ratio results more than doubled with respect to the first measurement demonstrating no device degradation in controlled conditions.

4.4 Conclusions

Thanks to the insertion of poly-PT as an electron blocking layer and the consequent increase in surface energy, it was possible to fabricate fully-organic, inkjet printed photodetectors where the top anode electrode could be simply processed from a PEDOT:PSS formulation without the addition of a fluorosurfactant. Importantly, the insertion of the printed EBL succeeded in halving average dark current densities, resulting in $75nA \cdot cm^{-2}$, while maintaining EQE as high as 65%. The addition of the printed poly-PT layer mildly affects the device response time, which turns out to be of $136\mu s$. These achievements on printed, semitransparent photodetectors with low dark currents can pave the way for a cost-effective integration of this sensing element in interactive surfaces and imaging systems with challenging SNR requirements such as medical imaging, biosensing and night vision.

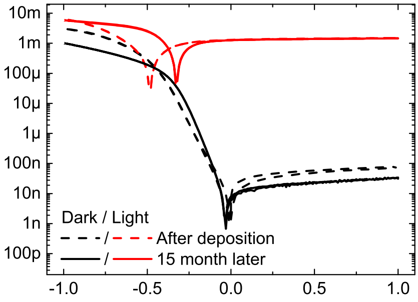

Figure 4.8: I-V characteristics of (b) device in dark (black) and under 6400K white light (red) two days (dashed) and 15 months (continuous) after the deposition.

Chapter 5

Near infrared inkjet printed photodetectors

Hereby inkjet printed photodetectors with sensitivity extended to the near infrared wavelenght is reported. A method that allows to print small molecules is proposed. We will focus both on the manufacturing details and on the electro-optical characterization of the devices. In the last part of the chapter the results of an insight on the role of PFN are reported.

5.1 NIR photodetectors and small molecule devices

NIR-light is fundamental for applications in optical communications,[155,156] remote control applications,[157] and biomedicine.[158] Being infrared photon energies lower than visible ones their collection requires the employment of low band-gap compounds as photoactive materials. Several fields of application[159,160] exploit the near infrared radiation (NIR) and would benefit from the advantages of the organic semiconductors. In last years some examples of organic NIR photodetectors have been reported,[142,161] overcoming known issues regarding synthetic accessibility, chemical stability and solubility of low band-gap materials.[162,163].

In the case of organic photodetectors, all-plastic short range data communication, plastic digital and conformable imagers, position and security sensors, and interactive surfaces become possible.[49] To date the examples of all-printed photoresponsive devices are mainly limited to the case of blends comprising conjugated polymer donors. Semiconducting small molecules are also appealing, as they are not affected by polydispersity and are characterized by a simpler purification technique, which also fulfil the purpose of a better scalability of organic electronics. While inkjet printed blends of semiconducting polymers have already been shown to be reproducible,[154,164] additional issues have to be solved when dealing with the printing of small molecule-based blends. The major problem arises from the strong tendency of such small molecules to crystallize. Crystalline films are desired when the printing is directed to specific functionalities of the organic films, as in high mobility, single crystal organic field effect transistors (OFET).[165,166] Instead in donor acceptor blends a proper phase intermixing is required to improve charge separation.[167] However, the strong tendency of small molecules to crystallize usually limits the control of the uniformity and the reproducibility of the printed film. In fact, a strong tendency to crystallization leads to phase segregation between donor and acceptor components (D-A) in the blend. Such poor intermixing reduces the D-A interfacial area, providing reduced exciton dissociation and therefore charge collection at the electrodes. Also, the presence of large aggregates or crystallites very often increases the roughness of the active materials favouring short circuiting and higher densities of interfacial defects. Furthermore, solutions containing small molecules are characterized by a lower viscosity than polymer solutions, providing a very different rheological behaviour of the printed drop, favouring coffee stain flows.[16,168]

In this part of the work we make use of a recently synthesized narrow band-gap small molecule and we achieve reproducible printing by introducing a semiconducting polymer to obtain a ternary blend. Concerning photoactive blends based on small molecules, this is a quite novel strategy and allowed us to greatly reduce issues related to poor printability and low device performances. We demonstrate an all-organic and fully-printed photodiode, with a spectral responsivity region extending until $750nm$, which thanks to semi-transparent contacts enables double-side signal detection: light detection is indeed demonstrated to occur both when light is incoming from the top and from the bottom side of the photodiode, with comparable efficiencies.

5.2 Experimental

PEN was purchased from DuPont and used as flexible, lightweight and transparent substrate. The synthesis of T1 has already been reported.[169] The silver layer was inkjet printed using a Fujifilm Dimatix $10pL$ cartridge filled with Cabot Conductive Ink CCI-300 further diluted with ethanol and ethylene glycol ($1 : 0.3 : 0.7$), filtered with $0.2\mu m$ PTFE filter. After deposition, two annealing steps were performed in ambient atmosphere, the first one at $70°C$ for 30 minutes, the second one at $140°C$ for 10 minutes. PFN was purchased from Ossila and dissolved in a mixture of methanol ($99.6vol.\%$) and acetic acid ($0.4vol.\%$) to obtain a $1mg \cdot mL^{-1}$ solution which was deposited by spincoating at $2500rpm$ for $1min$ with an acceleration of $1000rpm/s$. The measured thickness of the PFN layer on glass was $5nm$.

7,7'-(4,4-bis(2-ethylhexyl)-4H-silolo[3,2-b:4,5-b']dithiophene-2,6-diyl)bis(6-fluoro-4-(5'-hexyl-[2,2'-bithiophen]-5-yl) benzo[c][1,2,5] thiadiazole) (T1) was used as photoactive donor blended with [6,6]-phenyl-C70-butyric acid methyl ester ($PC_{70}BM$) as acceptor. The concentration of the binary blend of T1 and $PC_{70}BM$ was $35mg \cdot mL^{-1}$ ($21mg \cdot mL^{-1}$ of T1 and $14mg \cdot mL^{-1}$ of $PC_{70}BM$). The ternary blend of T1, $PC_{70}BM$ (purity 99% from Solenne) and P3HT were prepared from a solution of 1,2-dichlorobenzene ($68vol.\%$) and mesitylene ($32vol.\%$) to which a $0.4vol.\%$ of 1,8-diiodoctane (DIO) (Sigma Aldrich) was added. All solvents where purchased from Sigma Aldrich. P3HT ($RR = 96.6\%$, $Mw = 65500\text{Dalton}$) was purchased from Merck. The blend solution was stirred overnight at $100°C$ in glovebox. Before printing, the solution was heated at $70°C$ for 10 min, filtered with a $0.2\mu m$ PTFE filter and then printed with a Microfab JETLAB 4 equipped with a $40\mu m$ diameter nozzle with Diamond Like Carbon (DLC) coating. Clear solutions were obtained upon addition of P3HT, no particulate suspension was present. The new formulation remained clear and stable throughout all the printing time. Clevios P Jet N PEDOT:PSS ink was enriched with Zonyl FS-300 fluorosurfactant, filtered with $0.2\mu m$ PVDF filter and used to load a Dimatix $10pL$ cartridge. The PEDOT:PSS bottom electrode was annealed at $100°C$ for $10min$ before blend printing. Each deposition was performed in ambient condition.

KLA Tencor Alpha-Step IQ was used to measure stripes profile. The UV-Vis absorption spectra were acquired on a Varian Cary 50 Spectrophotometer. IV measurements in dark and under white light ($6400K$, $5mW \cdot cm^{-2}$) were performed in glovebox and acquired with an Agilent B1500A Semiconductor Parameter Analyzer. EQE measurements were performed in glovebox at incident power of about $1mW \cdot cm^{-2}$. Devices were illuminated by a set of Light Emitting Diodes covering the spectral range between $370nm$ and $810nm$. Atomic Force Microscopy (AFM) images were acquired with an Agilent 5500 microscope.

5.3 Results and discussion

Narrow band-gap small molecules have been successfully employed in organic solar cells as they can combine IR photoresponse, high power conversion efficiencies and ease of processability due to their higher solubility with respect to polymers.[29] Recently, a blend of T1 and $PC_{70}BM$ in the presence of the additive DIO has been demonstrated to provide solar cells with power conversion efficiencies of up to 9%.[169–171]

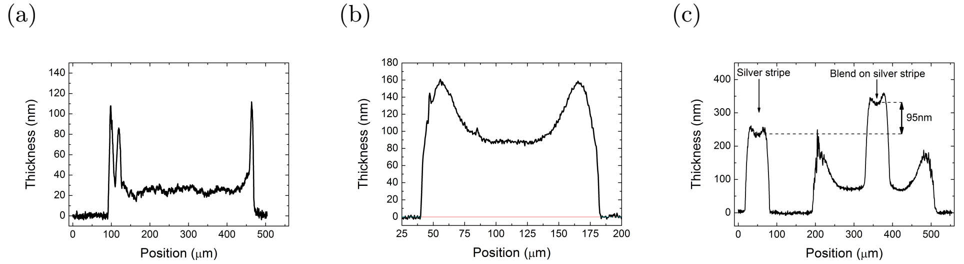

Figure 5.1: Profiles of printed blends. (a) line profile of a printed drop of a binary blend of T1 and PC$_{70}$BM; (b) line profile of a printed stripe of the ternary T1:P3HT:PC$_{70}$BM blend prepared with $5mg$ of P3HT; dissolved in mesitylene-dichlorobenzene solvent mixture; (c) line profile of a printed stripe of ternary blend on a silver stripe. We highlight the strong coffee stain effect observed for binary blends, which is suppressed in the ternary ones.

Firstly, we investigated the inkjet printing of binary blends based on T1 acting as donor and PC$_{70}$BM as the acceptor dissolved in dichlorobenzene-mesitylene solvent mixture. This solvent combination results in a strong coffee stain effect (sec. 1.1.1.2), leaving the central part of the printed stripe thinner than $30nm$, and edges as thick as $80nm$. The binary formulation has also been tested with other solvents as chlorobenzene, but always resulted in a high probability of nozzle clogging due to the likelihood of precipitate formation. The coffee ring effect was difficult to overcome by using a suitable mixing of solvents with different boiling points and surface tensions, which is a strategy commonly adopted in the case of polymer semiconductor blends (sec. 2.2). The profile of the drop obtained by inkjet printing the binary blend T1:PC$_{70}$BM dissolved in a mesitylene-dichlorobenzene solvent mixture is reported in fig. 5.1a. When integrated into a vertical structured device, where the printed layer is sandwiched between two conducting electrodes, such active layers lead to very unstable electrical behaviour, prone to short-circuiting even at low bias voltages, likely due to an active layer too thin to cover the rough silver bottom contact without defects (fig. 2.9 in sec. 2.3.3). The thickness of the layer can be increased by heating the substrate up to $120°C$ during printing. Such a thick film could form thanks to the increased vapour pressure of the solvents at high temperature, favouring the fast drying of the printed drop coming into contact with the hot substrate plate and limiting the spreading of the ink. However, this causes strong phase separation together with the formation of large T1 crystals (fig. 5.2), providing very low device reproducibility.[172] To overcome this issue we adopted a ternary formulation, where an additional photoactive polymer is introduced into the blend to vary the ink viscosity and to reduce small molecule crystallization. To this end we chose P3HT as the semiconducting polymer, due to its capability to par-

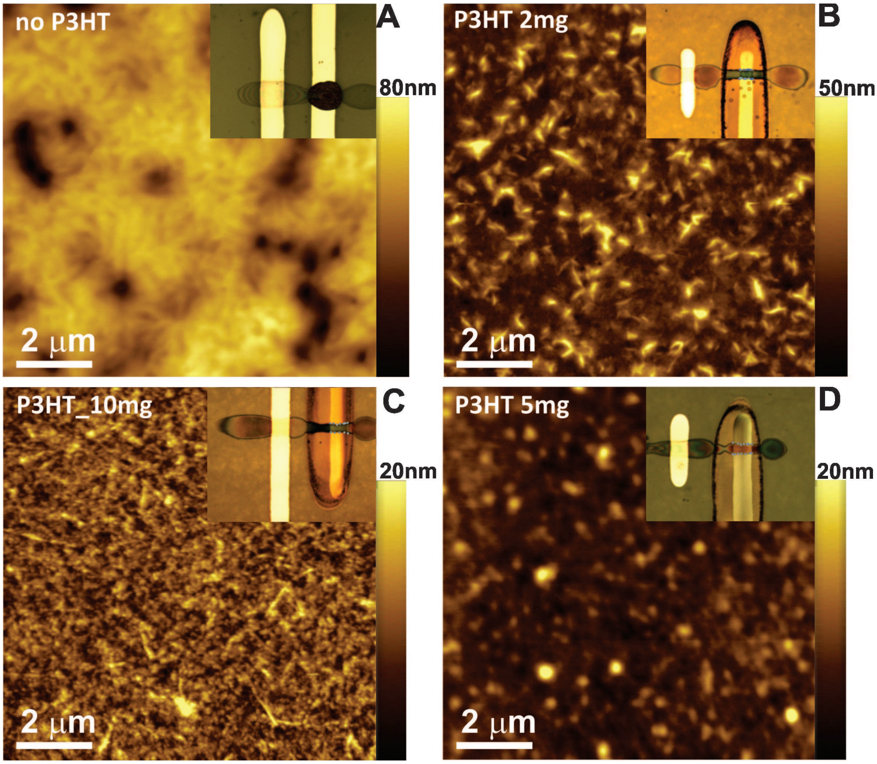

Figure 5.2: AFM images of inkjet printed blends on top of the silver electrode: (a) T1:$PC_{70}BM$ in the absence of P3HT. The substrate was heated up to $120°C$ during printing; (b) T1:$PC_{70}BM$ blend with the addition of $2mg$ of P3HT; (c) T1:$PC_{70}BM$ blend with the addition of $5mg$ of P3HT; (d) T1:$PC_{70}BM$ blend with the addition of $10mg$ of P3HT. Inset: optical microscope images of the printed photodetectors; the brighter vertical stripes are Ag printed bottom electrodes; the horizontal semitransparent stripes are the PEDOT:PSS top electrodes; the blend stripe is printed on top of the Ag electrode (vertical lines in micrographs, in figure (a) the blend is the dark drop).

ticipate to the transport of the photogenerated charges. Also, it is widely commercially available and cost-effective photoactive material providing the possibility to foster a broadband response of the device when combined with T1. The new ternary blend formulation allowed a reduction in the coffee ring effect by favouring a better control on the printing process. This allowed us to reproducibly print blend stripes with uniform thickness of about $100nm$ by holding the substrate at room temperature. Following recent studies presented in the literature,[173,174] we have also explored the possibility to introduce a high molecular weight and insulating polystyrene (PS) polymer to increase the solution viscosity. Huang et al.[173] showed that for low PS concentrations it is possible to improve the thickness, the absorbance and the uniformity of films based on T1:$PC_{70}BM$ deposited by spin-coating. However, by employing a similar strategy we could not easily optimize inkjet printable formulations due to high viscosity. A deeper investigation of the role played by molecular weight and concentration of PS was not the purpose of this work.

Different amounts of P3HT were added to the ternary blend: for a $1mL$ solution we kept the amounts of T1 ($15mg \cdot mL^{-1}$) and $PC_{70}BM$ ($14mg \cdot mL^{-1}$) constant, to which 2, 5 and $10mg$ of P3HT was added (respectively 10%, 26%, 53% weight ratio of P3HT and binary blend). Profiles are reported in fig. 5.1b-c. The concentration of the solutions with P3HT is equal or lower with respect to the one without it. The P3HT addition only cannot be enough to explain the observed thickness increase for the ternary formulation. The improved wetting control and printability of the blend is observed already with very low P3HT concentrations, therefore such an increase of the total thickness cannot be explained by a selective accumulation of the semiconducting polymer. Though in the ternary blend a coffee ring effect can still be observed, the peak to valley ratio and the lateral width of the printed pattern are halved with respect to the one found in the binary blend. These considerations point out that a different wetting and evaporation dynamics are involved for ternary blend printing due to the addition of the semiconducting polymer. The AFM image of the T1:$PC_{70}CM$ photoactive film (fig. 5.2) shows features similar to the ones exhibited by crystalline films of the same materials, as previously obtained by other groups,[172,175,176] leading to the conclusion that also in the printed film of this work the T1 component has a strong tendency to crystallize. By increasing the amount of P3HT an effective morphology variation occurs and the crystallinity of T1 is strongly affected. Crystalline domains are still evident for blends containing 10% P3HT. Their size reduces by adding 26% of P3HT, while they are no more identifiable than for the 53% one. This last ink formulation led to a printed layer morphology with evident fibrillar structures, ascribable to P3HT aggregates.[177] This trend is also confirmed by UV-Vis absorption spectra reported in fig. 5.3, where the main absorption

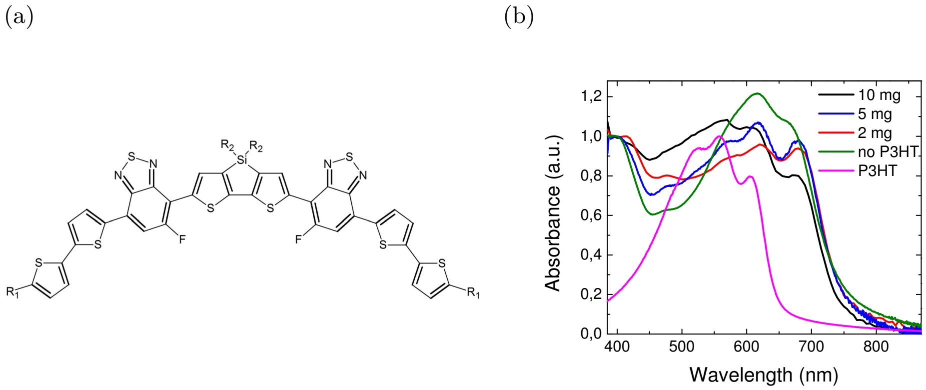

Figure 5.3: (a) chemical structures of T1 (R1 = n-hexyl R2 = 2-ethylhexyl). (b) UV-Vis absorption spectra of the printed blend on a PEN substrate covered with a layer of PFN, normalized at $400nm$. The PEN-PFN absorption has been subtracted as background.

of the T1 around $400nm$ shifts to lower wavelength upon increasing the P3HT content, as expected for a less crystalline film of T1.[172,176]

Though the visible region of the spectra of T1 in the blends overlaps with the P3HT absorption tail, the relative intensity of the peaks around $600nm$ and $700nm$ suggests the same reduced crystallization of T1 when increasing the P3HT content in the blend. This variation in the relative intensity of the peaks at $600nm$ and $700nm$ and the shift in the blue region were already shown for samples of pristine T1 owing to different degree of crystallinity.[176]

Once we optimized the ink formulation, we fabricated the photodetector devices on PEN substrates. The devices have a vertical structure with the photoactive layer placed between two conductive electrodes. Electrodes were realized by printing commercial inks: a silver nanoparticle based ink for the bottom opaque electrodes or PEDOT:PSS for the transparent ones. In all the devices the top contact is a printed PEDOT:PSS electrode (sheet resistance $\sim 5k\Omega/\Box$). Current versus voltage measurements for devices based on printed ternary blends are provided in fig. 5.4a, along with the corresponding External Quantum Efficiency (EQE) spectra in fig. 5.4b-c. The data are compared with a binary blend of P3HT:$PC_{60}BM$ (1:1). Low content of P3HT is responsible for higher instability of devices fabricated with the blend containing $2mg$ of P3HT. A more stable device is obtained by printing a stack of 3 layers of the $2mg$ P3HT blend, its EQE is reported in fig. 5.4c. For photodetectors, the printed bottom electrode was functionalized with PFN by means of spincoating. The introduction of PFN in our devices led to a rectifying behaviour by strongly decreasing the inverse dark current and thus increasing the ON/OFF ratio. Briefly, we could identify an effective hole-injection blocking effect. This

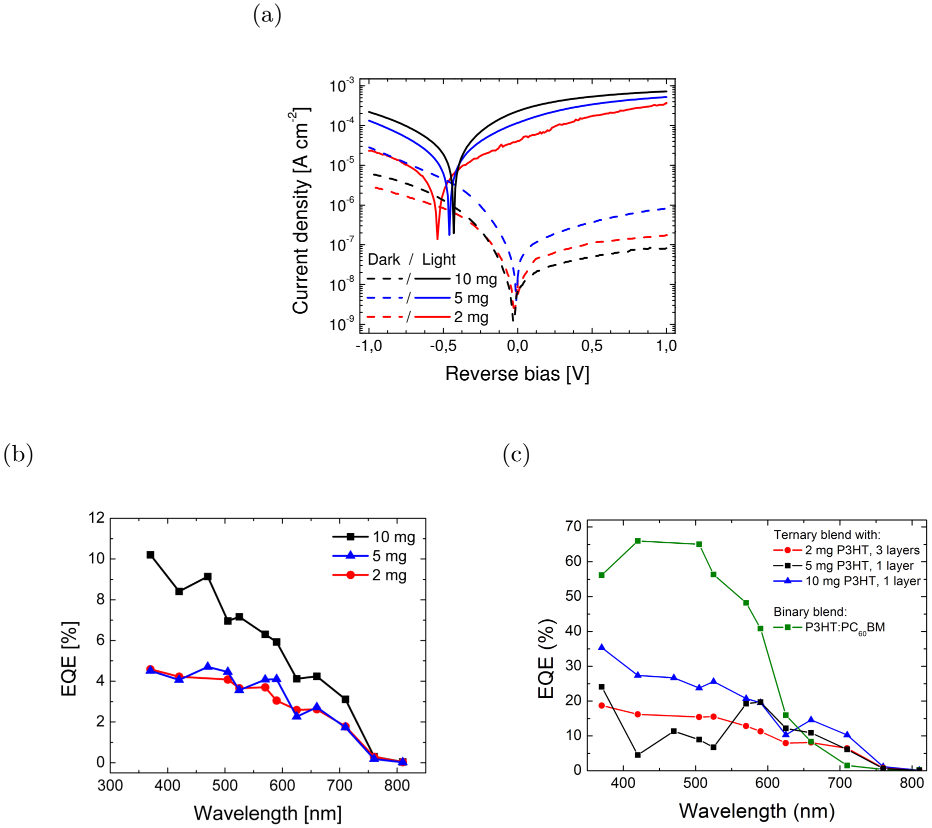

Figure 5.4: (a) Dark (dashed) and white light ($5mWcm^{-2}$) I-V of the devices with printed Ag bottom electrode; EQE spectra at $0V$ (b) and $1V$ (c) for each kind of blend.

conclusion is supported by Kelvin probe measurements where we measured a decreased work-function for both Au and PEDOT:PSS electrodes, following the PFN layer deposition. In the following section (5.3.1) we provide a more comprehensive description of the role played by the PFN interlayer.

Photodiodes made with the 53% P3HT ink formulation showed the best performances in terms of dark current and photocurrent density approaching light-dark current ratio of 10^4, while the V_{OC} is only slightly reduced (fig. 5.4a). Measurements of EQE spectra were performed at $0V$ and $1V$ fig. 5.4b-c. Higher photoresponse in the $650 - 750nm$ region occurs when increasing the P3HT content in the blend. In this region only the T1 is responsible for the light absorption. By combining these data with the observation of a decreased crystallinity of T1, we find, as expected, that the strong tendency of small molecules to crystallize can be a drawback when trying to optimize the photodetector efficiency.

So far we have demonstrated that it is possible to obtain high efficiency in small molecule printed photodetectors through the addition of a semiconducting polymer that inhibits crystallization. To fully exploit the potential of our approach and the added value of organic printing technology, we have optimized an all-carbon based photodetector printed on flexible substrates with semitransparent electrodes.[106] For this goal we replaced the silver bottom contact with a PEDOT:PSS electrode, so that the only non transparent material would be the active blend for which the transparency could be modulated by varying the thickness. Not only does this electrode allow for the semi-transparency of the device, but it also provides a very smooth interface with the organic semiconductor. This feature reduces instabilities due to the formation of leakage paths often observed with the rougher silver printed electrode. The rectifying behaviour and the dark current density, as low as $1\mu A \cdot cm^{-2}$ (fig. 5.5a), shown by these devices, prove that the PFN interlayer is effective in inducing asymmetry between top and bottom electrode work functions as also demonstrated by Kelvin probe measurements (sec. 5.3.1).

Fig. 5.5b reports the EQE measurements acquired with light impinging respectively from the top side and bottom side of the device. We stress that the semi-transparent photodetector responds from both sides to a broad wavelength band up to $710nm$ with an EQE above 10%.

5.3.1 Role of PFN in dark current reduction

From literature it is known that a suitable interlayer can be used in order to suppress the dark current density in inverse polarized photodetectors.[136,142] In this work we employed PFN[178] as an interfacial layer. The efficacy of the PFN as injection layer was already investigated, especially for applications in

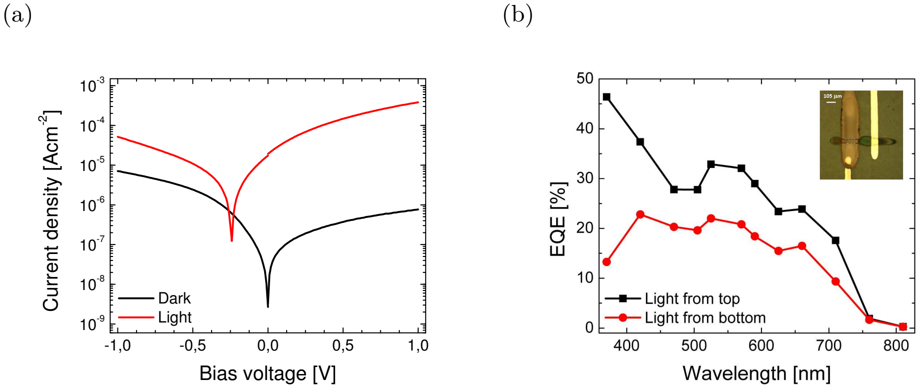

Figure 5.5: (a) Dark and Light I-V of the devices with bottom and top PEDOT:PSS electrodes for blend containing $5mg$ of P3HT. (b) EQE spectra of the device acquired at $1V$ bias, with light impinging either from the bottom or the top side. Inset: optical microscope image of all-organic photodetector. The different values found in the EQE for top and bottom side illumination, is still under investigation. This could be associated with a possible vertical phase segregation of the PC$_{70}$BM to the bottom electrodes acting as a screening for the incoming light reducing the effective photon intensity absorbed by the blend. Also, when shining light from the bottom electrode, the PEN substrate can act as a scattering medium reducing the effective light intensity impinging on the active layer.

the field of Organic Light Emitting Diodes (OLEDs).[179] Some studies could show the variation of the work function induced by the PFN layer on top of substrates like ITO or ZnO.[103] However the microscopic factors which lead to the overall device improvement are still unclear. A fixed dipole moment can effectively lead to a change in the workfunction of the functionalized electrode. Also an induced dipole shielding of the polarization field could lead to a reduced tunneling injection from electrode to the active material.[180] The following study shows the hole blocking capability of PFN, which plays an important role in the reduction of the dark current. The reduced dark current following PFN insertion mainly determines the strong increase in the ON/OFF current ratio of the devices investigated in this work. To explain the PFN role in our printed photodetectors we firstly measured the electrode workfunction with and without PFN layer by Kelvin Probe Microscopy. The data are presented in tab. 5.1. The presence of a top layer of PFN induces a reduction in the work function of $\sim 0.5eV$ for both gold and PEDOT:PSS electrodes. In the case of printed silver electrodes the measurements are more unstable due to the high roughness of the electrodes ($\sim 20-30nm$) leading to easier tip contamination. It is not the purpose of this work to address the specific microscopic mechanism leading to the observed variation in workfunctions.

We also investigated the PFN influence on the dark currents by comparing

Printed electrode	Workfunction [eV]
Au	4.9 ± 0.1
Au/PFN	4.2 ± 0.1
Ag	4.8 ± 0.3
Ag/PFN	4.9 ± 0.3
PEDOT:PSS	5.3 ± 0.04
PEDOT:PSS/PFN	4.8 ± 0.04

Table 5.1: Workfunction of printed electrodes measured by Kelvin microscopy under nitrogen atmosphere. Highly Ordered Pyrolytic Graphite (HOPG, workfuntion = $4.6eV$) was used as reference. The workfunction value is the averaged value measured over different tips and different sample areas. The measurements were performed by using a 5500 Agilent Microscope and Pt coated tips (Micromash, $150kHz$ resonant frequency, $7N \cdot m^{-1}$ force constant).

different device configurations. In particular hole-only devices, made of a gold bottom electrode (vacuum-evaporated, $\sim 2nm$ roughness), were compared with devices including a printed silver bottom electrode and a printed PEDOT:PSS bottom electrode. In all the devices the active blend (T1:PC$_{70}$BM with 26% of P3HT) and the PEDOT:PSS transparent top electrode were printed. Per each bottom electrode, three configurations have been investigated: a- without PFN interlayer; b- with the PFN interfacing the bottom electrode and the blend; c- with the PFN interfacing the top electrode and the blend. Fig. 5.6 shows the measured dark current density of the tested devices; bias is applied at the bottom electrode with respect to the top one and current is measured at the top electrode. Looking at the devices containing gold bottom electrode, we observe that for positive bias, i.e. for holes injected from the gold electrode, the current density (at $1V$) decreases by almost two orders of magnitude when the PFN is present at the bottom interface.

This is consistent with a blocking effect on holes injection. We also notice that when the PFN is at the top electrode, the holes injection from the gold electrode is substantially unaltered for voltages higher than $0.3V$ with respect to the devices without PFN. The lower current density for positive voltages lower than $0.3V$ may be related to an extraction barrier introduced by PFN. If we consider the energy alignment of the HOMO-LUMO levels presented in fig. 5.7, we can explain such different behavior of the PFN at the top and bottom electrode of the Au devices by considering its HOMO energy level, i.e., when PFN interfaces Au electrode, holes injection is hampered by the introduction of an energetic barrier due to the energy HOMO level of PFN.

Also, Kelvin probe measurement show a strong decrease in workfunction

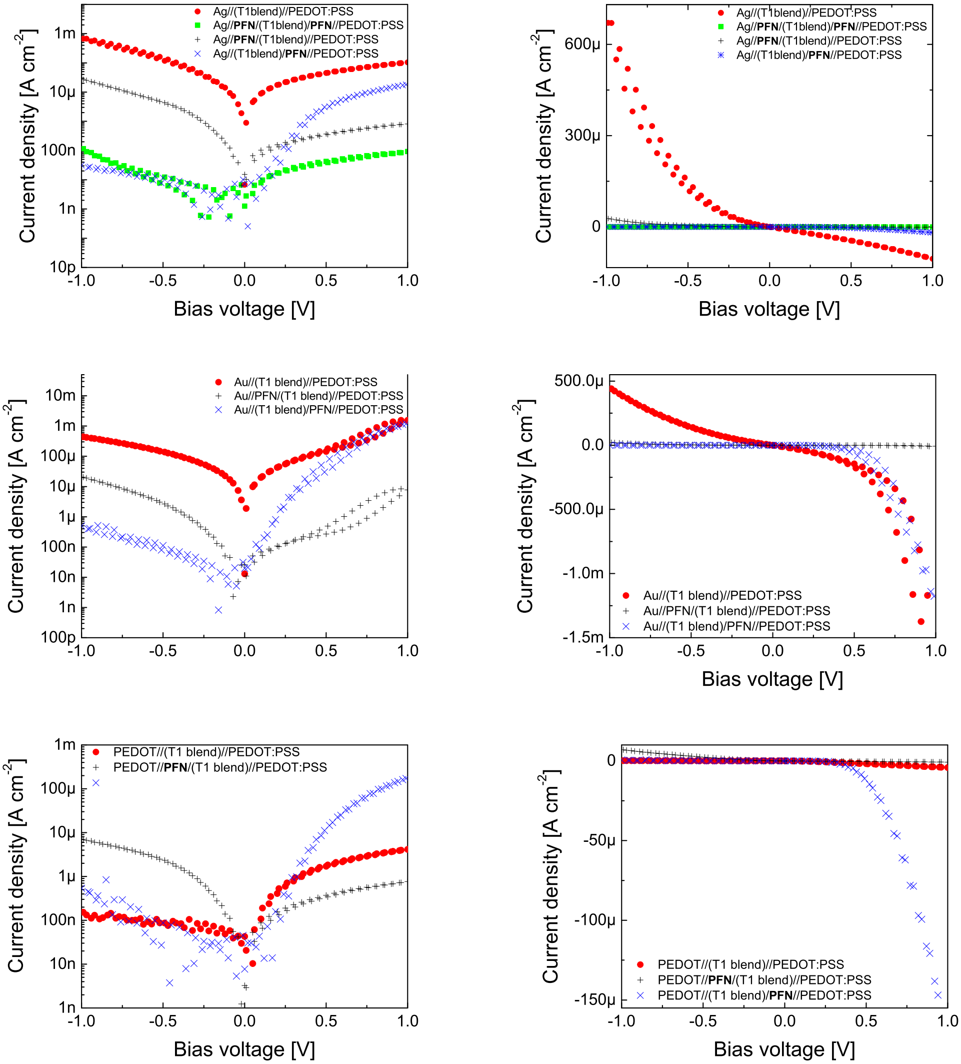

Figure 5.6: I-V plot of the dark currents measured for devices containing either Ag, Au, PEDOT:PSS as bottom electrode and PEDOT:PSS as top electrode. For each bottom electrode three different device configurations have been tested, where the PFN layer was either absent, at the bottom or at the top.

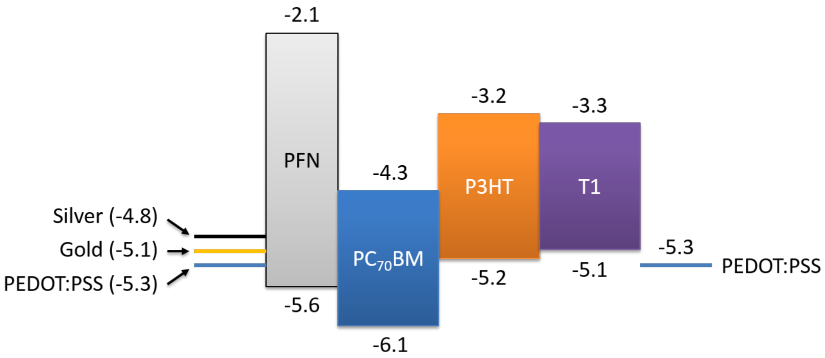

Figure 5.7: Energy diagram of the different electrodes and active materials used in the photodetector fabrication. For gold, silver and PEDOT:PSS we report the energy level as measured with the Kelvin probe microscope under nitrogen atmosphere. The other energy levels reported in the scheme were taken from literature for the pristine PFN, $PC_{70}BM$,[181] P3HT and T1. The effective workfunction measured for PEDOT:PSS/PFN electrode is $4.8eV$ (Kelvin probe, tab. 5.1).

for the gold/PFN electrode, which is consistent with the increase of the injection barrier for holes into the blend active materials.

Looking at the negative biases region, where electrons are injected from the bottom electrodes, and the holes from the top, we find that when PFN is at the top, it effectively blocks holes injection, strongly reducing the current. When it is at the bottom, the current density, while being higher than in the previous case, is again reduced with respect to the PFN free device. Tab. 5.1 shows that since in presence of PFN the measured workfunction for gold/PFN electrode decreases, a better electron injection should be expected as also reported in the literature.[105] The reduced current density indicates that in spite of the strong workfunction decrease, the low mobility of PFN might hamper the electron injection into the active material, suggesting that the current is still dominated by holes, in this case injected from the top PEDOT:PSS electrode. The reduced injection of holes from PEDOT:PSS with the PFN at the bottom may be ascribed also in this case to an extraction barrier.

When considering the dark current for silver devices the same conclusion as for gold can be drawn confirming a similar role played by PFN. The current density found for PEDOT:PSS devices with PFN at the bottom is very similar to the one observed for gold and silver bottom electrodes, both for positive and negative biases. This indicates that PFN introduce a similar blocking effect for holes injection and extraction also in PEDOT:PSS based devices. The rise in the effective workfunction of the new PEDOT:PSS/PFN electrode (tab. 5.1) further increases the hole injection barrier, inferring the electron

Device	$J_{R,Dark}$ $[mA \cdot cm^{-2}]$	$J_{F,Dark}$ $[mA \cdot cm^{-2}]$	Photo/Dark current	V_{OC} $[V]$
Au – a	7.34	0.52	1.3	0.11
Au – b	$10 \cdot 10^{-3}$	$25 \cdot 10^{-3}$	51	0.42
Au – c	$0.34 \cdot 10^{-3}$	0.86	5.8	0.29
Ag – a	0.14	0.73	5.1	0.19
Ag – b	$9.1 \cdot 10^{-3}$	$21 \cdot 10^{-3}$	638	0.45
Ag - c	$4.8 \cdot 10^{-5}$	$58 \cdot 10^{-3}$	95	0.10
PEDOT:PSS - a	$2.7 \cdot 10^{-3}$	$4.1 \cdot 10^{-3}$	13	0.00
PEDOT:PSS - b	$1.2 \cdot 10^{-3}$	$7.4 \cdot 10^{-3}$	372	0.33
PEDOT:PSS - c	$0.19 \cdot 10^{-3}$	5.77	7.2	0.17

Table 5.2: Figures of merit are reported for devices with gold, silver and PEDOT:PSS bottom electrode without PFN interlayer a-, with the PFN interfacing the bottom electrode and the blend b- and with the PFN interfacing the top electrode and the blend c-. J_R and J_F are dark current densities under reverse and forward bias respectively at $1V$ and $-1V$; ratio between photocurrent and dark current values and (V_{OC}) open circuit voltage per each device structure.

injection enhancement and the strong rectifying behavior observed for these devices.

Tab. 5.2 summarizes parameters exhibited by each kind of photodetector.

Combining all the above observations, we can conclude that the PFN interlayer can affect the device performances by varying the electrode workfunction, as shown by Kelvin probe measurements, as well as by acting as a hole blocking layer both for injection and extraction. However, the only workfunction variation does not explain all the observed phenomena and the role played by the PFN poor conductivity associated with its wide bandgap and/or its different thickness and morphology on top of each electrode, has to be called into cause. In fact, such blocking effect can be also attributed to the poor charge transport properties of PFN which constitutes a non-negligible ($5nm$ thick when measured on glass), low mobility layer to be overcome by charges.[104]

We also remind that in presence of acetic acid, the protonated PFN is a cationic polyelectrolyte, i.e. counterion drifting could be possibly foster other possible mechanism as internal field screening or ionic dipole induced phenomena. Time dependent current measurements show that no ionic drifting can be claimed to be responsible for the observed hole blocking phenomena and reduced dark current (fig. 5.8).[182] We would like to stress that such

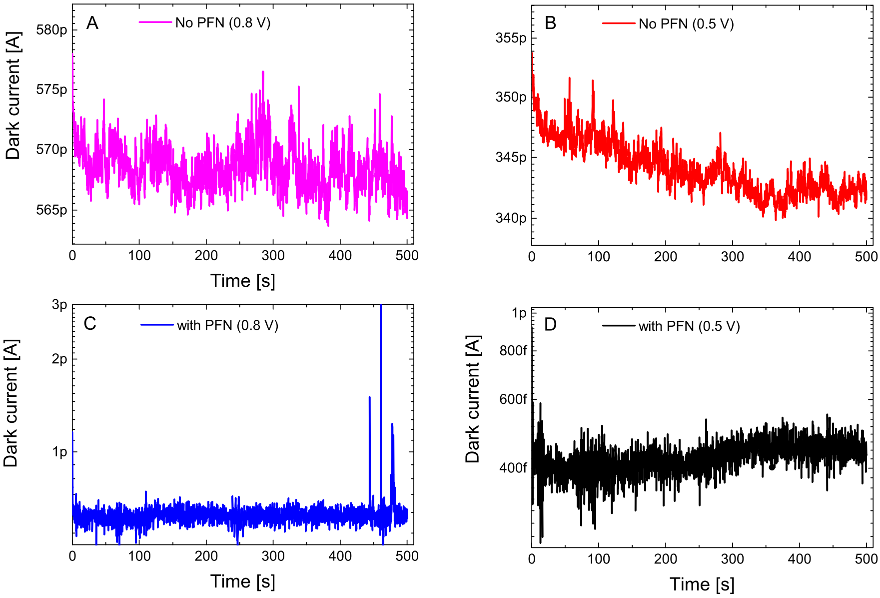

Figure 5.8: Time resolved current dynamics clearly shows the absence of any ions drift mechanism possibly induced by the ionic nature of the PFN in presence of acetic acid (PFN+). The current dynamics have been acquired at constant applied bias of $0.5V$ and $0.8V$.

analysis is valid for the specific thickness of PFN used in the current study ($\sim 5nm$), thicker or thinner layer can show completely different effect on the I-V measurements.

5.4 Conclusions

In conclusion, this work demonstrates the possibility to reproducibly fabricate all-organic and fully-printed, semi-transparent photodiodes on plastic substrates by adopting low band gap small molecule based inks, properly formulated by exploiting ternary blends containing semiconducting polymers. A broad-band wavelength, extending to the NIR range, response could be obtained both when light impinges from the top and the bottom side. Semi-transparent, all-printed detectors can pave the way for a cost-effective integration of innovative light sensing elements in future interactive surfaces, flexible displays, and surveillance systems.

Chapter 6

Planar inkjet printed photodetectors for fully-printed, all-polymer integrated twilight switch

The integration of a fully-printed planar photodetector with printed organic Schmitt trigger is reported in this chapter. At first the fabrication of the light sensor and transistor are presented. Then the circuit rationale is explained dealing with Schmitt trigger working mechanism and the determination of it transition voltages. Satisfying performances of the single devices and trigger are demonstrated by measurements shown. On the basis of those results it was possible to simulate the behaviour of the twilight switch. Finally the validation of the realized system as dusk sensor is proven by full-system measurements.

6.1 Introduction

The tremendous development of organic electronics in the last 30 years can be attributed to the new perspectives envisioned through the study of organic materials. This development is now being enabled for consumer electronics, introducing very interesting properties like flexibility and transparency, along with solution-based manufacturing thanks to cost-effective mass production printing techniques.[24] The main target applications are flexible displays,[183] integrated systems for distributed and wearable sensing and interactive surfaces, with applications in automation, health-care, industrial diagnostic and security. Concerning light detection, organic semiconductors offer several advantages because of their high absorption coefficient and the possibility to finely tune the absorption optical bandwidth.[30,31,33] The fabrication of high quantum yield and semitransparent organic photodetectors by means of printing techniques was been the topic of previous chapters. The only example of their integration in fully-direct-written circuits was presented here (chap. 3).

To make organic electronics suitable for these applications, reliable and robust electronics must be implemented. This can be achieved by following the path paved by the silicon electronics industry which found the best robustness in the development of complementary logic. Although the concept of complementary logic is simple, fabrication of such circuits with organic materials and scalable printing techniques is not straightforward.[184,185] For this reason, most of the organic circuitry in literature is uni-polar,[186] with a direct consequence on circuit performances mainly in terms of power dissipation and area occupation, or includes hybrid approaches for the fabrication in which some of the process steps require, for example, high resolution photolithography.[187] Printing by means of techniques inherited by the graphic arts, i.e. inkjet printing, flexographic printing, bar-coating, rotogravure, etc., would enable industrial mass production with reduced capital investments and limited cost per unit area of the final product. Moreover, depending on the chosen deposition method, it would allow faster customization and time-to-market thanks to the use of digital pattern definition techniques. The step towards all-printed circuits and systems is far from trivial:[24,185] techniques in use still suffer resolution limitations, and the uniformity and yield requirements for industrial production can still hardly be guaranteed. Some recent works have tested different scalable printing methods for the fabrication of organic complementary circuits and have been able to successfully produce devices with good reproducibility and yield.[188–191] On the other hand, these works still suffer some performance limitations in terms of charge carrier mobility or need to include some process steps which are hardly scalable (tab. 6.2). Recently[67] a method to fabricate all-carbon-based, transparent, flexible and all-printed organic field effect transistors (OFETs) and complementary circuits in ambient conditions with scalable production techniques was developed, but a clear demonstration of the feasibility of this method for the fabrication of real-life applications is still lacking.

In this work, after a brief analysis of the fabrication of reliable complementary circuits and photodetectors in a fully-printed approach with all-polymeric materials, we describe their integration into a stand-alone implementation realizing an all-organic integrated photo-active switch on plastic, an application usable in real-life contexts, e.g. for a twilight sensor or for industrial machinery control. The fabricated photo-active switch detects the amount of environmental light power and triggers a digital ON/OFF signal at pre-defined threshold conditions. In particular, the OFF signal is provided when the light power exceeds a pre-set P_{T+} threshold and the ON signal is triggered when the light power drops under a second P_{T-} threshold, with $P_{T-} < P_{T+}$. This feature, intentionally designed, grants an intrinsic immunity to light fluctuations, a feature that may be desirable for particular applications operating in a real-life context. Indeed, a commonly required behaviour for devices responding to environmental stimuli is to trigger their state when a predefined threshold condition is met, and then reject any possible small signal fluctuations, i.e. the devices should hold their new state until the stimulus undergoes a large variation. The photo-active switch described here is provided with this advantageous capability, guaranteeing its suitability for integration in applications requiring the detection of and reaction to environmental light conditions. Here we single out and investigate a possible example: a twilight switch, a device used in outdoor lighting to automatically activate illumination at night or in general when environmental light is lacking. The immunity to fluctuations, which is a key feature in our implementation, effectively rejects small light intensity drops and peaks which are common in a real-life environment, i.e. due to the build-up of clouds or the passage of a body in front of the device.

6.2 Fabrication

Clevios P Jet 700 and Clevios P Jet 700 N were the PEDOT:PSS inks used for the fabrication of transistors and photodetector respectively, both purchased from Heraeus. The Ag-nanoparticles-based ink CCI-300 was purchased from CABOT corp. P(NDI2OD-T2) was purchased from Polyera and diketopyrrolopyrrole-thieno [3,2-b]thiophene (DPPT-TT) was synthesized as in[192]. Poly(methyl methacrylate) ($Mw120k$) was purchased from Sigma Aldrich.

6.2.1 Photodetector fabrication

Photodetector electrodes were inkjet printed using a Fujifilm Dimatix DMP2831 with a $10pL$ nozzle cartridge on bar-coated PMMA. One of the electrodes was coated with a hole injection blocking interlayer by inkjet printing PFN, purchased from Ossila, dissolved at $1mg \cdot ml^{-1}$ in a solution of water ($45vol.\%$), IPA ($45vol.\%$) and ethylene glycol ($10vol.\%$) to which $0.4vol.\%$ of acetic acid was added. The blend ink of P3HT:PC_{61}BM (1:1) was obtained by mixing 1,2-dichlorobenzene ($68vol.\%$) and mesitylene ($32vol.\%$), both purchased from Sigma Aldrich. Before printing with a Microfab JETLAB 4 equipped with a $40\mu m$ diameter DLC nozzle, the blend solution was stirred overnight, heated at $80°C$ for $10min$ and filtered with a $0.20\mu m$ PTFE filter.

6.2.2 Transistor, interconnections and resistances fabrication

The patterning of the source and drain electrodes of the devices and the interconnections was performed using a Fujifilm Dimatix DMP2831 inkjet printer equipped with a $10pL$ cartridge. Five silver reference pads were printed at convenient locations with the same printer, to facilitate the measurement operations. After printing, an annealing step ($110°C$, $30min$) followed. A solution of P(NDI2OD-T2) in mesitylene ($5g \cdot l^{-1}$) was then printed using the same printer in the channel region of the n-type transistors, and an annealing step ($120°C$, $8h$) was performed. Later, a solution of DPPT-TT in mesitylene ($5g \cdot l^{-1}$) was printed in the channel region of the p-type transistors. A $700nm$ thick dielectric layer was fabricated by means of a custom bar-coating apparatus for deposition of a PMMA solution (n-butyl acetate, $70g \cdot l^{-1}$), and a drying step was performed ($80°C$, $15min$). Via holes were chemically drilled by inkjet printing of chlorobenzene. Gate electrodes and top-layer interconnections were fabricated via inkjet printing of PEDOT:PSS ink. Low conductivity Clevios 4083 PEDOT:PSS (purchased from Heraeus) was diluted 7:3 with deionized water as in[193] and used to print the voltage divider resistance.

The layout of the printed patters is reported in fig. 6.1a together with the optical micrograph of the system (fig. 6.1b).

6.2.3 Electrical measurements

The measurement of the circuit voltage transfer curve, as well as the transfer and output characteristics of the single transistor devices, was performed in a nitrogen atmosphere using an Agilent B1500A Semiconductor Parameter Analyzer. Photodetector I-V measurements in the dark and under white light ($6400K$) conditions were performed in glovebox using Agilent B1500A. The overall system was measured by using the B1500A as the voltage supply and recorder while the $6400K$ white light (max power approx. $0.01W \cdot cm^{-2}$) was used for shining light on the device. As a load, an external passive resistance of $1G\Omega$ was employed.

6.3 Circuit rationale

The opto-electronic circuit we realized operates as a photoactive switch, the function of which is to trigger a logic output signal when the amount of light power impinging on the detector exceeds a certain threshold, which can be defined beforehand during the circuit design phase. As an additional feature, this switch, which has a programmable hysteretic threshold, is capable

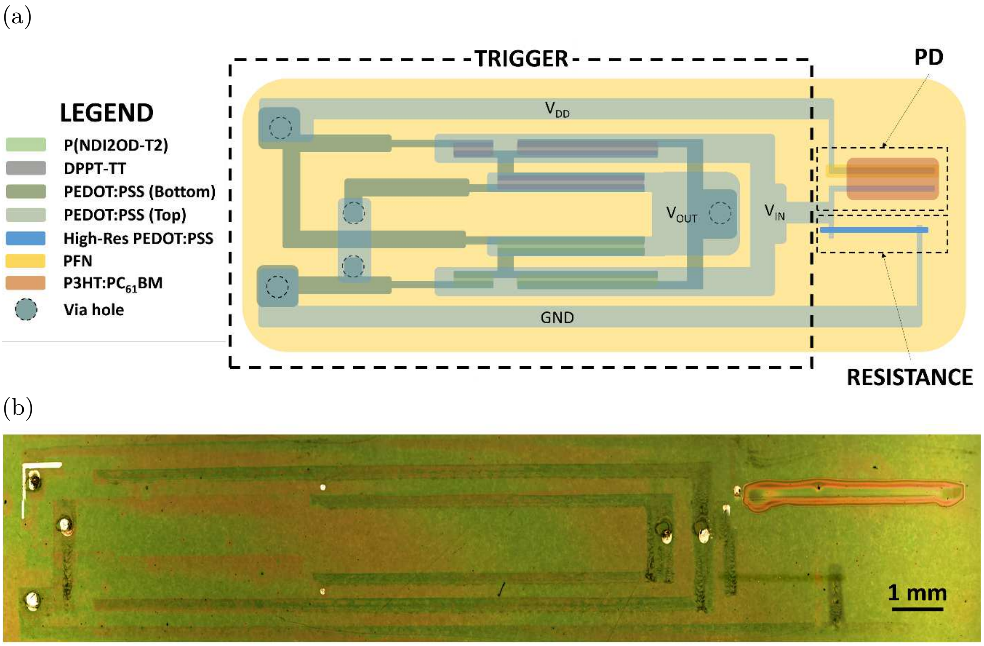

Figure 6.1: (a) Full system layout with identification of the trigger, photodetector and load resistance areas. (b) Optical micrograph of the overall system on PEN foil.

of rejecting light power fluctuations that could generate multiple unwanted ON/OFF transitions in the case of a fixed threshold. This twilight switch integrates a planar photodiode and a Schmitt trigger, electrically connected as depicted in the schematic in fig. 6.2a.

The photodetector behaves as a variable impedance device, bearing different resistances as a function of the amount of light power impinging on it. The resistive partition realized by the photodiode and the printed pull-down resistor is fed to the input terminal of the Schmitt trigger. The trigger is responsible for the definition of the desired switching thresholds and for providing an appropriate signal fluctuation immunity.

6.3.1 Schmitt trigger working principle

The Schmitt trigger is a very common and well-known electronic circuit.[194] Its basic function is to provide an inversion of the logic value at its input, in a similar manner to the simpler inverter logic gate, with the additional feature of providing a defined-by-design hysteresis between the high-to- low and low-to-high transitions. Its realization in complementary logic is shown in fig. 6.2b, and an example of an ideal voltage transfer curve is shown in fig.

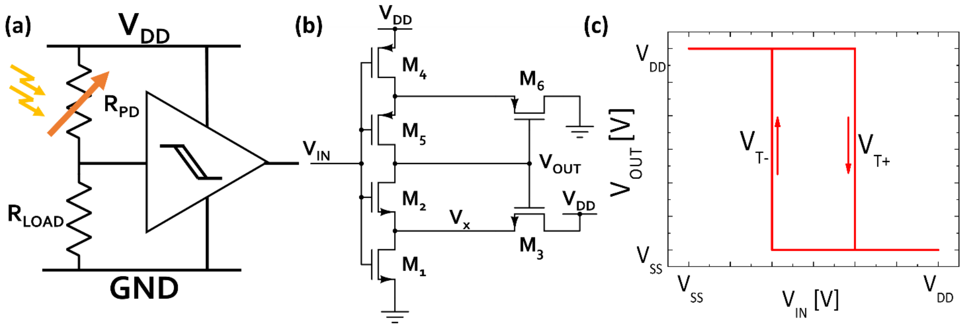

Figure 6.2: (a) Schematic of the photo-active switch proposed in this work. The photodetector acts as a variable resistor R_{PD} in a voltage divider configuration with the load resistance R_{LOAD}. (b) Complementary Schmitt trigger circuital scheme. (c) Ideal voltage transfer characteristic of a Schmitt trigger highlighting the hysteresis behaviour with the two thresholds V_{T+} and V_{T-}.

6.2c, which highlights the two transitions at the V_{T+} and V_{T-} thresholds. The width of the hysteresis and position of the threshold voltages can be tuned by suitably designing the aspect ratio of the transistors.

6.3.2 Transition thresholds determination

The analysis of the circuit mainly relies on the determination of the threshold voltages for high-to-low and low-to-high transitions. The symmetry between the p- and n-subnetworks allows the separate analysis of the two transitions; hence, only the n-type network will be treated as an example. When the input voltage V_{IN} is set to $0V$, transistors M_1 and M_2 are turned off, and the output voltage V_{OUT} is kept at the supply voltage level V_{DD} thanks to the series of transistors M_4-M_5. Hence, transistor M_6 is off and transistor M_3 is on, keeping V_X at $(V_{DD} - V_{tn})$. When V_{IN} reaches V_{tn}, M_1 turns on in the saturation region, driving a current

$$I_1 = 0.5\mu_n C_{ox}\frac{W_1}{L_1}(V_{IN} - V_{tn})^2 \tag{6.1}$$

while M_3 drives

$$I_3 = 0.5\mu_n C_{ox}\frac{W_3}{L_3}(V_{DD} - V_X - V_{tn})^2 \tag{6.2}$$

and V_X decreases linearly with the increase of V_{IN}, as long as M_2 is in the off-state. By equating I_1 and I_3 results:

$$V_X = V_{DD} - V_{tn} - \sqrt{\frac{k_1}{k_3}}(V_{IN} - V_{tn}) \tag{6.3}$$

where

$$k_i = 0.5\mu_n C_{ox}\frac{W_i}{L_i} \tag{6.4}$$

When V_X reaches $V_{IN} - V_{tn}$, M_2 turns on and starts to discharge the output node. Thus, the high-low transition would start at a value

$$V_{T+} = \frac{V_{DD} + \sqrt{\frac{k_1}{k_3}}V_{tn}}{1 + \sqrt{\frac{k_1}{k_3}}} \tag{6.5}$$

In reality the real high – low transition initiates at a value $V_{IN} > V_{T+}$, since at V_{T+}, when M_2 is turned on, a current path from V_{DD} to ground is created through M_5 – M_4 – M_2 – M_1, and a small further increase of V_{IN} is needed to lower the voltage of the output node, allowing M_6 to turn on and complete the triggering action. Similarly, the low-to-high transition threshold can be derived as follows

$$V_{T-} = \frac{\sqrt{\frac{k_4}{k_6}}(V_{DD} - V_{tp})}{1 + \sqrt{\frac{k_4}{k_6}}} \tag{6.6}$$

We have validated our approach for the determination of the switching thresholds through simulations of the circuit for different $k_1/k_3 = k_4/k_6$ ratios (fig. 6.3), and we found good accordance between the simulation and the theoretical prediction with a maximum discrepancy of $900mV$.

6.4 Results and discussion

6.4.1 Photodetector

A photodetector was realized on top of a bar-coated PMMA layer, which serves as gate dielectric in the trigger realization, in order to facilitate the subsequent integration in the final fabrication stage. Two parallel PEDOT:PSS electrodes separated by a $90\mu m$ gap were fabricated by inkjet printing. Subsequently, printing of the photoactive ink formulated by dissolving P3HT and $PC_{61}BM$ at $30mg \cdot ml^{-1}$ in a solution of dichlorobenzene and mesitylene as in chap. 2 is performed. No thermal treatment was required to obtain device performances suitable for the application here described, thus relaxing constraints on the thermal budget during the system integration.

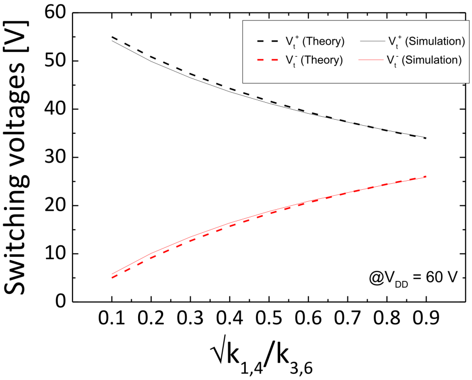

Figure 6.3: Theoretical (dashed lines) and numerically simulated (solid line) thresholds at $V_{DD} = 60V$ for Schmitt triggers designed with different aspect ratios.

The need to apply a bias higher than a few volts to properly comply with the Schmitt trigger supply voltages (sec. 6.4.3) forces the choice for a planar structure that shows a reduced electric field with respect to a vertical one because of the larger inter-electrode spacing; typically tens of micrometers for the planar, and hundreds of nm for the vertical structure. If two symmetric PEDOT:PSS electrodes are adopted, the ratio between the resistance in light and dark conditions was slightly higher than unity (fig. 6.4).

To solve this issue we resort to the functionalization of one of the electrodes that was done by printing PFN on top. The PFN hole blocking effect prevents hole injection from the functionalized electrode while their collection at the other contact is kept unchanged (sec. 5.3.1). The photodetector biased at $60V$ shows a resistance (R_{PD}) of $7.2G\Omega$ when kept in the dark, while $R_{PD} = 91.7M\Omega$ when exposed to $10.9mW \cdot cm^{-2}$ $6400K$ white radiation. The R_{PD} versus impinging power curve is reported in fig. 6.5c, for a photodetector biased at 60, 30 and $1V$.

We stress the fact that a wide modulation is present also for the low bias ($1V$). We measured the external quantum efficiency (EQE) spectrum of the detector (fig. 6.5d), recording a response well superimposed with the P3HT:PC$_{61}$BM absorption spectrum. The response time was determined at various light intensities: as a photoconductor, the device shows typical photoconductive features with fast response times at high light intensity and slow at low ones (fig. 6.6b). The decay time is equal to $150\mu s$ at $1mW \cdot cm^{-2}$ while at $100nW \cdot cm^{-2}$ is around $100ms$. Above $100\mu W \cdot cm^{-2}$ the photoresistance follows a photoconduction model which takes into account hopping charge transport in an exponential density of states (fig. 6.6).[153] We also found good reproducibility of the photodetector parameters between different

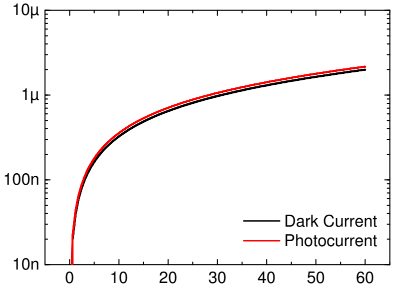

Figure 6.4: Photodetector current in the case of symmetrical electrodes in dark (black) and exposed to $3mW \cdot cm^{-2}$ white light (red) as function of the applied voltage. Ratio between photocurrent and dark current computed at bias of $60V$ is 1.085.

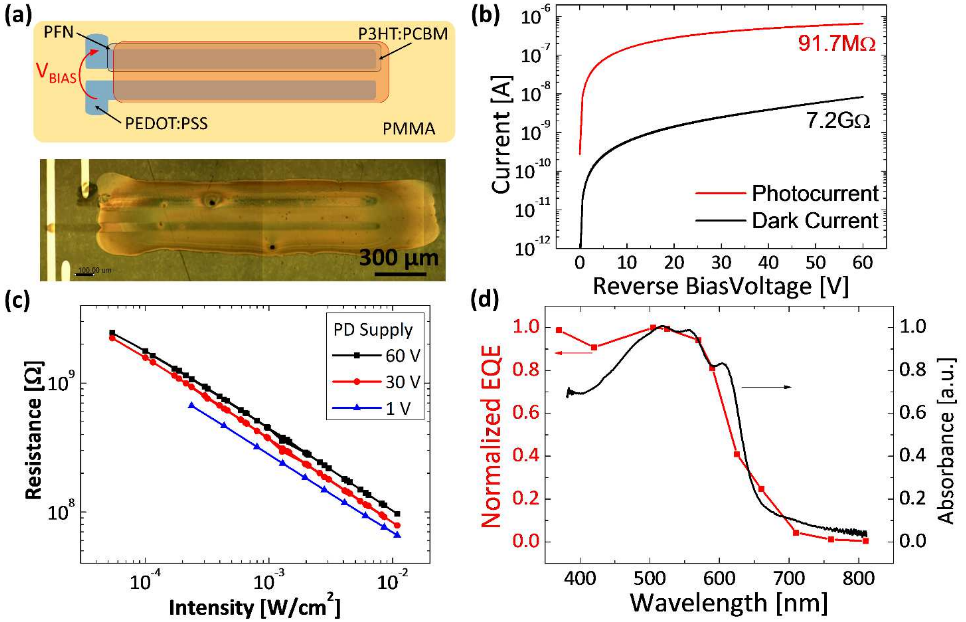

Figure 6.5: (a) Layout and optical micrograph of the printed planar photodetector. (b) I-V characteristics in dark (black) and lighted (red) conditions with resistance computed at bias of $60V$. (c) Resistance versus impinging optical intensity at $60V$ (black), $30V$ (red) and $1V$ (blue) of applied bias. (d) External quantum efficiency and absorption spectra of the printed planar photodetector.

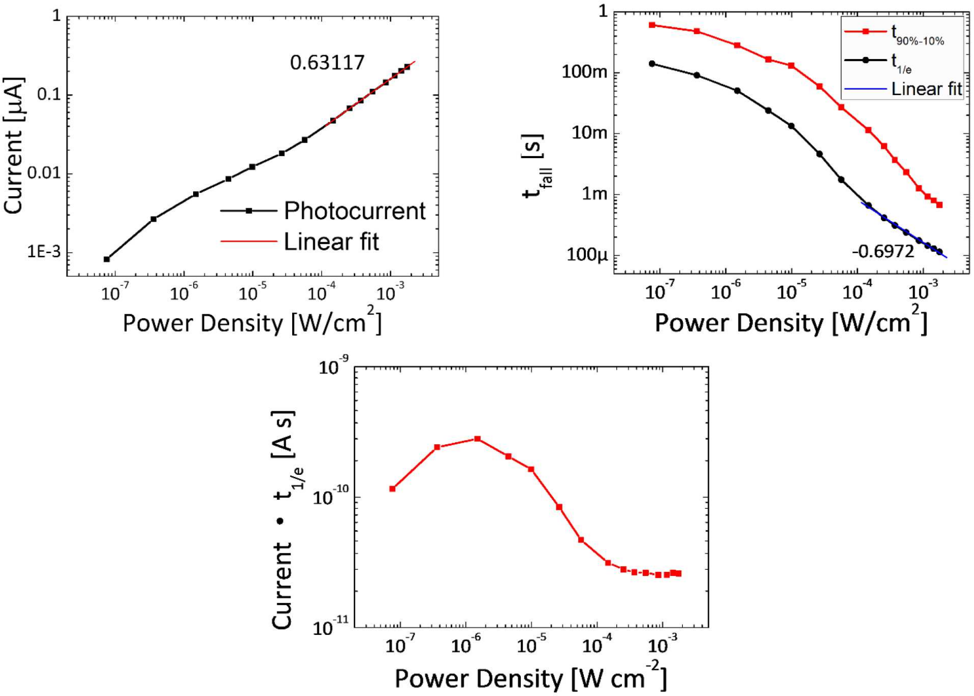

Figure 6.6: Photodetector photocurrent (a), response time (b) and product between photocurrent and response time (c) plotted versus optical power density. Above $100 \mu W cm^{-2}$ the photoresistor shows fingerprints of hopping photoconduction in exponential density of states: the photocurrent follows a power law on light intensity with exponent less than unity, decay time decreases as power law on light intensity and the product between the two is independent on impinging intensity.

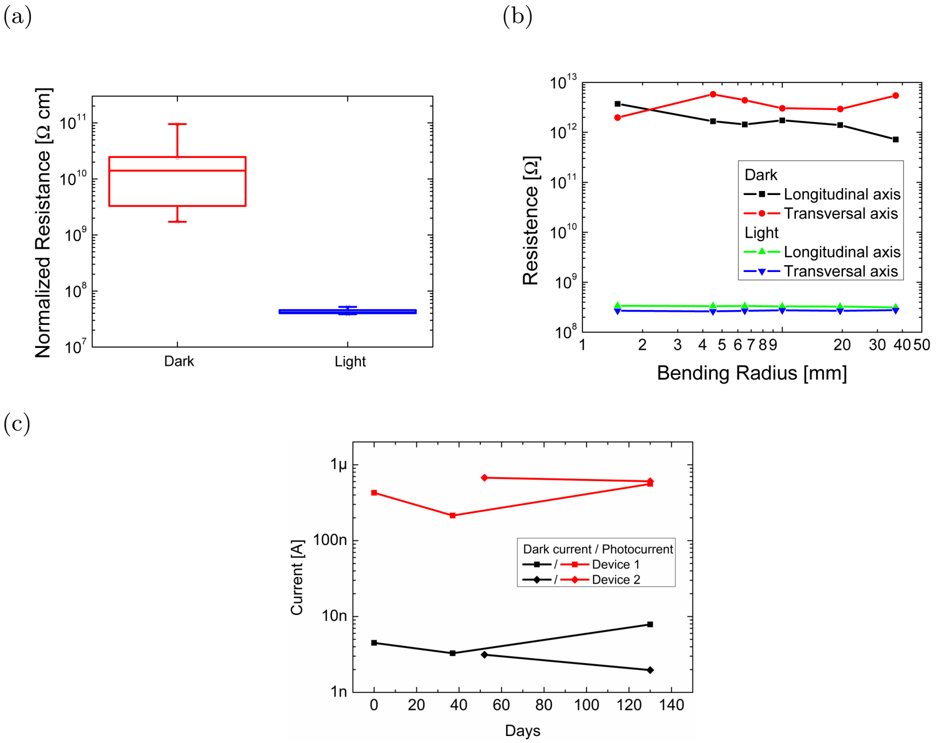

Figure 6.7: (a) Normalized resistance variation for a number of photodetectors and (b) resistance variation for a single photodetector after bending at different bending radii. (c) Stability measurements for photodetectors in a 130 days period.

realizations in light and dark regimes of operation (fig.6.7a).

Moreover, the photodetector resistance variation under tensile stress was measured, showing minimal change down to a bending radius of less than $2mm$, both in light and dark conditions (fig.6.7b). This result is perfectly compliant with the bending properties of the transistor devices, as described in[67]. Stability measurements on the photodetector (fig.6.7c) show limited parameter variations in a period of 130 days during storage in a nitrogen glove box.

6.4.2 Transistor characterization

We employed p- and n-type organic field effect transistors (OFETs) in a top-gate, bottom-contacts architecture (fig. 6.8a,d).

On a $125\mu m$ thick PEN substrate, we patterned PEDOT:PSS by inkjet printing to de fine the source and drain electrodes, resulting in an OFET with channel length $L = 50\mu m$, which is kept constant for all devices, and with the

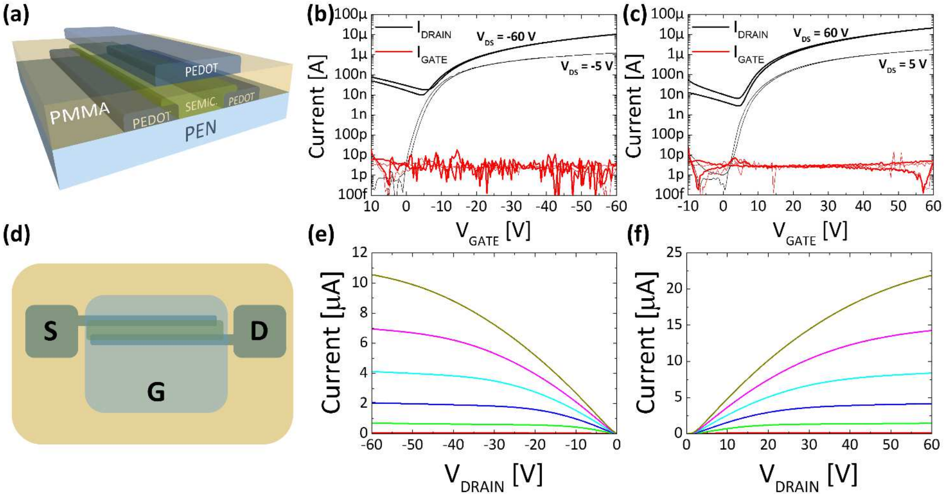

Figure 6.8: (a) 3D View of a general OFET stack employed in this fabrication and (d) top view of the device. (b) Transfer and (e) output characteristics for a p-type OFET, (c) transfer and (f) output characteristics for an n-type OFET ($W = 1000\mu m$, $L = 50\mu m$).

variable channel width W, depending on circuit design requirements. Then p- and n-type semiconductors are deposited from solution by inkjet printing in the channel region, resulting in a $\sim 40nm$ thick layer. The $700\mu m$ thick dielectric layer is then deposited via bar-coating following the same procedure as in[67]. The output and transfer curves of two typical n- and p-type devices realized through this process are shown in fig. 6.8b,c,e,f, and the extracted charge carrier mobilities and threshold voltages are summarized in tab. 6.1. The devices fabricated through this process feature a gate leakage current level lying below $10pA$ guaranteeing an appropriate decoupling between the input and output stages of the logic gates when they are employed in complementary circuits. In general, an organic transistor can be operated both in the hole and electron accumulation regimes, a feature referred to as am-

Type	Semiconductor	μ_n $[cm^2/Vs]$	μ_p $[cm^2/Vs]$	V_{tn} $[V]$	V_{tp} $[V]$
N	P(NDI2OD-T2)	0.18	$2 \cdot 10^{-3}$	4.8	-20
P	DPPT-TT	$2 \cdot 10^{-3}$	0.08	20	-4

Table 6.1: Summary of the average of extracted saturation mobilities and threshold voltages for the fabricated OFETs

bipolarity.[195] Despite this, in the case of strongly different charge mobilities associated to the two carriers, we refer to the highest one to define whether the transistor is employed as p- or n-type. We identify the highest one as the nominal mobility, while the lowest one is denominated as the parasitic channel mobility. The saturation mobilities and threshold voltages associated to the parasitic charge carriers for our n- and p-type transistors are summarized in tab. 6.1. The Schmitt trigger complementary layout is designed to operate properly in the case of ideally unipolar transistors, yet in our case a degree of ambipolarity is present and this has an effect which is discussed in the next section. In our previous work[67] OTFTs fabricated with the same process along with transparency these devices showed great flexibility, despite the use of a rather thick PET substrate, as assessed by bending tests. By applying a tensile stress $> 1\%$ perpendicular to the FET array channel a minimal variation of the electron mobility was found, denoting the robustness of this fabrication approach. In order to assess the advantages and disadvantages of our method over other fully-printed approaches for the fabrication of complementary circuits, we have compared the performance of our fully-printed all-organic devices with some works implementing fully-printed or partially printed complementary logic circuits (tab. 6.2).

We highlight how this robust fabrication process allows the realization of p- and n-type transistors with almost balanced mobilities and good threshold voltage values. Moreover, it is noteworthy that our approach, among all the compared works, combines excellent performance in terms of charge carrier mobility and an all-organic all-polymer fabrication process at the same time.

6.4.3 Schmitt trigger

The Schmitt trigger was fabricated by connecting six transistors realized following the layout illustrated in fig. 6.1a. We realized three different designs with values of 0.09, 0.25 and 0.81 for $k_1/k_3 = k_4/k_6$. These values should guarantee, in an ideal trigger, high-low switching thresholds of 47.3, 41.7, and $33.9V$ respectively and in low-high switching thresholds of 12.7, 18.3, and $26.1V$ respectively. The measured voltage transfer characteristics (VTCs) illustrate the correct behaviour of the circuit at different V_{DD} (fig. 6.9a $k_1/k_3 = k_4/k_6 = 0.25$), a quasi rail-to-rail operation and a hysteresis window correctly centred around $V_{DD}/2$.

A collective view of the VTCs of the three different designs ($V_{DD} = 60V$) is presented in fig. 6.9b, highlighting good agreement of the transition threshold with the predicted values for an aspect ratio of 0.81, agreement that gradually worsens while moving towards lower aspect ratios. To address this deviation from the ideal prediction, we introduced in the simulations the contribution

Ref.	Fabrication process	Semiconductor	Type	Mobility $[cm^2/Vs]$	Threshold $[V]$	Supply voltage $[V]$
[188]	Inkjet / Screen Printing / Evaporation	Acene-based-diimide	n	$3.7 \cdot 10^{-2}$	15	40
		PTAA	p	$3.4 \cdot 10^{-2}$	-8.9	
[189]	Screen printing / Gravure	BASF GSID 104031-1	n	$2.9 \cdot 10^{-3}$	-1 ± 7.1	100
		TIPS-Pentacene	p	$3.9 \cdot 10^{-3}$	-1.5 ± 7.1	
[190]	Inkjet / Dropcast / Evaporation	N1400	n	$3.7 \cdot 10^{-3}$	N.A.	80
		TIPS-Pentacene	p	$7.8 \cdot 10^{-3}$	N.A.	
[191]	Evaporation / Bar-coating	CsF / PTVPhI-Eh	n	0.23	45.6	100
		PTVPhI-Eh	p	0.24	-32.3	
This work	Inkjet / Bar-coating	P (NDI2OD-T2)	n	0.18	4.8 ± 0.5	60
		DPPT-TT	p	0.08	-4 ± 0.3	

Table 6.2: Parameters and process comparison between fully-printed / partially printed complementary logic works.

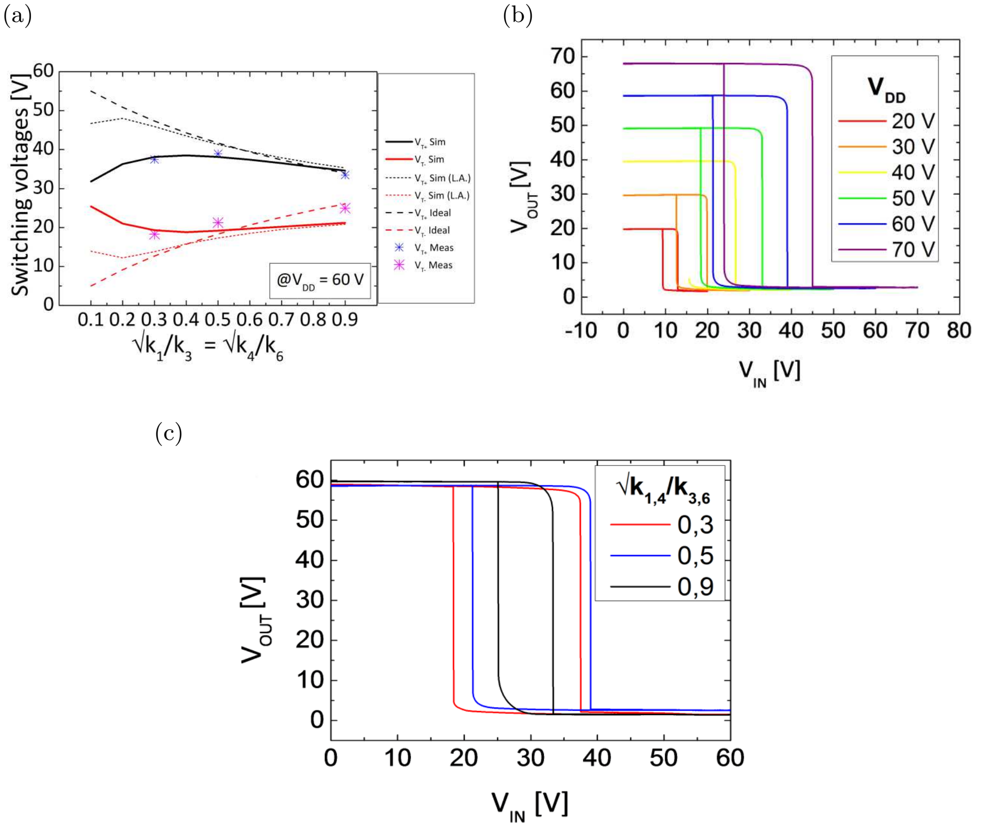

Figure 6.9: (a) Voltage transfer curves for a Schmitt trigger with $k_{1,4}/k_{3,6} = 0.25$ at different supply voltages and (b) voltage transfer curves at $V_{DD} = 60V$ for triggers with different aspect ratios. (c) Ideal, simulated and measured trigger switching voltages for different transistor aspect ratios and under multiple ambipolarity conditions.

Aspect ratio $k_{1,4}/k_{3,6}$	Simulated V_{T+} $[V]$	Measured V_{T+} $[V]$	Deviation $[\%V_{DD}]$	Simulated V_{T-} $[V]$	Measured V_{T-} $[V]$	Deviation $[\%V_{DD}]$
0.09	38.1	37.5	1.0	19.3	18.3	1.6
0.25	38.1	38.9	1.3	19.2	21.2	3.3
0.81	34.6	33.5	1.8	21.2	25	6.3

Table 6.3: Simulated and measured Schmitt trigger thresholds for different transistor aspect ratios.

of the parasitic channel due to the ambipolar nature of the semiconductors employed.[187,191] Indeed, we verified that ambipolarity leads the circuit to deviate from the ideal behaviour as predicted by the formulas derived previously. We have simulated the circuit behaviour for different values of the nominal and parasitic charge carrier mobility (respectively μ_n and μ_s), and we show the results in fig. 6.9c. The results of the simulation associated with the values summarized in tab. 6.1 (thick solid line, fig. 6.9c) are displayed in tab. 6.3, along with the measured threshold voltages and the deviation from the simulated values. The simulation results fit well with the experimental data in the case of the high-low threshold, while the deviation is more distinct when considering the low-high thresholds. We attribute this discrepancy to a drift of the threshold voltage V_T of the p-type transistors due to bias stress occurring during the measurement time. Therefore, even in the absence of a strong ambipolarity, as in our case, the circuit suffers a remarkable deviation from the ideal theoretical behaviour, reducing the available maximum width of the hysteresis window. To limit this source of non-ideality, a reduction of the contribution of the parasitic channel is needed. We performed a second simulation (thin dashed line, fig. 6.9c) in which we set $\mu_n/\mu_s = 10^3$, and we show that this further reduction of the ambipolar contribution would allow an approach to the ideal behaviour and of exploiting a hysteresis window width of up to 60% of the supply voltage.

6.4.4 Environmental working simulation

Taking into consideration the device operation, we have simulated the system response to a real working environment on the basis of the experimental data collected for the discrete trigger and photoresistor components. To this purpose, we calculated the solar direct radiation power on a surface at a particular tilt angle as a function of latitude and day of the year.[196] The resulting direct radiation versus daytime plot, calculated at $44°N$ latitude (Milan, Italy) and for the 172^{th} day of the year, is shown in fig. 6.10a. In order to extract

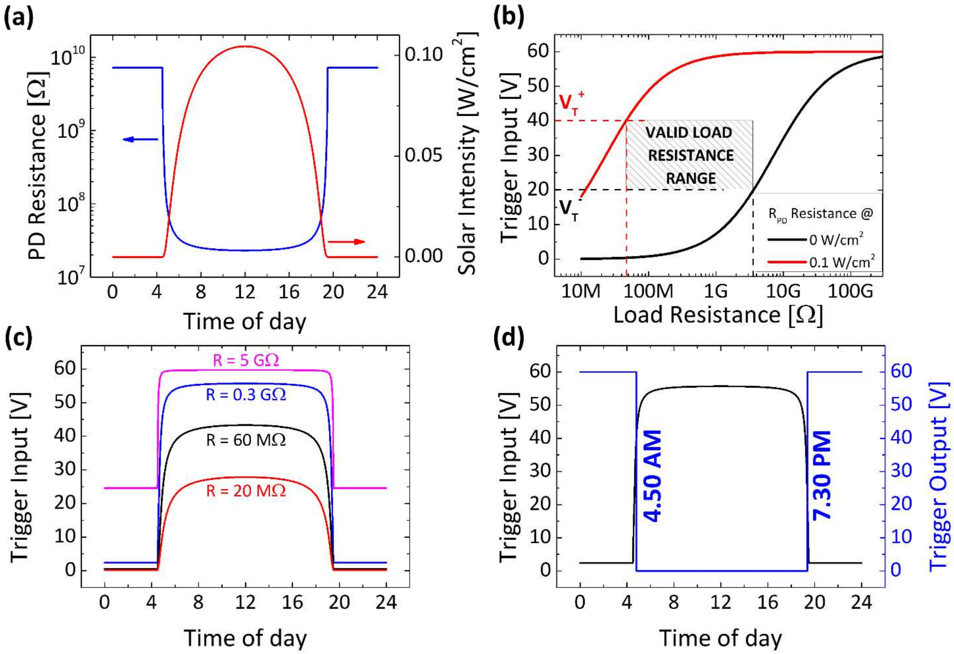

Figure 6.10: (a) Photodetector equivalent resistance in response to direct solar exposure during the day. (b) Load resistance range selection for a trigger designed with $V_{T+} = 40V$ and $V_{T-} = 20V$. (c) Trigger input from the $R_{PD} - R_{LOAD}$ voltage divider at different values of the load resistance. (d) Simulated system output for a load resistance of $300M\Omega$.

the resistance as a function of the daytime, we fitted and then numerically reconstructed the resistance-power curve of the photodetector at $60V$. By comparing the direct exposure to sun power with the aforementioned data it is then possible to plot the photodetector equivalent resistance during the whole day. This information is useful to make a direct estimation of the input signal fed to the Schmitt trigger as a result of the voltage divider between the variable photodetector resistance R_{PD} and the PEDOT:PSS printed load resistance R_{LOAD}. To properly address the signal that is fed to the trigger input, both the photodetector resistance R_{PD} and the load resistance R_{LOAD} must be taken into consideration. Since R_{PD} in light and dark is fixed by the PD fabrication process and layout, a proper load resistance must be chosen. In fact, the need to satisfy the requirements for the input signal to be greater than the V_{T+} threshold, when the PD is exposed to a certain solar intensity, and lower than the V_{T-} threshold, in almost-dark conditions, is consequently imposing a range upon which the load resistance must be chosen. In fig. 6.10b this range is highlighted, for a Schmitt trigger with threshold $V_{T+} = 40V$ and $V_{T-} = 20V$, by evaluating the input signal fed to the trigger for different R_{LOAD} values. As R_{PD} values we used the previously reported experimental data in which $R_{PD} = 7.2G\Omega$ in dark conditions and $R_{PD} = 91.7M\Omega$ at an incident power of $0.01W \cdot cm^{-2}$; the R_{PD}-incident power curve fitting allows the estimation of R_{PD} for any illumination value, hence extracting a $R_{PD} = 23.2M\Omega$ at an incident power of $0.1W \cdot cm^{-2}$. Under these conditions, the allowed load resistance values range from $46M\Omega$ to $3.6G\Omega$ as highlighted in fig. 6.10b. It is important to point out that the gate leakage current coming from the Schmitt trigger may affect this choice by modifying the voltage at the input node following the relation:

$$V_{IN} = \frac{R_{LOAD}}{R_{LOAD} + R_{PD}} V_{DD} + I_{Leak} \frac{R_{LOAD} \cdot R_{PD}}{R_{LOAD} + R_{PD}} \tag{6.7}$$

thus potentially compromising the previous R_{LOAD} estimation. Simulations (fig. 6.11) show that for the range of resistances employed in our application, leakage levels must be lower than $1nA$ to have a negligible effect. Therefore our system does not suffer this drawback since common gate leakage levels are in the $1 - 10pA$ range, as reported in fig. 6.8. As the R_{LOAD} range and the R_{PD} values are defined, it is then possible to evaluate the trigger input signal as a function of the daytime. Fig. 6.10c shows the signal trend for different R_{LOAD} values chosen inside ($60M\Omega$, $300M\Omega$) and outside ($20M\Omega$, $5G\Omega$) the allowed range. Whereas the former provide perfect switching beyond the thresholds, the latter give rise to a non-switching behaviour of the trigger. The correct behaviour of the input signal is also underlined in fig. 6.10d where

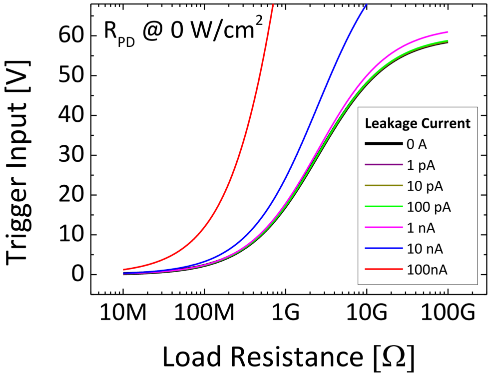

Figure 6.11: Influence of the leakage current on the choice of R_{LOAD} considering a gate leakage coming out of the trigger gate and the photodetector in dark conditions.

we have simulated an ideal output of the entire system as a function of the daytime. As the Sun is rising, thus the solar incident power increases, the input signal triggers the device to a low output at approximately $4.50AM$. Similarly, the device is triggered to a high output level when the incident power is decreasing, at approximately $7.30PM$. This also demonstrates that the resistance R_{LOAD} can be used, in addition to the hysteresis windows, to fine-tune the time at which the switching occurs. The relation between the target switching power and the system parameters can be used to properly design the system and is derived as follows:

$$V_{T+}(P_{T+}) = V_{DD}\left(1+\frac{10^{a+b\log_{10}P_{T+}}}{R_{Load}}\right)^{-1} = \frac{V_{DD}+\sqrt{\frac{k_1}{k_3}}V_{tn}}{1+\sqrt{\frac{k_1}{k_3}}} \tag{6.8}$$

where a and b are parameters extracted by fitting the resistance-power relation of the photodetector and P_{T+} is the target switch-off power. The same applies to the negative threshold.

6.4.5 Full-system measurements

The base building blocks presented have been integrated following the layout depicted in fig. 6.1 and the output voltage was measured upon variation of the impinging light intensity from dark to a maximum of $10.9mW \cdot cm^{-2}$. In fig. 6.12a we plot the variation of the Schmitt trigger input voltage versus light intensity (linear scale for the intensity in the inset), highlighting the proper operating behaviour of the light-sensing stage. Finally, in fig. 6.12b, we show the correct switching activity of the output voltage upon the variation

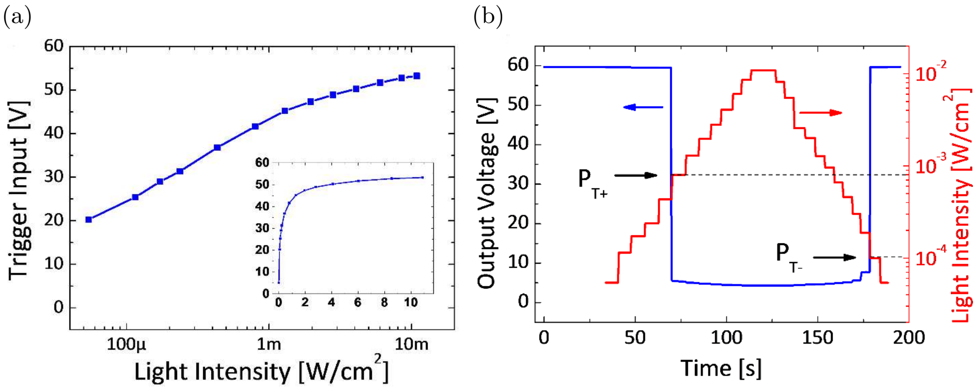

Figure 6.12: (a) Measurement of the trigger input voltage versus impinging light intensity (linear scale on abscissa in the inset). (b) Variation of the output voltage of the circuit (blue) upon change of the impinging light intensity (red). P_{T+} and P_{T-} threshold voltages are marked.

of the impinging light intensity. The fluctuation immunity feature, previously introduced, is demonstrated by high-lighting the different switching thresholds (dashed thin black line, fig. 6.12b) for the high-low and low-high transitions.

6.5 Conclusions

We have demonstrated an effective method for integrating different transparent and fully carbon-based devices into a single real-life application. In addition, the fabrication was entirely realized by employing scalable printing techniques at low temperatures and in ambient conditions. The implemented fabrication process, combining the good resolution typical of inkjet printing techniques together with the advantages of fast prototyping and reduced waste of material, proved itself capable of fabricating devices with optimal performance and improved repeatability, desirable features for the realization of circuits or integrated systems in an industrial environment. In particular, we realized a twilight switch integrating a printed organic photodetector and a printed organic Schmitt trigger. First, the Schmitt trigger design requirements for the tuning of its switching thresholds have been discussed and experimentally validated, including the non-idealities introduced by the OFETs ambipolar contribution. This analysis was then used and combined with simulations to properly design a sensor capable of reacting to the daily typical sunlight intensity variation and trigger an ON/OFF signal at selected times of the day. The designed system was fabricated entirely using scalable printing techniques and the correct integration and working behaviour of the overall system was experimentally validated. Compared to other recent works in which organic complementary circuits were realized employing scalable techniques, at least partially, our fabrication method not only enables a fully-printed approach, but also attains a performance among the best in terms of charge carrier mobility and threshold voltage standard deviation. This work proves the feasibility of our technique for the fabrication of real-life applications combining desirable elements (such as bendability and transparency) for the realization of electronics for wearable devices, distributed sensing, bio-electronics or flexible displays, solely employing techniques which are scalable to low-cost mass production.

Conclusions

My Ph.D. thesis reports on the development of inkjet printed organic photodetectors and their integration in complex optoelectronic systems.

We have demonstrated the possibility to fabricate photodetectors with good optoelectronic performances via cost-effective and additive inkjet printing technique. Additional key features as semi-transparency and fully-patternability of the devices offer advantages for their integration in complex electronic systems. With a specific detectivity that reaches $6.2 \cdot 10^{12}$Jones in the best case, the inkjet printed photodetectors realized in this work are not only among the best of printed photodiodes reported in literature so far but also compete with their inorganic counterpart. This work demonstrates the possibility to fabricate an imager prototype of interconnected semitransparent organic pixels realized by inkjet printing and femtosecond laser ablation. The versatility of the fabrication approach used was a great advantage for the improvement of performances and to achieve the goal. The overall thermal budget is limited and the material waste low. No vacuum technique or mask was used. The flexibility and lightweight of the substrate are other key features. Fabrication yield and characteristics of single components were enough to operate the matrix and to acquire signals from 6 pixels detecting two order of magnitudes of impinging light intensity.

The use of a suitably synthesised interlayer material, namely poly-PT, was addressed. Guidelines for the design of poly-PT aim to an effective electron blocking layer which can also serve to improve the wettability of photoactive blend by PEDOT:PSS ink. Poly-PT design took in consideration its solubility too. Not only it turns out to be solution processable but can also be deposited with inkjet printing without damaging the organic semiconductor. Fully-organic, inkjet printed photodetectors realized exploiting this new interlayer succeed both in avoiding the massive addition of fluorosurfactant to PEDOT:PSS and halving dark current densities with respect to reference device. Printed semitransparent photodetectors with reduced dark current can pave the way for a cost-effective integration of this sensing elements in interactive surfaces and imaging systems with challenging SNR requirements. Photoconductive behaviour was deeply investigated highlighting changes introduced by the EBL. Specifically, increased amount of interface traps is pointed out as a reasonable cause for the slowing down of the response and as an extra contribution to the electron blocking effect.

The adoption of low band gap small molecule based inks to fabricate all-organic, semi-transparent photodiodes printed on plastic substrates was reported. Proper formulation of organic ternary blends led to reproducibly device realization. The wavelength response of P3HT:PCBM detector was extended to red and NIR ranges, obtaining a devices sensible from 470 to $750nm$. EQE in excess of 10% was achieved up to $710nm$ both when light impinges from the top and the bottom side.

The investigation of PFN role found that a PFN thin layer is effective in $0.5eV$ reduction of the workfunction of PEDOT:PSS and gold electrodes. I-V measurements performed on a number of different devices structures was used to prove PFN hole blocking effect.

At last it was presented the realization of a twilight switch integrating a printed organic planar photodetector and a printed organic Schmitt trigger. Planar structure was chosen because it makes possible to apply to the photoresistor voltages of tens of Volts without incurring in breakdown. The Schmitt trigger design requirements for the tuning of its switching thresholds have been discussed and experimentally validated, including the non-idealities introduced by the OFETs ambipolar contribution. This analysis was then used and combined with simulations to properly design a sensor capable of reacting to the daily typical sunlight intensity variation and trigger an ON/OFF signal at selected times of the day. The designed system was fabricated entirely using scalable printing techniques and the correct integration and working behaviour of the overall system was experimentally validated reproducing the exposure to sun that occurs during a day.

Appendix A

Introduction to organic semiconductors

In this appendix electronic properties of organic semiconductors will be used to introduce concepts related to charge transport in molecular solids, their interaction with light and injection of charges from metal to organic semiconductors.

A.1 Fundamental properties of organic semiconductors

Organic semiconductors are carbon-based compounds undergoing the sp^2 or sp hybridization of the atomic orbitals.[197,198] The hybridization is the result of the linear combination of $2s$ and $2p$ orbitals, resulting in a strong and localized covalent bond between the adjacent atomic sites (σ-bond) which constitutes the back-bone of the carbon based molecule/polymer. When one or two p orbitals are not involved in the hybridization, but still available they combine with each other to form weak π-bonds (fig. A.1). This kind of bond admits the existence of an electronic cloud delocalized over the molecular plane and gives semiconducting properties to molecular solids.[198] Organic compounds are built up by the repetition of the same fundamental unit, named monomer, for one (molecule), few (oligomers) or many times (polymer). Molecules/polymers are packed together to form molecular solids via Van der Waals interactions. Those interactions ($10kcal/mol$)[199] are weaker than covalent bonds (e.g. crystalline solids), but strong enough to build solid state films. Mechanically flexibility and processability from solution at room temperature are allowed by the weakness of the Van der Waals interaction.

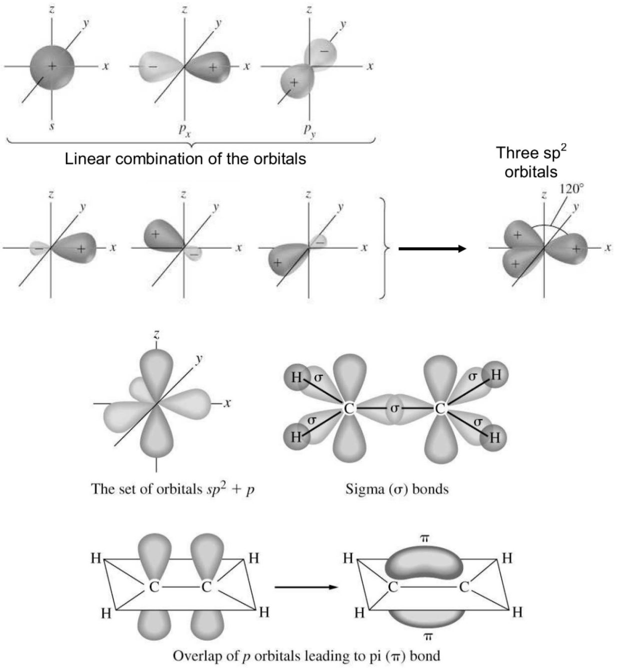

Linear combination of the orbitals

The set of orbitals $sp^2 + p$

Sigma (σ) bonds

Overlap of *p* orbitals leading to pi (π) bond

Figure A.1: Formation of the hybridized orbital *sp*2 (top); σ and π orbitals in the ethylene molecule (bottom).

A.2 Electronic properties of organic semiconductors

A.2.1 Peierls instability in organic systems

The model of the monodimensional semiconductor adopted in solid state physics can be exploited to describe the electronic properties of molecular solids. Considering a chain with an infinite number of monomeric units without chemical defects, the model of 1-D semiconductor can be used to describe the electronic properties of the system. Let's consider the case of polyacetilene: putting several monomeric units close together to form a chain, we expect a strong σ-orbital located around the atomic sites and a delocalized π-orbital placed above and underneath the plane of the carbon sites. In the hypothesis that atom sites are equally spaced by the same amount d each atom shares one half-filled p orbital. For a chain composed by n carbon sites, the system presents a half-filled band made of n energy levels, according to the Bloch theorem. Consequently polyacetilene should behave like a metal, but this is not true. Peierls theorem states that one-dimensional equally-spaced ions chain with one electron per ion is unstable.[200] In fact, if the periodicity of the chain is modified, i.e. doubled, displacing the even parity atoms of δ in order to modulate the distance between adjacent carbon atoms, a gap appears in the dispersion diagram at $k = \pm\pi/2a$ (being a the distance between two adjacent carbon atoms). The energy states lying between $-\pi/2a$ and $+\pi/2a$ undergo an energy reduction, while the energy of the other states is increased. Since half a band was empty, the final result is a energy decrease for occupied states and an energy increase for empty states, leading to the band structure of a semiconductor material. In the case of polyacetilene the ground or the fundamental state comes from a distortion where $r = 2$, giving rise to a second order degeneracy: the half-filled 'initial' band is split in two bands where the occupied states lie energetically below the empty states. A gap appears in the dispersion plot at $k = \pm\frac{\pi}{2d}$ and the semiconducting behaviour of polyacetilene can be easily justified (fig. A.2).

In the organic systems Peierls instability is named dimerization or conjugation. In cases where adjacent carbon sites are not equivalent and the $2a$ periodicity already exists before taking into account the effect of the dimerization the so called extrinsic contribution to the gap has to be added to the dimerization one. In the case of chains with finite length the Jahn-Teller theorem holds: conjugated oligomers show a dimerization of the molecule which leads to an energy stabilization of the HOMO orbital (Highest Occupied Molecular Orbital) and a destabilization of the LUMO orbital (Lowest Unoccupied Molecular Orbital) which results in an energetic gap between them.

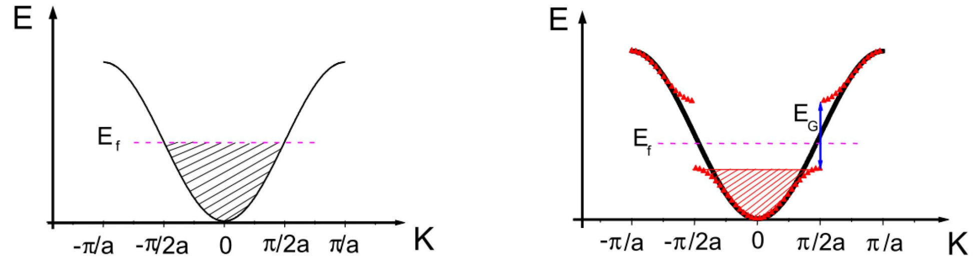

Figure A.2: Comparison between the $E - k$ plot of undimerized (left) and dimerized systems (right).

A.2.2 Excited states

Excited states in organic semiconductors can be ionic, when one or more charges are introduced in the system, or neutral.

Ionic states The ground state in conjugated systems strictly depends on the occupation of the π-orbitals in the half-filled band. The dimerization occurs to minimize the overall energy: the occupied states result stabilized while the unoccupied unstabilized. The dimerization causes an expense of the elastic energy. If an additional charge is introduced the system, it places on the first available level destabilized by the dimerization. Its energy is higher than in absence of the dimerization which turns out to be energetically disadvantageous. The system will tend to locally recover its undimerized state to arrange the additional charge. This perturbation can be seen as a state in between the LUMO and the HOMO and is usually named polaron.[198,201] If an external field is applied, the polaron can travel across the system, followed by the induced lattice distortion.

Neutral states Neutral states usually arise from interaction of light with the system. When a photon is absorbed in the semiconductor, an electron-hole pair is generated. The photogenerated charges are bound together through the Coulombic interaction in an exited state named exciton. The exciton radius and its binding energy strongly depend on the dielectric constant of the semiconductor. According to the Bohr model for the hydrogen atom[202] the semiconductor dielectric constant accounts for screening the coulombic interaction. In classical crystalline semiconductors, like silicon ($\varepsilon = 11.9$), the screening is so effective that the exciton binding energy is easily overcome by thermal energy and the charges are free to travel in the semiconductor (Wannier-Mott exciton). Organic semiconductors usually have low dielectric constant. Consequently the exciton binding energy usually ranges from 0.1 to $1eV$ (Frenkel excitons[201]) making it difficult to dissociate the tightly bound electron-hole pair at room temperature.

A.3 Transport in organic semiconductors

The motion of charge carriers in molecular solids has two mechanisms: the intramolecular transport, when the polaron is smaller than molecule, and the intermolecular transport, when the charge hops from one molecule to another. Generally speaking the intermolecular transport is the bottleneck in the charge transport, due to the weak solid state interactions between molecules and the high degree of disorder of organic systems.[203] From a general point of view a carrier can be subject to coherent transport, analogous to band-like transport for delocalized states, or hopping transport, if it moves with thermally activated jumps between localized states. The carriers motion in an ideal crystal at $0K$ is totally coherent, but progressively increasing the temperature electron-phonon interaction tends to produce a localization of the carrier. The ratio between the resonance integral (related to energetic gain for charge delocalization) and polaron binding (related to energetic gain for charge localization), determines the degree of this localization.[204] Taking into account a material the transport can be band-like below a certain temperature and hoppig-like for higher ones.[205] For solids with high disorder degree, the hopping-like model must be always used because carriers are localized even at $0K$.

Organic semiconductors can be seen as a collection of hopping site where the disorder causes a random distribution of energy values around HOMO and LUMO. In amorphous organic semiconductors the statistic distribution is typically assumed to be Gaussian, as shown in fig.A.3.[203]

A.3.1 The hopping transport

A description of hopping transport will be provided here. Let's consider the charge hopping between two sites, A and B. It is a two steps process: to reach resonant condition the two states exchange energy with phonons, then charge tunneling from the departure to the arrival site can occur (fig. A.4). Thus the hopping probability depends on two terms: the first takes into account the thermal activation, hence depending on the energy difference between A and B, the second accounting for the tunneling effect. This latter depends on the wavefunction overlapping of the sites, that takes into account their spatial displacement. A quantitative definition of the hopping rate was provided by

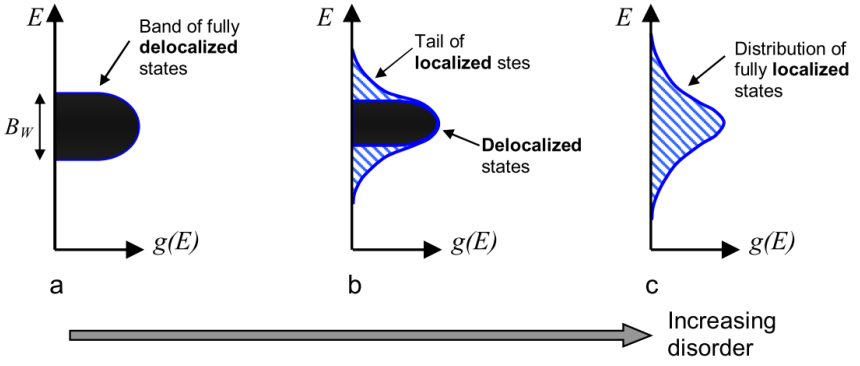

Figure A.3: Density of states depending on the system disorder arising from completely delocalized states (zero disorder; left) to completely localized ones (right).

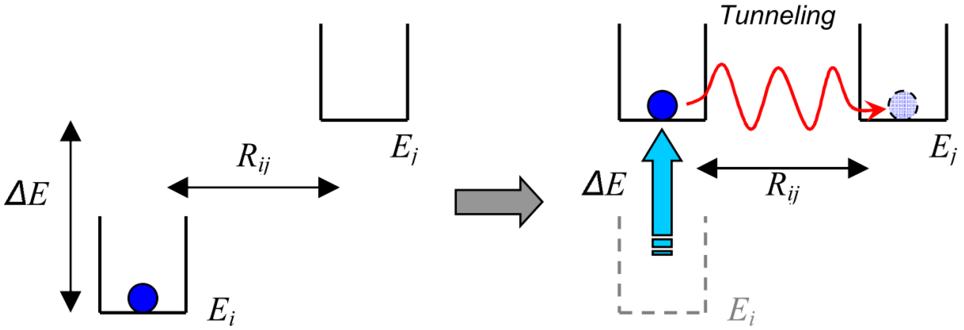

Figure A.4: Hopping process from the state i to the state j through phonon interaction.

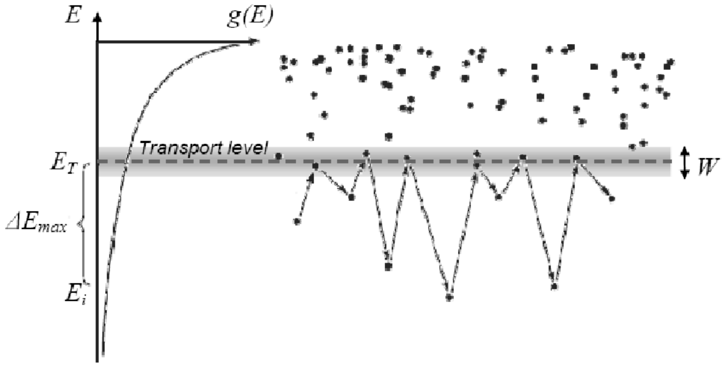

Figure A.5: In the presence of a Gaussian distribution of sites, the states on the tail are easily excited to a defined energy known as transport energy aside from their initial energy.

Miller and Abrahams for disordered semiconductors[206]:

$$\begin{cases} \nu_{i,j} = \nu_0 \cdot e^{\frac{\Delta E_{i,j}}{kT}} \cdot e^{-\gamma r_{i,j}}, E_j > E_i \\ \nu_{i,j} = \nu_0 \cdot e^{-\gamma r_{i,j}}, E_j < E_i \end{cases} \tag{A.1}$$

where ν_0 is the maximum hopping rate, ΔE is the energy difference between the two sites with energies E_i and E_j, k is the Boltzmann constant, T the absolute temperature, γ is the inverse localization radius and $r_{i,j}$ is the spatial distance between the two sites. A Boltzmann-like statistics was assumed for phonons ($\frac{\Delta E_{i,j}}{kT}$). In eq. A.1 only upward hops are considered because no thermal contribution is required for downward transitions, only the tunnelling term survives in a first approximation. At high temperature $\frac{\Delta E_{i,j}}{kT} \to 1$, the only the term $e^{-\gamma r_{i,j}}$ determines the hopping rate, hence hop toward the closest sites is favoured. For low temperature the situation is the opposite: most likely hop occurs toward the sites that need less activation energy. Generally the system finds an optimum radius as well as an optimum energy that maximizes the hopping rate. This is known as Variably Hopping Regime (VHR). It has been demonstrated for distributions decaying faster than E^{-4} that the optimal arrival site does not depend on the starting site.[207] This is also valid for carriers in gaussian tail which is usually the case for organic semiconductors.[208] The energy of this optimal site is defined as the transport level (fig. A.5). After being excited to the transport level, the carrier will probably hop toward low energy sites. where it waits until it is excited again to the transport level. It is possible to qualitatively assess the carrier mobility by using the concept of transport level. The mobility is limited by the most difficult hops, just in the same way as a series of resistances is dominated only by the biggest ones. One can consider only the hops upward to the transport level. The diffusivity associated to this kind of events is given by the square of the covered distance multiplied by the hopping rate. Finally the mobility can be derived by means of the Einstein relation. This kind of scenario is called Multiple Trapping and Release.[209] Only carriers promoted to the transport level contribute to the electrical conduction and the amount of these carriers is strongly related to the difference between the transport level and the energy of the departure site in the DOS tail.

A.3.2 Field-dependent transport

So far we have discussed the transport properties of disordered semiconductors in presence of only small electric field considered as a weak perturbation for the system. In this case the thermal energy is the only factor that determines the hopping rate. if the strength of the field is increased up to induce a modification of few kT to the barriers between adjacent sites, the mobility is directly affected showing an electric field dependence. The spatial correlation between hopping sites is related to the main mechanism responsible of the degree of disorder of the system.[210] A relationship between the mobility and the electric field applied to the system can be drawn depending on the nature of the spatial disorder. In polymers systems doped by molecules the disorder is considered to be caused by the random orientation of electric dipoles. This leads to a functional dependence of the spatial correlation radius on $1/r$: in that case the mobility follows the Poole-Frenkel dependence on the electric field ($\mu \propto e^{\sqrt{F}}$), where F is the applied electric field. For systems which do not show neat dipoles other models should be exploited to derive the mobility dependence on the electric field.

A.4 The interaction with light

Strong visible absorption and the tunability absorption/emission spectrum are among the main advantages of organic semiconductors.[201] The photon interaction with an organic semiconductor can be described by the Fermi's golden rule:

$$\frac{2\pi}{\hbar} = \left|\langle i \left| H \right| f \rangle\right|^2 \delta(E_f - E_i \pm E) \tag{A.2}$$

where the $\hbar$ is the reduced Planck constant, $\langle i$ is the wavefunction of the initial state, $f\rangle$ is the wavefunction of the final state, H is Hamiltonian associated to the perturbing photon and E is the energy difference between the two states. The delta function states the amount of energy absorbed during the transition, while the term $\left|\langle i \left| H \right| f \rangle\right|^2$accounts for the strength of coupling between the initial and the final state. This latter term strongly depends on how much the initial and final state wavefunctions overlap. In crystalline semiconductors the overlap may be small, e.g. final far-ranging state and initial localized state, while in quantum confined systems will be larger being both final and initial state confined on the same location. In this way the photon absorption would be greater for localized states; this is the case of many organic semiconductors.

When a photon is absorbed an electron is promoted from grount state to an excited one and a tightly bound Frenkel exciton is generated. To collect charges the exciton must be broken generally providing an additional external energy. Being spinless the exciton can dissociate only if at least one of the two carriers in the bound couple is transferred to another site, otherwise the exciton relaxes and the initially excited site comes back to its ground state S_0. Excitons dissociation phenomena are usually divided into intrinsic and extrinsic.

A.4.1 Exciton intrinsic dissociation

The following description is rigorously valid for molecular solids, but it can describe also disordered systems at a first approximation.[201] Called S_n the exited singlet state of a molecule/site it can relax to S_0 through one of the following processes (fig. A.6a):

Internal Conversion (IC) The excited state thermalizes to the intermediate state S_1 releasing energy to vibronic levels. According to the Kasha rule this is a very efficient process. Then a relaxation to the ground state occurs either radiatively or not.

Intersystem Crossing (ISC) The initial singlet state S_n is converted to a triplet state T_n via spin flip. This decay is not allowed by the spin selection rules, but it can happen thanks to the spin orbit coupling (it is an efficient process when heavy atoms are involved). Then, T_n thermalizes to the lower T_1 state. Transition from T_1 to S_0 requires again spin orbit coupling. The average lifetime of T_1 is usually much longer than S_1.

Autoionization (AI) One hot charge can move to an adjacent molecule/site provided that the overlapping integral between the adjacent sites is high enough. This mechanism is rather inefficient in molecular solids for which overlapping integral is generally low. Autoionization is in competition with IC.

Let's analyse the AI process more in details being the one that can contribute to light detection. A photogenerted hot charge carrier that moves

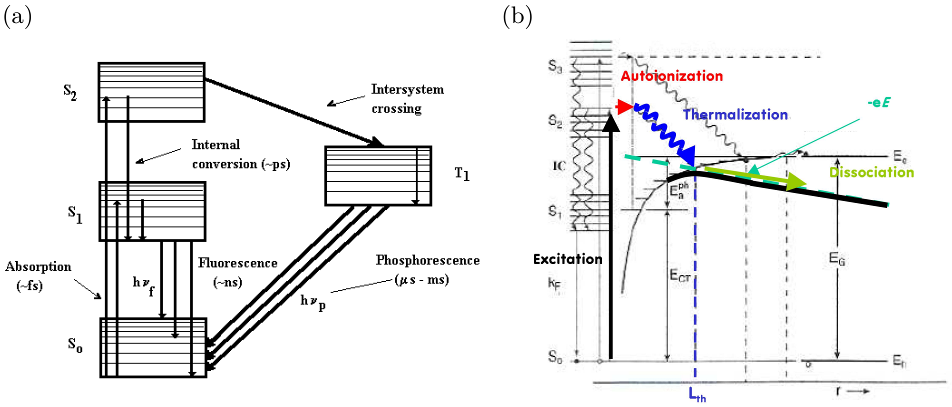

Figure A.6: (a) Jablonski diagram summarizing the possible transitions inside a molecule upon interaction with light. (b) Schematic representation of the processes following the absorption of a photon by an organic molecule in the presence of an electric field. The electric field supplies the excess energy needed to dissociate the molecular exciton.

away from the photogeneration site (AI) will experience several thermalization processes by interacting with the vibrational levels of the system. The spatial distance covered while it loses its excess of energy is called thermalization length (L_{th}) and it's very short ($\sim nm$) due to poor electronic mobility in disordered systems. During the thermalization the electron-hole pair in the Frenkel exciton becomes less tightly bound. This new excitonic state is named Charge Transfer (CT) state. Thermal energy promote the pair dissociation only if it's larger than coulombian interaction. This situation occurs when L_{th} is higher than the capture radius defined as:

$$r_C = \frac{q^2}{4\pi\varepsilon kT} \tag{A.3}$$

If the incoming photon energy is higher than the system bandgap E_g the extra amount of energy can facilitate the dissociation. Typically an excess of $0.5 - 1eV$ would be enough to escape recombination and get exciton dissociation by AI process. Electric field (typically in the order of $10^5 - 10^6 V/cm$), can enhance the carrier migration to an adjacent site according to the Onsager model.[211]

A.4.2 Exciton extrinsic dissociation

Even in presence of high energetic photons or external electric field, the AI is a very inefficient dissociation process. The widely adopted technique to provide enough energy for the exciton break is to mix semiconductors with

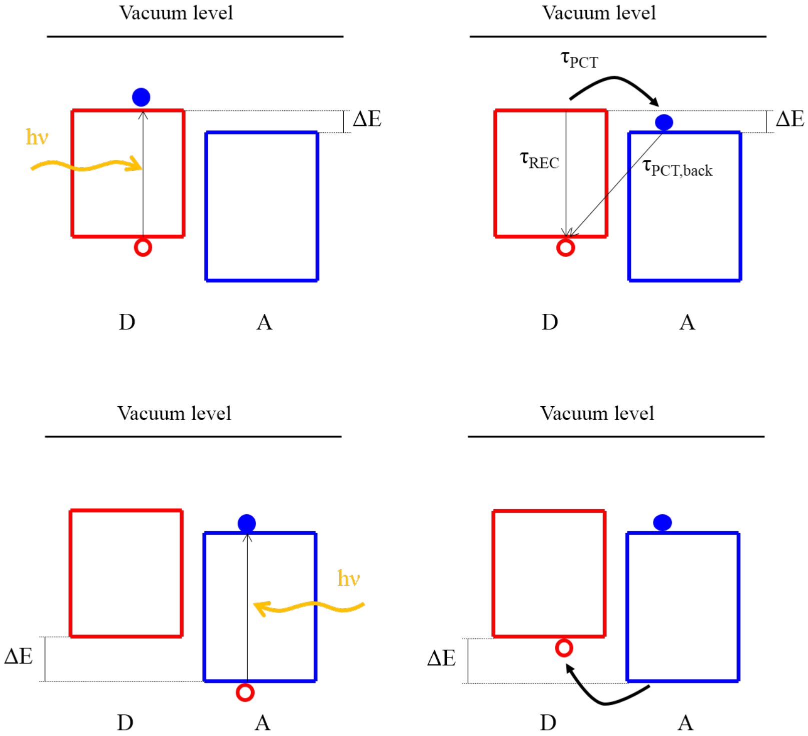

Figure A.7: Schematics of the photoinduced charge transfer between a donor and an acceptor molecule. In the case (a), the exciton generated on the molecule D is broken up by electron transfer to the lower LUMO of the molecule A. In the case (b), the exciton is generated on the molecule A and broken up by hole transfer to the higher lying HOMO level of molecule D. In both the situations, charge transfer from a molecule to the adjacent one is assumed to be energetically favorable for the system.

different electron affinities, namely donor (D) and acceptor (A), in a so called heterojunction.[212,213] If the exciton is generated close enough to the interface between the D and A species, the dissociation probability rises. That requires that charge transfer between the two materials is favoured by energetics: for electrons (holes) generated in the D (A) the LUMO (HOMO) of the acceptor (D) must stay energetically lower (higher) than the LUMO (HOMO) of the D (A) (fig. A.7).

This process ($D^* \rightarrow D^+ + A^-$), named photoinduced charge transfer, is efficient in unbound electron and the hole and make them free to drift towards their respective electrodes. Because excitons have usually limited diffusion lengths in organic semiconductors[212,214] only pairs generated less than a diffusion length far from the D/A interface can undergo dissociation. Therefore the best approach is to realize a bulk heterojunction where a distributed and interpenetrating network of the two species maximizes the area where the excitons can get dissociated.[213,215] Nevertheless, while enhancing the efficiency of excitons break up, continuous paths have to be preserved for both phases, otherwise the separated charges can not percolate towards their respective electrodes. The degree of phase separation between the two species indeed plays a key role: 'comb' structure is the ideal case where the optimum trade-off between charge transport and exciton dissociation is achieved. Other attempts to maximize the area where the excitons can get dissociated were made, i.e. the bilayer structure,[216] where both the acceptor and the donor semiconductors are thinner than the exciton diffusion length. Finally it's worth to report that evidence of dopant-assisted exciton dissociation enhancement was found.[217]

A.4.3 Exciton migration

Exciton transfer can occur from a molecule to another. It can follow different processes either radiative or non-radiative and does not contribute to the photocurrent generation. For radiative transfer the exciton energy is released in the form of radiative decay of the donor molecule and reabsorbed by an acceptor molecular site nearby. The spectral overlap between the two moieties determines the efficiency of this kind of process.[218] Instead, non radiative transfers can basically occur via two different mechanisms.[201] Both of them do not imply any neat charge transfer. Dexter transfer is directly proportional to the overlap integral between the wavefunctions of the two sites involved and it basically implicates a nearest neighbour interaction because of the exponential dependence on the spatial distance ($\sim e^{-x}$). Dexter transfer involves only sites close enough ($0.1 - 1nm$[218]). The latter one is called Förster transfer and it is a dipole-dipole interaction regulated by the overlap between the absorption spectrum of the acceptor phase and the fluorescent spectrum of the donor. Even sites farther apart their Van der Waals radii up to a distance of $10nm$ are interested by Förster transfer.

A.4.4 Photogenerated carriers recombination

A photogenerated hole-electron pair can immediately recombine with a certain probability upon their creation.[201] Recombination is named geminate when the generate pair fails to fully dissociated; non-geminate when occurs between carriers generated by different absorption events. Geminate recombination is one of the main reasons of the external quantum efficiency (EQE) limitations in low mobility systems.[219,220] The electric field comes into play in determining the escape probability for the excitons according to the Onsager theory,[211]. The recombination rate (and hence the escape probability) is expected to be independent on the excitation density and the photocurrent depends linearly on the incident power P (monomolecular decay). If in bimolecular recombination the recombination of charges is controlled by diffusion of carriers in absence of deep traps Langevin model is typically applied.[221] It predicts that the recombination occurs when two carriers of different signs meet each other at a distance less than the critical radius (eq. A.3): in that case they are attracted by Coulombic force, an exciton will form and charges recombine. This mechanism is driven by excitation density. The recombination coefficient is mobility dependent and the photocurrent is proportional to the square root of the optical power ($I \propto P^{\alpha}$, with $\alpha = 0.5$). Therefore the Langevin recombination is dominant at high incident power regimes. In real devices α ranges between 0.5 and 1.[222] The simultaneous presence of different recombination processes can explain the experimental data.[223] Trap-assisted phenomena are the main responsible of the deviation of from the expected mono- or bimolecular models. In low mobility systems traps act as recombination centres. The relationship between the photocurrent and the incident power depends on the traps and on the charge distribution in the system.

A.5 Charge injection

At first approximation the charge injection from metal contacts into an organic material is dominated by the height of the energetic barrier arising from the difference between the metal workfuntion ϕ_M and the LUMO (for electrons) and HOMO (for holes) levels of the organic semiconductor. Joining together a piece of metal and an organic semiconductor, at the thermal equilibrium the Fermi level in the metal and in the organic system must be the same. Consequently there will occur a migration of charges from the metal to the semiconductor (or viceversa) depending on their relative Fermi levels displacement. Built-in potential will appear, sustained by the charges accumulated at the metal/organic interface. On the metal charges accumulate on a surface layer, on the semiconductor side carriers can arise space charge area or interfacial dipoles (fig. A.8).

The first contribution comes from free charges or dopants, while the latter could be due to a variety of mechanisms in organic semiconductors that can alter the interface energetics.[224] Other three contributions come into account in determining the charge injection: the electrostatic energy due to external electric field, the image charge potential and semiconductor disorder that causes inhomogeneities at the interface.[224,225] The injection of charges

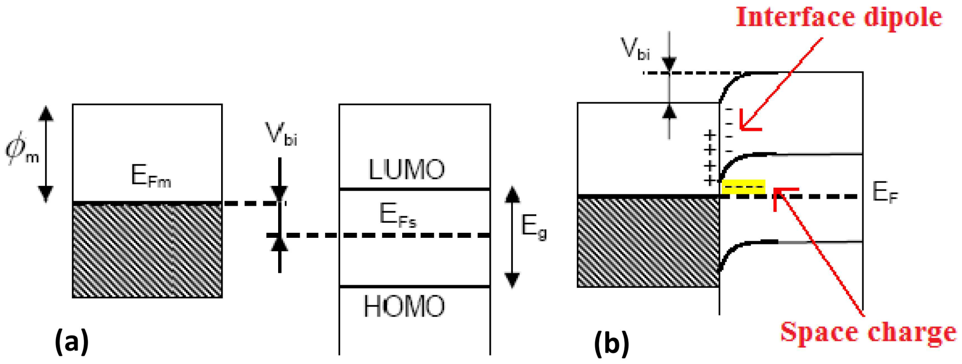

Figure A.8: (a) Schematic of the energy levels in the isolated metal (left) and semiconductor (right). (b) Charge distribution at the metal/semiconductor interface. The Fermi level between the metal and the semiconductor is aligned. The energy levels are bent as a consequence of the built-in potential.

is basically the transition of a carrier from an excited state in the metal to a localized state in the organic semiconductor via thermally assisted tunneling through the energetic barrier between the two states(fig. A.9). A simplified description is based on the thermalization of a hot charge of the metal into a localized state in the semiconductor close to the interface.[224,226] If the thermalization length is higher than the distance between the interface and the peak of the barrier, then the carrier will be effectively injected in the semiconductor, otherwise it will be either pushed back to the interface by the image potential or moved towards the bulk of the semiconductor by thermal agitation. While in high semiconductors mobility the thermionic emission is the limiting factor for charge injection, in low mobility the transport through the interface can be the bottleneck making the injection efficiency mobility dependent, as usually observed for organic semiconductors.

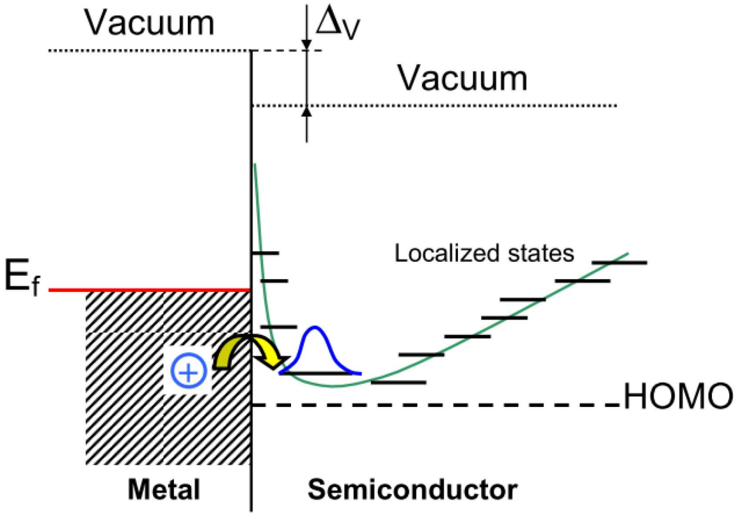

Figure A.9: Hole injection at the metal-semiconductor interface. The 'hot' charge can overcome the barrier occupying a localized state in the semiconductor. The states in the metal are considered delocalized.

Appendix B

Printing parameters

In this appendix inkjet printing parameters used to print inks employed in this work will be reported. For both printers voltage waveforms applied to the piezo are generally drawn and then followed by tables listing specific parameters.

B.1 Jetlab waveforms

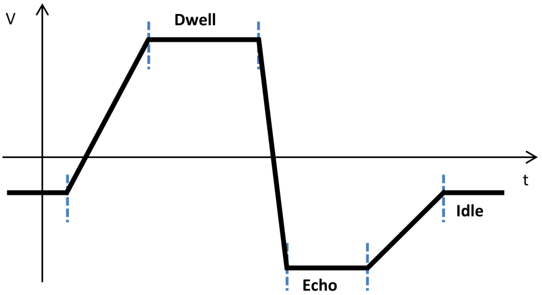

Figure B.1: Voltage waveform parameters for the MicroFab JETLAB 4 printer.

Parameter	P3HT:PCBM and T1:P3HT:PCBM	T1:PCBM
Rise time 1 [μs]	3	10
Dwell time [μs]	20	30
Fall time [μs]	8	3
Echo time [μs]	20	40
Rise time 2 [μs]	20	4
Idle voltage [V]	-6	-5
Dwell voltage [V]	26	50
Echo voltage	-22	30
Jetting frequency [kHz]	500	500
Drop spacing [μm]	70	70

Table B.1: Parameters values for P3HT:PCBM, T1:P3HT:PCBM and T1:PCBM blends.

B.2 Dimatix waveforms

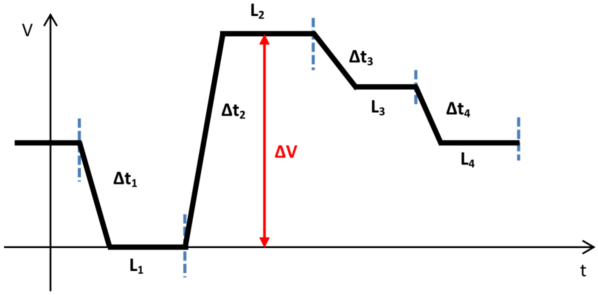

Figure B.2: Voltage waveform parameters for the Dimatix printer.

Parameter	PEDOT inks	TEC-IJ-010	CCI-300
ΔV $[V]$	36	40	40
Δt_1 $[\mu s]$	2.752	2.752	2.688
Δt_2 $[\mu s]$	3.712	3.712	3.776
Δt_3 $[\mu s]$	3.392	3.392	3.392
Δt_4 $[\mu s]$	0.832	0.832	0.832
L_1 $[V]$	0	0	0
L_2 $[V]$	1	1	1
L_3 $[V]$	0.67	0.67	0.47
L_4 $[V]$	0.40	0.40	0.40
Slew rate$_1$ $\Delta V\cdot$ $[\mu s^{-1}]$	0.65	0.65	0.65
Slew rate$_2$ $\Delta V\cdot$ $[\mu s^{-1}]$	0.93	0.93	1.40
Slew rate$_3$ $\Delta V\cdot$ $[\mu s^{-1}]$	0.60	0.60	1.13
Slew rate$_4$ $\Delta V\cdot$ $[\mu s^{-1}]$	0.80	0.80	0.80
Jetting frequency $[kHz]$	1	5	3
Drop spacing $[\mu m]$	35	32	35

Table B.2: Parameters values for conductive inks.

Parameter	PFN	LC153	CB	PMMA
ΔV $[V]$	40	40	40	21
Δt_1 $[\mu s]$	2.752	5.504	7.488	3.456
Δt_2 $[\mu s]$	3.712	7.424	5.76	3.776
Δt_3 $[\mu s]$	3.392	6.784	5.632	2.880
Δt_4 $[\mu s]$	0.832	1.664	2.496	0.832
L_1 $[V]$	0	0	0	0
L_2 $[V]$	1	1	1	1
L_3 $[V]$	0.67	0.67	0.67	0.67
L_4 $[V]$	0.40	0.40	0.53	0.40
Slew rate$_1$ $\Delta V\cdot$ $[\mu s^{-1}]$	0.65	0.65	0.19	2
Slew rate$_2$ $\Delta V\cdot$ $[\mu s^{-1}]$	0.93	0.93	1.47	2
Slew rate$_3$ $\Delta V\cdot$ $[\mu s^{-1}]$	0.60	0.60	0.96	1.33
Slew rate$_4$ $\Delta V\cdot$ $[\mu s^{-1}]$	0.80	0.80	0.8	0.8
Jetting frequency $[kHz]$	5	5	1	1
Drop spacing $[\mu m]$	35	27	5	30

Table B.3: Parameters values for other inks printed with Dimatix.

Bibliography

[1] B J de Gans, P C Duineveld, and U S Schubert. Inkjet Printing of Polymers: State of the Art and Future Developments. *Advanced Materials*, 16(3):203–213, 2004.

[2] Mario Caironi, E Gili, and Henning Sirringhaus. Ink-Jet Printing of Downscaled Organic Electronic Devices. In Hagen Klauk, editor, *Organic Electronics II: More Materials and Applications*, pages 281–326. Wiley-VCH, 2011.

[3] Martin Kaltenbrunner, Tsuyoshi Sekitani, Jonathan Reeder, Tomoyuki Yokota, Kazunori Kuribara, Takeyoshi Tokuhara, Michael Drack, Reinhard Schwödiauer, Ingrid Graz, Simona Bauer-Gogonea, Siegfried Bauer, and Takao Someya. An ultra-lightweight design for imperceptible plastic electronics. *Nature*, 499(7459):458–63, jul 2013.

[4] Yong-Young Noh, Ni Zhao, Mario Caironi, and Henning Sirringhaus. Downscaling of self-aligned, all-printed polymer thin-film transistors. *Nature nanotechnology*, 2(12):784–9, dec 2007.

[5] Jianpu Wang, Xiaoyang Cheng, Mario Caironi, Feng Gao, Xudong Yang, and Neil C. Greenham. Entirely solution-processed write-once-read-many-times memory devices and their operation mechanism. *Organic Electronics*, 12(7):1271–1274, 2011.

[6] Koji Abe, Koji Suzuki, and Daniel Citterio. Inkjet-printed microfluidic multianalyte chemical sensing paper. *Analytical Chemistry*, 80(18):6928–6934, 2008.

[7] Vineet Dua, Sumedh P. Surwade, Srikanth Ammu, Srikanth Rao Agnihotra, Sujit Jain, Kyle E. Roberts, Sungjin Park, Rodney S. Ruoff, and Sanjeev K. Manohar. All-Organic Vapor Sensor Using Inkjet-Printed Reduced Graphene Oxide. *Angewandte Chemie International Edition*, 49(12):2154–2157, 2010.

[8] S. M. Zakir Hossain, Roger E. Luckham, Anne Marie Smith, Julie M. Lebert, Lauren M. Davies, Robert H. Pelton, Carlos D M Filipe, and John D. Brennan. Development of a bioactive paper sensor for detection of neurotoxins using piezoelectric inkjet printing of sol-gel-derived bioinks. *Analytical Chemistry*, 81(13):5474–5483, 2009.

[9] J. Jang, J. Ha, and J. Cho. Fabrication of Water-Dispersible Polyaniline-Poly(4-styrenesulfonate) Nanoparticles For Inkjet-Printed Chemical-Sensor Applications. *Advanced Materials*, 19(13):1772–1775, 2007.

[10] Bo Li, Suresh Santhanam, Lawrence Schultz, Malika Jeffries-EL, Mihaela C. Iovu, Genevieve Sauvé, Jessica Cooper, Rui Zhang, Joseph C. Revelli, Aaron G. Kusne, Jay L. Snyder, Tomasz Kowalewski, Lee E. Weiss, Richard D. McCullough, Gary K. Fedder, and David N. Lambeth. Inkjet printed chemical sensor array based on polythiophene conductive polymers. *Sensors and Actuators, B: Chemical*, 123(2):651–660, 2007.

[11] Claudia N Hoth, Pavel Schilinsky, Stelios A Choulis, and Christoph J Brabec. Printing Highly Efficient Organic Solar Cells. *Nano letters*, 8(9):2806–2813, 2008.

[12] Madhusudan Singh, Hanna M Haverinen, Parul Dhagat, and Ghassan E Jabbour. Inkjet printing-process and its applications. *Advanced materials (Deerfield Beach, Fla.)*, 22(6):673–85, feb 2010.

[13] Sungjune Jung, Antony Sou, Kulbinder Banger, Doo-Hyun Ko, Philip C. Y. Chow, Christopher R. McNeill, and Henning Sirringhaus. All-Inkjet-Printed, All-Air-Processed Solar Cells. *Advanced Energy Materials*, 3(11):1400432, may 2014.

[14] Brian Derby. Inkjet Printing of Functional and Structural Materials: Fluid Property Requirements, Feature Stability, and Resolution. *Annual Review of Materials Research*, 40(1):395–414, jun 2010.

[15] Dan Soltman and Vivek Subramanian. Inkjet-printed line morphologies and temperature control of the coffee ring effect. *Langmuir : the ACS journal of surfaces and colloids*, 24(5):2224–31, mar 2008.

[16] Robert D Deegan, Olgica Bakajin, and Todd F Dupont. Capillary flow as the cause of ring stains from dried liquid drops. *Nature*, 389:827–829, 1997.

[17] Hanlin Wang, Cheng Cheng, Lei Zhang, Hongtao Liu, Yan Zhao, Yunlong Guo, Wenping Hu, Gui Yu, and Yunqi Liu. Inkjet printing short-channel polymer transistors with high-performance and ultrahigh photoresponsivity. *Advanced Materials*, 26:4683–4689, 2014.

[18] Friedrich Dausinger, Friedemann Lichtner, and Holger Lubatschowski, editors. *Femtosecond Technology for Technical and Medical Applications*. 2004.

[19] B. C. Stuart, M. D. Feit, A. M. Rubenchik, B. W. Shore, and M. D. Perry. Laser-Induced Damage in Dielectrics with Nanosecond to Subpicosecond Pulses. *Physical Review Letters*, 74:2248, 1995.

[20] K M Davis, K Miura, N Sugimoto, and K Hirao. Writing waveguides in glass with a femtosecond laser. *Optics letters*, 21(21):1729–1731, 1996.

[21] Yong Son, Junyeob Yeo, Hanul Moon, Tae Woo Lim, Sukjoon Hong, Koo Hyun Nam, Seunghyup Yoo, Costas P. Grigoropoulos, Dong Yol Yang, and Seung Hwan Ko. Nanoscale electronics: Digital fabrication by direct femtosecond laser processing of metal nanoparticles. *Advanced Materials*, 23:3176–3181, 2011.

[22] Sadir G. Bucella, Giorgio Nava, Krishna Chaitanya Vishunubhatla, and Mario Caironi. High-resolution direct-writing of metallic electrodes on flexible substrates for high performance organic field effect transistors. *Organic Electronics*, 14(9):2249–2256, 2013.

[23] Logeeswaran Vj, Jinyong Oh, Avinash P. Nayak, Aaron M. Katzenmeyer, Kristin H. Gilchrist, Sonia Grego, Nobuhiko P. Kobayashi, Shih-Yuan Wang, a. Alec Talin, Nibir K. Dhar, and M. Saif Islam. A Perspective on Nanowire Photodetectors: Current Status, Future Challenges, and Opportunities. *IEEE Journal of Selected Topics in Quantum Electronics*, 17(4):1002–1032, jul 2011.

[24] Kang Jun Baeg, Mario Caironi, and Yong Young Noh. Toward printed integrated circuits based on unipolar or ambipolar polymer semiconductors. *Advanced Materials*, 25(31):4210–4244, 2013.

[25] Xi Wang, Wei Tian, Meiyong Liao, Yoshio Bando, and Dmitri Golberg. Recent advances in solution-processed inorganic nanofilm photodetectors. *Chemical Society reviews*, 43(5):1400–22, 2014.

[26] Roar R. Søndergaard, Markus Hösel, and Frederik C. Krebs. Roll-to-Roll fabrication of large area functional organic materials. *Journal of Polymer Science, Part B: Polymer Physics*, 51(1):16–34, 2013.

[27] Frederik C. Krebs. Fabrication and processing of polymer solar cells: A review of printing and coating techniques. *Solar Energy Materials and Solar Cells*, 93(4):394–412, 2009.

[28] Xiong Gong, Minghong Tong, Yangjun Xia, Wanzhu Cai, Ji Sun Moon, Yong Cao, Gang Yu, Chan-Long Shieh, Boo Nilsson, and Alan J. Heeger. High-Detectivity Polymer Photodetectors with Spectral Response from 300 nm to 1450 nm. *Science (New York, N.Y.)*, 325:1665–1667, 2009.

[29] Amaresh Mishra and Peter Bäuerle. Small molecule organic semiconductors on the move: Promises for future solar energy technology. *Angewandte Chemie - International Edition*, 51(9):2020–2067, 2012.

[30] Wei Jiang, Yan Li, and Zhaohui Wang. Heteroarenes as high performance organic semiconductors. *Chemical Society reviews*, 42(14):6113–27, 2013.

[31] Hakan Usta, Antonio Facchetti, and Tobin J. Marks. N-channel semiconductor materials design for organic complementary circuits. *Accounts of Chemical Research*, 44(7):501–510, 2011.

[32] James C. Blakesley, Fernando A. Castro, William Kylberg, George F a Dibb, Caroline Arantes, Rogério Valaski, Marco Cremona, Jong Soo Kim, and Ji Seon Kim. Towards reliable charge-mobility benchmark measurements for organic semiconductors. *Organic Electronics: physics, materials, applications*, 15(6):1263–1272, 2014.

[33] Jean Roncali, Philippe Leriche, and Philippe Blanchard. Molecular materials for organic photovoltaics: Small is beautiful. *Advanced Materials*, 26(23):3821–3838, 2014.

[34] Stéphane Altazin, Raphaël Clerc, Romain Gwoziecki, Jean Marie Verilhac, Damien Boudinet, Georges Pananakakis, Gérard Ghibaudo, Isabelle Chartier, and Romain Coppard. Physics of the frequency response of rectifying organic Schottky diodes. *Journal of Applied Physics*, 115(6), 2014.

[35] P Peumans, V Bulovic, and S R Forrest. Efficient, high-bandwidth organic multilayer photodetectors. *Applied Physics Letters*, 76(2000):3855–3857, 2000.

[36] Pavel Schilinsky, Christoph Waldauf, Jens Hauch, and Christoph J. Brabec. Polymer photovoltaic detectors: progress and recent developments. *Thin Solid Films*, 451-452:105–108, mar 2004.

[37] Dezhi Yang, Xiaokang Zhou, and Dongge Ma. Fast response organic photodetectors with high detectivity based on rubrene and C60. *Organic Electronics: physics, materials, applications*, 14(11):3019–3023, 2013.

[38] Hugh L. Zhu, Wallace C. H. Choy, Wei E. I. Sha, and Xingang Ren. Photovoltaic Mode Ultraviolet Organic Photodetectors with High On/Off Ratio and Fast Response. *Advanced Optical Materials*, 2(11):1082–1089, nov 2014.

[39] Tatsunari Hamasaki, Taichiro Morimune, Hirotake Kajii, Satoshi Minakata, Ryoji Tsuruoka, Toshiki Nagamachi, and Yutaka Ohmori. Fabrication and characteristics of polyfluorene based organic photodetectors using fullerene derivatives. *Thin Solid Films*, 518(2):548–550, 2009.

[40] Jeramy D. Zimmerman, Vyacheslav V. Diev, Kenneth Hanson, Richard R. Lunt, Eric K. Yu, Mark E. Thompson, and Stephen R. Forrest. Porphyrin-tpe/C60 organic photodetectors with 6.5% external quantum efficiency in the near infrared. *Advanced Materials*, 22(25):2780–2783, 2010.

[41] Kyung Sun Park, Ki Seok Lee, Chan-mo Kang, Jangmi Baek, Kyu Seok Han, Changhee Lee, Yong-eun Koo Lee, Youngjong Kang, and Myung Mo Sung. Cross-Stacked Single-Crystal Organic Nanowire p−n Nanojunction Arrays by Nanotransfer Printing. *Nano letters*, 15:289–293, 2015.

[42] Gerasimos Konstantatos and Edward H Sargent. Nanostructured materials for photon detection. *Nature nanotechnology*, 5(6):391–400, 2010.

[43] Illan J. Kramer and Edward H. Sargent. The architecture of colloidal quantum dot solar cells: Materials to devices. *Chemical Reviews*, 114(1):863–882, 2014.

[44] Vahid a. Akhavan, Brian W. Goodfellow, Matthew G. Panthani, Dariya K. Reid, Danny J. Hellebusch, Takuji Adachi, and Brian a. Korgel. Spray-deposited CuInSe2 nanocrystal photovoltaics. *Energy & Environmental Science*, 3(10):1600, 2010.

[45] M. Böberl, M. V. Kovalenko, S. Gamerith, E. J. W. List, and W. Heiss. Inkjet-Printed Nanocrystal Photodetectors Operating up to 3 μm Wavelengths. *Advanced Materials*, 19(21):3574–3578, nov 2007.

[46] Tobias Rauch, Michaela Böberl, Sandro F. Tedde, Jens Fürst, Maksym V. Kovalenko, Günter Hesser, Uli Lemmer, Wolfgang Heiss,

and Oliver Hayden. Near-infrared imaging with quantum-dot-sensitized organic photodiodes. *Nature Photonics*, 3(6):332–336, may 2009.

[47] Sean Keuleyan, Emmanuel Lhuillier, Vuk Brajuskovic, and Philippe Guyot-Sionnest. Mid-infrared HgTe colloidal quantum dot photodetectors. *Nature Photonics*, 5(8):489–493, 2011.

[48] Andy Eu-Jin Lim, Junfeng Song, Qing Fang, Chao Li, Xiaoguang Tu, Ning Duan, Kok Kiong Chen, Roger Poh-Cher Tern, and Tsung-Yang Liow. Review of Silicon Photonics Foundry Efforts. *IEEE Journal of Selected Topics in Quantum Electronics*, 20(4):8300112, 2014.

[49] Kang-Jun Baeg, Maddalena Binda, Dario Natali, Mario Caironi, and Yong-Young Noh. Organic light detectors: photodiodes and phototransistors. *Advanced materials (Deerfield Beach, Fla.)*, 25(31):4267–95, aug 2013.

[50] Juan Cabanillas-Gonzalez, Giulia Grancini, and Guglielmo Lanzani. Pump-probe spectroscopy in organic semiconductors: Monitoring fundamental processes of relevance in optoelectronics. *Advanced Materials*, 23(46):5468–5485, 2011.

[51] Murray A. Lampert and Peter Mark. Current Injection in Solids. *Science*, 170(3961):966–967, nov 1970.

[52] S. O. Kasap. *Optoelectronics and photonics: principles and practices.* Prentice Hall, 2nd edition, 2001.

[53] Silvano Donati. *Photodetectors: Devices, Circuits and Applications.* Prentice Hall, 1999.

[54] Thomas D. Anthopoulos. Electro-optical circuits based on light-sensing ambipolar organic field-effect transistors. *Applied Physics Letters*, 91(11):2005–2008, 2007.

[55] Paul H. Wöbkenberg, John G. Labram, Jean-Marie Swiecicki, Ksenia Parkhomenko, Dusan Sredojevic, Jean-Paul Gisselbrecht, Dago M. de Leeuw, Donal D. C. Bradley, Jean-Pierre Djukic, and Thomas D. Anthopoulos. Ambipolar organic transistors and near-infrared phototransistors based on a solution-processable squarilium dye. *Journal of Materials Chemistry*, 20(18):3673, 2010.

[56] Samuele Lilliu, Michaela Böberl, Maria Sramek, Sandro F. Tedde, J. Emyr Macdonald, and Oliver Hayden. Inkjet-printed organic photodiodes. *Thin Solid Films*, 520(1):610–615, oct 2011.

[57] Jason R Wojciechowski, Lisa C Shriver-Lake, Mariko Y Yamaguchi, Erwin Füreder, Roland Pieler, Martin Schamesberger, Christoph Winder, Hans Jürgen Prall, Max Sonnleitner, and Frances S Ligler. Organic photodiodes for biosensor miniaturization. *Analytical chemistry*, 81(9):3455–61, 2009.

[58] Leah Lucas Lavery, Gregory Lewis Whiting, and Ana Claudia Arias. All ink-jet printed polyfluorene photosensor for high illuminance detection. *Organic Electronics*, 12(4):682–685, apr 2011.

[59] Jingda Wu and Lih Y Lin. Inkjet Printable Flexible Thin-Film NCQD Photodetectors on Unmodified Transparency Films. *IEEE Photonics Technology Letters*, 26(7):737–740, 2014.

[60] Yu Yang, Soichiro Omi, Ryo Goto, Masayuki Yahiro, Masanao Era, Hirofumi Watanabe, and Yuji Oki. Wavelength sensitive photodiodes in the visible based on J-type aggregated films patterned by inkjet method. *Organic Electronics*, 12(3):405–410, 2011.

[61] Claudia N. Hoth, Andrea Seemann, Roland Steim, Tayebeh Ameri, Hamed Azimi, and Christoph J. Brabec. Printed Organic Solar Cells. In Gavin Conibeer and Arthur Willoughby, editors, *Solar Cell Materials: Developing Technologies*. Wiley-VCH, 2014.

[62] Kiran Kumar Manga, Shuai Wang, Manu Jaiswal, Qiaoliang Bao, and Kian Ping Loh. High-gain graphene-titanium oxide photoconductor made from inkjet printable ionic solution. *Advanced materials (Deerfield Beach, Fla.)*, 22(46):5265–70, dec 2010.

[63] David J. Finn, Mustafa Lotya, Graeme Cunningham, Ronan J. Smith, David McCloskey, John F. Donegan, and Jonathan N. Coleman. Inkjet deposition of liquid-exfoliated graphene and MoS2 nanosheets for printed device applications. *Journal of Materials Chemistry C*, 2(5):925, 2014.

[64] Yong-Hoon Kim, Jeong-In Han, Min-Koo Han, John E. Anthony, Jacky Park, and Sung Kyu Park. Highly light-responsive ink-jet printed 6,13-bis(triisopropylsilylethynyl) pentacene phototransistors with suspended top-contact structure. *Organic Electronics*, 11(9):1529–1533, sep 2010.

[65] Minseok Kim, Hyun-Jun Ha, Hui-Jun Yun, In-Kyu You, Kang-Jun Baeg, Yun-Hi Kim, and Byeong-Kwon Ju. Flexible organic phototransistors based on a combination of printing methods. *Organic Electronics*, 15(11):2677–2684, 2014.

[66] Minseok Kim, Jae Bon Koo, Kang-Jun Baeg, Soon-Won Jung, Byeong-Kwon Ju, and In-Kyu You. Top-gate staggered poly(3,3'-dialkyl-quarterthiophene) organic thin-film transistors with reverse-offset-printed silver source/drain electrodes. *Applied Physics Letters*, 101(13):133306, 2012.

[67] Saumen Mandal, Giorgio Dell'Erba, Alessandro Luzio, Sadir Gabriele Bucella, Andrea Perinot, Alberto Calloni, Giulia Berti, Gianlorenzo Bussetti, Lamberto Duò, Antonio Facchetti, Yong-Young Noh, and Mario Caironi. Fully-printed, all-polymer, bendable and highly transparent complementary logic circuits. *Organic Electronics*, 20:132–141, 2015.

[68] Yan Wu, Emad Girgis, Valter Ström, Wolfgang Voit, Lyubov Belova, and K. V. Rao. Ultraviolet light sensitive In-doped ZnO thin film field effect transistor printed by inkjet technique. *Physica Status Solidi (a)*, 208(1):206–209, jan 2011.

[69] Jiantong Li, Maziar M. Naiini, Sam Vaziri, Max C. Lemme, and Mikael Östling. Inkjet Printing of MoS 2. *Advanced Functional Materials*, 24(41):6524–6531, nov 2014.

[70] E. Katzir, S. Yochelis, Y. Paltiel, S. Azoubel, a. Shimoni, and S. Magdassi. Tunable inkjet printed hybrid carbon nanotubes/nanocrystals light sensor. *Sensors and Actuators B: Chemical*, 196:112–116, jun 2014.

[71] http://www.isorg.fr/actu/2/plastic-logic-and-isorg-claim-the-prestigious-flexi-award-for-their-revolutionary-flexible-plastic-image-sensor_206.htm.

[72] Sandro F Tedde, Johannes Kern, Tobias Sterzl, Jens Fu, Paolo Lugli, and Oliver Hayden. Fully Spray Coated Organic Photodiodes. *Nano letters*, 9(3):4–7, 2009.

[73] Daniela Baierl, Lucio Pancheri, Morten Schmidt, David Stoppa, Gian-Franco Dalla Betta, Giuseppe Scarpa, and Paolo Lugli. A hybrid CMOS-imager with a solution-processable polymer as photoactive layer. *Nature communications*, 3:1175, jan 2012.

[74] Claire M Lochner, Yasser Khan, Adrien Pierre, and Ana C Arias. All-organic optoelectronic sensor for pulse oximetry. *Nature Communications*, 5:1–7, 2014.

[75] Hagen Marien, Michiel Steyaert, and Paul Heremans. Analog Organic Electronics. *Analog Circuits and Signal Processing*, pages 1–13, 2013.

[76] Giorgio Dell'Erba, Andrea Perinot, Andrea Grimoldi, Dario Natali, and Mario Caironi. Fully-Printed , all-polymer integrated twilight switch. *Semiconductor Science and Technology*, 30(10):104005, 2015.

[77] Berend-Jan de Gans, Lijing Xue, Uday S. Agarwal, and Ulrich S. Schubert. Ink-Jet Printing of Linear and Star Polymers. *Macromolecular Rapid Communications*, 26(4):310–314, feb 2005.

[78] Yinhua Zhou, Canek Fuentes-Hernandez, Jaewon Shim, Jens Meyer, Anthony J Giordano, Hong Li, Paul Winget, Theodoros Papadopoulos, Hyeunseok Cheun, Jungbae Kim, Mathieu Fenoll, Amir Dindar, Wojciech Haske, Ehsan Najafabadi, Talha M Khan, Hossein Sojoudi, Stephen Barlow, Samuel Graham, Jean-Luc Brédas, Seth R Marder, Antoine Kahn, and Bernard Kippelen. A universal method to produce low-work function electrodes for organic electronics. *Science (New York, N.Y.)*, 336(6079):327–32, apr 2012.

[79] J. C. Blakesley and R. Speller. Modeling the imaging performance of prototype organic x-ray imagers. *Medical Physics*, 35(1):225, 2008.

[80] M. Binda, D. Natali, M. Sampietro, T. Agostinelli, and L. Beverina. Organic based photodetectors: Suitability for X- and Γ-rays sensing application. *Nuclear Instruments and Methods in Physics Research Section A: Accelerators, Spectrometers, Detectors and Associated Equipment*, 624(2):443–448, dec 2010.

[81] a. Iacchetti, M. Binda, D. Natali, M. Giussani, L. Beverina, C. Fiorini, R. Peloso, and M. Sampietro. Multi-Layer Organic Squaraine-Based Photodiode for Indirect X-Ray Detection. *IEEE Transactions on Nuclear Science*, 59(5):1862–1867, 2012.

[82] Steven K. Hau, Hin-Lap Yip, and Alex K.-Y. Jen. A Review on the Development of the Inverted Polymer Solar Cell Architecture. *Polymer Reviews*, 50(4):474–510, 2010.

[83] Panagiotis E Keivanidis, Neil C Greenham, Henning Sirringhaus, Richard H Friend, James C Blakesley, Robert Speller, Mariano Campoy Quiles, Tiziano Agostinelli, Donal D C Bradley, and Jenny Nelson. X-ray stability and response of polymeric photodiodes for imaging applications. *Applied Physics Letters*, 92(023304):1–3, 2008.

[84] Gerwin H. Gelinck, Abhishek Kumar, Date Moet, Jan-Laurens van der Steen, Umar Shafique, Pawel E. Malinowski, Kris Myny, Barry P. Rand, Matthias Simon, Walter Rütten, Alexander Douglas, Jorrit Jorritsma,

Paul Heremans, and Ronn Andriessen. X-ray imager using solution processed organic transistor arrays and bulk heterojunction photodiodes on thin, flexible plastic substrate. *Organic Electronics*, 14(10):2602–2609, jul 2013.

[85] Zhengchun Liu, Yi Su, and Kody Varahramyan. Inkjet-printed silver conductors using silver nitrate ink and their electrical contacts with conducting polymers. *Thin Solid Films*, 478(1-2):275–279, may 2005.

[86] Claudio Girotto, Davide Moia, Barry P. Rand, and Paul Heremans. High-Performance Organic Solar Cells with Spray-Coated Hole-Transport and Active Layers. *Advanced Functional Materials*, 21(1):64–72, jan 2011.

[87] J. a. Lim, W. H. Lee, H. S. Lee, J. H. Lee, Y. D. Park, and K. Cho. Self-Organization of Ink-jet-Printed Triisopropylsilylethynyl Pentacene via Evaporation-Induced Flows in a Drying Droplet. *Advanced Functional Materials*, 18(2):229–234, 2008.

[88] Andrea Grimoldi. *Photodiodes Based on Polythiophene Deposited with Inkjet Printing Technique.* Master thesis, Politecnico di Milano, 2012.

[89] Claudia N. Hoth, Stelios a. Choulis, Pavel Schilinsky, and Christoph J. Brabec. On the effect of poly(3-hexylthiophene) regioregularity on inkjet printed organic solar cells. *Journal of Materials Chemistry*, 19(30):5398, 2009.

[90] Minh Trung Dang, Lionel Hirsch, Guillaume Wantz, and James D Wuest. Controlling the Morphology and Performance of Bulk Heterojunctions in Solar Cells. Lessons Learned from the Benchmark Poly(3-hexylthiophene):[6,6]-Phenyl-C61-butyric Acid Methyl Ester System. *Chemical Reviews*, 113(5):3734–3765, 2013.

[91] Daniela Baierl, Bernhard Fabel, Paolo Gabos, Lucio Pancheri, Paolo Lugli, and Giuseppe Scarpa. Solution-processable inverted organic photodetectors using oxygen plasma treatment. *Organic Electronics*, 11(7):1199–1206, jul 2010.

[92] Daniela Baierl, Bernhard Fabel, Paolo Lugli, and Giuseppe Scarpa. Efficient indium-tin-oxide (ITO) free top-absorbing organic photodetector with highly transparent polymer top electrode. *Organic Electronics*, 12(10):1669–1673, 2011.

[93] Xilan Liu, Hangxing Wang, Tingbin Yang, Wei Zhang, and Xiong Gong. Solution-processed ultrasensitive polymer photodetectors with high external quantum efficiency and detectivity. *ACS Applied Materials and Interfaces*, 4(7):3701–3705, 2012.

[94] Marc Ramuz, Lukas Bürgi, Carsten Winnewisser, and Peter Seitz. High sensitivity organic photodiodes with low dark currents and increased lifetimes. *Organic Electronics*, 9(3):369–376, jun 2008.

[95] M. Punke, S. Valouch, S.W. Kettlitz, N. Christ, C. Gärtner, M. Gerken, and Uli Lemmer. Dynamic characterization of organic bulk heterojunction photodetectors. *Applied Physics Letters*, 91(07):071118, 2007.

[96] Martin Burkhardt, Wei Liu, Christopher G. Shuttle, Kaustav Banerjee, and Michael L. Chabinyc. Top illuminated inverted organic ultraviolet photosensors with single layer graphene electrodes. *Applied Physics Letters*, 101(3):033302, 2012.

[97] Valentin D. Mihailetchi, Hangxing Xie, Bert De Boer, L. Jan Anton Koster, and Paul W M Blom. Charge transport and photocurrent generation in poly(3-hexylthiophene): Methanofullerene bulk-heterojunction solar cells. *Advanced Functional Materials*, 16(5):699–708, 2006.

[98] Francesco Arca, Sandro F Tedde, Maria Sramek, Julia Rauh, Paolo Lugli, and Oliver Hayden. Interface trap States in organic photodiodes. *Scientific reports*, 3:1324, feb 2013.

[99] Bogdan Vlad Popescu, Dan Horia Popescu, Paolo Lugli, Simone Locci, Francesco Arca, Sandro Francesco Tedde, Maria Sramek, and Oliver Hayden. Modeling and Simulation of Organic Photodetectors for Low Light Intensity Applications. *IEEE Transactions on Electron Devices*, 60(6):1975–1981, jun 2013.

[100] Dario Natali and Mario Caironi. Charge injection in solution-processed organic field-effect transistors: physics, models and characterization methods. *Advanced materials (Deerfield Beach, Fla.)*, 24(11):1357–87, mar 2012.

[101] Kenjiro Fukuda, Tomohito Sekine, Daisuke Kumaki, and Shizuo Tokito. Profile control of inkjet printed silver electrodes and their application to organic transistors. *ACS applied materials & interfaces*, 5(9):3916–20, 2013.

[102] Emeline Saracco, Benjamin Bouthinon, Jean Marie Verilhac, Caroline Celle, Nicolas Chevalier, Denis Mariolle, Olivier Dhez, and Jean Pierre Simonato. Work function tuning for high-performance solution-processed organic photodetectors with inverted structure. *Advanced Materials*, 25:6534–6538, 2013.

[103] Chao He, Chengmei Zhong, Hongbin Wu, Renqiang Yang, Wei Yang, Fei Huang, Guillermo C. Bazan, and Yong Cao. Origin of the enhanced open-circuit voltage in polymer solar cells via interfacial modification using conjugated polyelectrolytes. *Journal of Materials Chemistry*, 20(13):2617, 2010.

[104] Hua Zheng, Yina Zheng, Nanliu Liu, Na Ai, Qing Wang, Sha Wu, Junhong Zhou, Diangang Hu, Shufu Yu, Shaohu Han, Wei Xu, Chan Luo, Yanhong Meng, Zhixiong Jiang, Yawen Chen, Dongyun Li, Fei Huang, Jian Wang, Junbiao Peng, and Yong Cao. All-solution processed polymer light-emitting diode displays. *Nature Communications*, 4(May):1–7, 2013.

[105] Corey V Hoven, Renqiang Yang, Andres Garcia, Victoria Crockett, Alan J Heeger, Guillermo C Bazan, and Thuc-Quyen Nguyen. Electron injection into organic semiconductor devices from high work function cathodes. *Proceedings of the National Academy of Sciences of the United States of America*, 105(35):12730–5, sep 2008.

[106] Fei Guo, Xiangdong Zhu, Karen Forberich, Johannes Krantz, Tobias Stubhan, Michael Salinas, Marcus Halik, Stefanie Spallek, Benjamin Butz, Erdmann Spiecker, Tayebeh Ameri, Ning Li, Peter Kubis, Dirk M. Guldi, Gebhard J. Matt, and Christoph J. Brabec. ITO-Free and Fully Solution-Processed Semitransparent Organic Solar Cells with High Fill Factors. *Advanced Energy Materials*, 3(8):1062–1067, 2013.

[107] Bogyu Lim, Jang Jo, Seok-In Na, Juhwan Kim, Seok-Soon Kim, and Dong-Yu Kim. A morphology controller for high-efficiency bulk-heterojunction polymer solar cells. *Journal of Materials Chemistry*, 20(48):10919, 2010.

[108] Marco Sampietro, Gianfranco Accomoando, Luca G Fasoli, Giorgio Ferrari, and Emilio C Gatti. High Sensitivity Noise Measurement with a Correlation Spectrum Analyzer. *IEEE Transactions on Instrumentation and Measurement*, 49(4):1–3, 2000.

[109] Stephen R Forrest. The path to ubiquitous and low-cost organic electronic appliances on plastic. *Nature*, 428(6986):911–918, 2004.

[110] Gerwin H Gelinck, Abhishek Kumar, Date Moet, Jan-laurens P J Van Der Steen, Albert J J M Van Breemen, Santosh Shanmugam, Arjan Langen, Jan Gilot, Pim Groen, Ronn Andriessen, Matthias Simon, Walter Ruetten, Alexander U Douglas, Rob Raaijmakers, Pawel E Malinowski, and Kris Myny. X-Ray Detector-on-Plastic With High Sensitivity Using Low Cost , Solution-Processed Organic Photodiodes. *IEEE Transactions on Electron Devices*, 18(9383):1–8, 2015.

[111] Jean-Pierre Moy. Large area X-ray detectors based on amorphous silicon technology. *Thin Solid Films*, 337(1-2):213–221, jan 1999.

[112] Francesco Arca, Eduard Kohlstädt, Sandro F Tedde, Paolo Lugli, and Oliver Hayden. Large Active Area Organic Photodiodes for Short-Pulse X-ray Detection. *IEEE Transactions on Electron Devices*, 60(5):1663–1667, 2013.

[113] Larry E. Antonuk, Qihua Zhao, Youcef El-Mohri, Hong Du, Yi Wang, Robert a. Street, Jackson Ho, Richard Weisfield, and William Yao. An investigation of signal performance enhancements achieved through innovative pixel design across several generations of indirect detection, active matrix, flat-panel arrays. *Medical Physics*, 36(7):3322, 2009.

[114] R.a Street, J Graham, Z.D Popovic, a Hor, S Ready, and J Ho. Image sensors combining an organic photoconductor with a-Si:H matrix addressing. *Journal of Non-Crystalline Solids*, 299-302:1240–1244, apr 2002.

[115] R.a. Street, R.L. Weisfield, R.B. Apte, S.E. Ready, a. Moore, M. Nguyen, W.B. Jackson, and P. Nylen. Amorphous silicon sensor arrays for X-ray and document imaging. *Thin Solid Films*, 296(1-2):172–176, mar 1997.

[116] R.L. Weisfield. Amorphous silicon TFT X-ray image sensors. In *International Electron Devices Meeting 1998. Technical Digest (Cat. No.98CH36217)*, pages 21–24. IEEE.

[117] Gyuseong Cho, J. S. Drewery, W. S. Hong, T. Jing, S. N. Kaplan, H Lee, A Mireshghi, V. Perez-Mendez, and D Wildermuth. Signal Readout in a-Si:H Pixel Detectors. *IEEE transactions on nuclear science*, 40(4):323–327, 1993.

[118] M Hoheisel, M Arques, J Chabbal, C Chaussat, T Ducourant, G Hahm, H Horbaschek, R Schulz, and M Spahn. Amorphous silicon X-ray detectors. *Journal of Non-Crystalline Solids*, 227-230:1300–1305, may 1998.

[119] Tse Nga Ng, Rene a. Lujan, Sanjiv Sambandan, Robert a. Street, Scott Limb, and William S. Wong. Low temperature a-Si:H photodiodes and flexible image sensor arrays patterned by digital lithography. *Applied Physics Letters*, 91(6):89–92, 2007.

[120] Andrei Sazonov, Denis Striakhilev, C. H O Lee, and Arokia Nathan. Low-temperature materials and thin film transistors for flexible electronics. *Proceedings of the IEEE*, 93(8):1420–1428, 2005.

[121] Tse Nga Ng, William S. Wong, Michael L. Chabinyc, Sanjiv Sambandan, and Robert a. Street. Flexible image sensor array with bulk heterojunction organic photodiode. *Applied Physics Letters*, 92(21):213303, 2008.

[122] Pawel E Malinowski, Peter Vicca, Myriam Willegems, Sarah Schols, David Cheyns, Steve Smout, Marc Ameys, Kris Myny, Subramanian Vaidyanathan, Emmanuel Martin, Abhishek Kumar, Jan-laurens Van Der Steen, Gerwin Gelinck, and Paul Heremans. Organic Imager on Readout Backplane Based on TFTs With Cross-Linkable Dielectrics. *IEEE Photonics Technology Letters*, 26(21):2197–2200, 2014.

[123] Toshitake Takahashi, Zhibin Yu, Kevin Chen, Daisuke Kiriya, Chuan Wang, Kuniharu Takei, Hiroshi Shiraki, Teresa Chen, Biwu Ma, and Ali Javey. Carbon nanotube active-matrix backplanes for mechanically flexible visible light and X-ray imagers. *Nano letters*, 13(11):5425–30, nov 2013.

[124] Gerwin H. Gelinck, Abhishek Kumar, Date Moet, Jan-Laurens van der Steen, Umar Shafique, Pawel E. Malinowski, Kris Myny, Barry P. Rand, Matthias Simon, Walter Rütten, Alexander Douglas, Jorrit Jorritsma, Paul Heremans, and Ronn Andriessen. X-ray imager using solution processed organic transistor arrays and bulk heterojunction photodiodes on thin, flexible plastic substrate. *Organic Electronics*, 14(10):2602–2609, oct 2013.

[125] Xiaoran Tong and Stephen R. Forrest. An integrated organic passive pixel sensor. *Organic Electronics: physics, materials, applications*, 12(11):1822–1825, 2011.

[126] C. Kyle Renshaw, Xin Xu, and Stephen R. Forrest. A monolithically integrated organic photodetector and thin film transistor. *Organic Electronics: physics, materials, applications*, 11(1):175–178, 2010.

[127] Safa O Kasap and John A Rowlands. Direct-Conversion Flat-Panel X-Ray Image Sensors for Digital Radiography. *Proceedings of the IEEE*, 90(4), 2002.

[128] Youcef El-Mohri, Larry E. Antonuk, Qihua Zhao, Yi Wang, Yixin Li, Hong Du, and Amit Sawant. Performance of a high fill factor, indirect detection prototype flat-panel imager for mammography. *Medical Physics*, 34(1):315, 2007.

[129] R K Swank. Calculation of modulation transfer functions of x-ray fluorescent screens. *Applied optics*, 12(8):1865–70, 1973.

[130] Abbas El Gamal and Helmy Eltoukhy. CMOS Image Sensors. *Circuits and Devices Magazine, IEEE*, 21(3):6 – 20, 2005.

[131] M Maolinbay, Y El-Mohri, L E Antonuk, K W Jee, S Nassif, X Rong, and Q Zhao. Additive noise properties of active matrix flat-panel imagers. *Medical physics*, 27(8):1841–54, aug 2000.

[132] J H Siewerdsen, L E Antonuk, Y El-Mohri, J Yorkston, W Huang, J M Boudry, and I a Cunningham. Empirical and theoretical investigation of the noise performance of indirect detection, active matrix flat-panel imagers (AMFPIs) for diagnostic radiology. *Medical physics*, 24(1):71–89, jan 1997.

[133] Florian Machui, Stefan Langner, Xiangdong Zhu, Steven Abbott, and Christoph J. Brabec. Determination of the P3HT:PCBM solubility parameters via a binary solvent gradient method: Impact of solubility on the photovoltaic performance. *Solar Energy Materials and Solar Cells*, 100:138–146, may 2012.

[134] Rosa M Masegosa, Margarita G Prolongo, Irmina Herntindez-fuentes, and Arturo Horta. Preferential and Total Sorption of Poly(methy1 methacrylate) in the Cosolvents Formed by Acetonitrile with Pentyl Acetate and with Alcohols (1-Butanol, 1-Propanol, and Methanol). *Macromolecules*, 17:1181–1187, 1984.

[135] Giorgio Dell'Erba, Andrea Perinot, Andrea Grimoldi, Dario Natali, and Mario Caironi. Fully-printed, all-polymer integrated twilight switch. *Semiconductor Science and Technology*, 30(10):104005, 2015.

[136] G Azzellino, A Grimoldi, M Binda, M Caironi, D Natali, and M Sampietro. Fully Inkjet Printed Organic Photodetectors with High Quantum Yield. *Advanced materials (Deerfield Beach, Fla.)*, 25(47):6829–33, sep 2013.

[137] Giuseppina Pace, Andrea Grimoldi, Marco Sampietro, Dario Natali, and Mario Caironi. Printed photodetectors. *Semiconductor Science and Technology*, 30(10):104006, 2015.

[138] Giuseppina Pace, Andrea Grimoldi, Dario Natali, Marco Sampietro, Jessica E. Coughlin, Guillermo C. Bazan, and Mario Caironi. All-Organic and Fully-Printed Semitransparent Photodetectors based on Narrow Bandgap Conjugated Molecules. *Advanced Materials*, 26:6773–6777, sep 2014.

[139] Adrien Pierre, Igal Deckman, Pierre Balthazar Lechêne, and Ana Claudia Arias. High Detectivity All-Printed Organic Photodiodes, 2015.

[140] Emeline Saracco, Benjamin Bouthinon, Jean-Marie Verilhac, Caroline Celle, Nicolas Chevalier, Denis Mariolle, Olivier Dhez, and Jean-Pierre Simonato. Work Function Tuning for High-Performance Solution-Processed Organic Photodetectors with Inverted Structure. *Advanced Materials*, 25(45):6534–6538, oct 2013.

[141] Panagiotis E. Keivanidis, Siong Hee Khong, Peter K H Ho, Neil C. Greenham, and Richard H. Friend. All-solution based device engineering of multilayer polymeric photodiodes: Minimizing dark current. *Applied Physics Letters*, 94(17):39–41, 2009.

[142] M. Binda, A. Iacchetti, D. Natali, L. Beverina, M. Sassi, and M. Sampietro. High detectivity squaraine-based near infrared photodetector with nA/cm[sup 2] dark current. *Applied Physics Letters*, 98(7):073303, 2011.

[143] Jesse R. Manders, Tzung-Han Lai, Yanbin An, Weikai Xu, Jaewoong Lee, Do Young Kim, Gijs Bosman, and Franky So. Low-Noise Multispectral Photodetectors Made from All Solution-Processed Inorganic Semiconductors. *Advanced Functional Materials*, 24:7205–10, 2014.

[144] Sebastian Valouch, Christian Hönes, Siegfried W. Kettlitz, Nico Christ, Hung Do, Michael F.G. Klein, Heinz Kalt, Alexander Colsmann, and Uli Lemmer. Solution processed small molecule organic interfacial layers for low dark current polymer photodiodes. *Organic Electronics*, 13(11):2727–2732, nov 2012.

[145] Xiong Gong, Minghong Tong, Yangjun Xia, Wanzhu Cai, Ji Sun Moon, Yong Cao, Gang Yu, Chan-Long Shieh, Boo Nilsson, and Alan J Heeger. High-detectivity polymer photodetectors with spectral response from 300 nm to 1450 nm. *Science (New York, N.Y.)*, 325(5948):1665–7, sep 2009.

[146] Takakazu Yamamoto and Hideki Hayashi. pi-Conjugated soluble and fluorescent poly (thiophene-2, 5-diyl)s with phenolic, hindered phenolic and p-C6H4OCH3 Substituents. Preparation, optical properties, and Redox Reaction. *Journal of Polymer Science Part A: ...*, 35:463–474, 1997.

[147] Morten Schmidt, Aniello Falco, Marius Loch, Paolo Lugli, and Giuseppe Scarpa. Spray coated indium-tin-oxide-free organic photodiodes with PEDOT:PSS anodes. *AIP Advances*, 4(10):107132, 2014.

[148] Chao-Te Liu, Wen-Hsi Lee, and Jui-Feng Su. Pentacene-Based Thin Film Transistor with Inkjet-Printed Nanocomposite High-K Dielectrics. *Active and Passive Electronic Components*, 2012:1–7, 2012.

[149] Huiqiong Zhou, Yuan Zhang, Cheng-Kang Mai, Samuel D Collins, Thuc-Quyen Nguyen, Guillermo C Bazan, and Alan J Heeger. Conductive Conjugated Polyelectrolyte as Hole-Transporting Layer for Organic Bulk Heterojunction Solar Cells. *Advanced materials (Deerfield Beach, Fla.)*, pages 1–6, oct 2013.

[150] Jung Hwa Seo, Andrea Gutacker, Yanming Sun, Hongbin Wu, Fei Huang, Yong Cao, Ullrich Scherf, Alan J. Heeger, and Guillermo C. Bazan. Improved high-efficiency organic solar cells via incorporation of a conjugated polyelectrolyte interlayer. *Journal of the American Chemical Society*, 133(22):8416–8419, 2011.

[151] Kai Zhang, Zhicheng Hu, Chunhui Duan, Lei Ying, Fei Huang, and Yong Cao. The effect of methanol treatment on the performance of polymer solar cells. *Nanotechnology*, 24(48):484003, dec 2013.

[152] Sooji Nam, Jaeyoung Jang, Hyojung Cha, Jihun Hwang, Tae Kyu An, Seonuk Park, and Chan Eon Park. Effects of direct solvent exposure on the nanoscale morphologies and electrical characteristics of PCBM-based transistors and photovoltaics. *Journal of Materials Chemistry*, 22(12):5543, 2012.

[153] a. Iacchetti, D. Natali, M. Binda, L. Beverina, and M. Sampietro. Hopping photoconductivity in an exponential density of states. *Applied Physics Letters*, 101(10):103307, 2012.

[154] Anke Teichler, Jolke Perelaer, and Ulrich S. Schubert. Inkjet printing of organic electronics – comparison of deposition techniques and state-of-the-art developments. *Journal of Materials Chemistry C*, 1(10):1910, 2013.

[155] Paul Polishuk. Plastic optical fibers branch out. *IEEE Communications Magazine*, 44(9):140–148, 2006.

[156] A. R. Jha. *Infrared Technology - Applications to Electro-Optics, Photonic Devices, and Sensors.* Wiley-VCH, 2000.

[157] Y. Yao, Y. Liang, V. Shrotriya, S. Xiao, L. Yu, and Y. Yang. Plastic Near-Infrared Photodetectors Utilizing Low Band Gap Polymer. *Advanced Materials*, 19(22):3979–3983, 2007.

[158] Andrea Pais, Ansuman Banerjee, David Klotzkin, and Ian Papautsky. High-sensitivity, disposable lab-on-a-chip with thin-film organic electronics for fluorescence detection. *Lab on a Chip*, 8(5):794, 2008.

[159] Maureen Kaine-Krolak and Mark E. Novak. An Introduction to Infrared Technology: Applications in the Home, Classroom, Workplace, and Beyond ... *Closing the Gap, Presentation Manuscript*, 1995.

[160] Taichiro Morimune, Hirotake Kajii, and Yutaka Ohmori. Photoresponse properties of a high-speed organic photodetector based on copper-phthalocyanine under red light illumination. *IEEE Photonics Technology Letters*, 18(24):2662–2664, 2006.

[161] Maddalena Binda, Dario Natali, Antonio Iacchetti, and Marco Sampietro. Integration of an Organic Photodetector onto a Plastic Optical Fiber by Means of Spray Coating Technique. *Advanced Materials*, pages n/a–n/a, jun 2013.

[162] Akiko Kobayashi, Masaaki Sasa, Wakako Suzuki, Emiko Fujiwara, Hisashi Tanaka, Madoka Tokumoto, Yoshinori Okano, Hideki Fujiwara, and Hayao Kobayashi. Infrared electronic absorption in a single-component molecular metal. *Journal of the American Chemical Society*, 126(2):426–7, 2004.

[163] M Carla Aragoni, Massimiliano Arca, Mario Caironi, Carla Denotti, Francesco a Devillanova, Emanuela Grigiotti, Francesco Isaia, Franco Laschi, Vito Lippolis, Dario Natali, Luca Pala, S S, Via a Moro, Politecnico Milano, P L Vinci, and Via Celoria. Monoreduced [M(R,R' timdt)2]-dithiolenes (M=Ni, Pd , Pt ; R,R' timdt = disubstituted imidazolidine-2,4,5-trithione): solid state photoconducting properties in the third optical fiber window. *Chemical Communication*, 1:1882–1883, 2004.

[164] Anke Teichler, Jolke Perelaer, Florian Kretschmer, Martin D. Hager, and Ulrich S. Schubert. Systematic investigation of a novel low-bandgap terpolymer library via inkjet printing: Influence of ink properties and processing conditions. *Macromolecular Chemistry and Physics*, 214:664–672, 2013.

[165] Kenjiro Fukuda, Yasunori Takeda, Makoto Mizukami, Daisuke Kumaki, and Shizuo Tokito. Fully Solution-Processed Flexible Organic Thin Film Transistor Arrays with High Mobility and Exceptional Uniformity. *Scientific Reports*, 4(20 V):4–11, 2014.

[166] Yong-Hoon Kim, Byungwook Yoo, John E. Anthony, and Sung Kyu Park. Controlled Deposition of a High-Performance Small-Molecule Organic Single-Crystal Transistor Array by Direct Ink-Jet Printing. *Advanced Materials*, 24(4):497–502, 2012.

[167] Harald Hoppe and Niyazi Serdar Sariciftci. Morphology of polymer/fullerene bulk heterojunction solar cells. *Journal of Materials Chemistry*, 16(1):45, 2006.

[168] Liying Cui, Junhu Zhang, Xuemin Zhang, Long Huang, Zhanhua Wang, Yunfeng Li, Hainan Gao, Shoujun Zhu, Tieqiang Wang, and Bai Yang. Suppression of the coffee ring effect by hydrosoluble polymer additives. *ACS applied materials & interfaces*, 4(5):2775–80, may 2012.

[169] Thomas S. van der Poll, John a. Love, Thuc-Quyen Nguyen, and Guillermo C. Bazan. Non-Basic High-Performance Molecules for Solution-Processed Organic Solar Cells. *Advanced Materials*, 24(27):3646–3649, 2012.

[170] Vinay Gupta, Aung Ko Ko Kyaw, Dong Hwan Wang, Suresh Chand, Guillermo C Bazan, and Alan J Heeger. Barium: an efficient cathode layer for bulk-heterojunction solar cells. *Scientific reports*, 3:1965, 2013.

[171] Aung Ko Ko Kyaw, Dong Hwan Wang, Vinay Gupta, Jie Zhang, Suresh Chand, Guillermo C. Bazan, and Alan J. Heeger. Efficient Solution-Processed Small-Molecule Solar Cells with Inverted Structure. *Advanced Materials*, pages n/a–n/a, mar 2013.

[172] Aung Ko Ko Kyaw, Dong Hwan Wang, Vinay Gupta, Wei Lin Leong, Lin Ke, Guillermo C. Bazan, and Alan J Heeger. Intensity Dependence of Current -Voltage Characteristics and Recombination in High-Efficiency. *ACS nano*, 7(5):4569–4577, 2013.

[173] Ye Huang, Wen Wen, Subhrangsu Mukherjee, Harald Ade, Edward J. Kramer, and Guillermo C. Bazan. High-Molecular-Weight Insulating Polymers Can Improve the Performance of Molecular Solar Cells. *Advanced Materials*, 26(24):4168–4172, 2014.

[174] Toby a M Ferenczi, Christian Müller, Donal D C Bradley, Paul Smith, Jenny Nelson, and Natalie Stingelin. Organic semiconductor:insulator polymer ternary blends for photovoltaics. *Advanced materials (Deerfield Beach, Fla.)*, 23(35):4093–7, sep 2011.

[175] Aung Ko Ko Kyaw, Dong Hwan Wang, Chan Luo, Yong Cao, Thuc-Quyen Nguyen, Guillermo C. Bazan, and Alan J. Heeger. Effects of Solvent Additives on Morphology, Charge Generation, Transport, and Recombination in Solution-Processed Small-Molecule Solar Cells. *Advanced Energy Materials*, 4(7):1301469–1301478, 2014.

[176] John a. Love, Christopher M. Proctor, Jianhua Liu, Christopher J. Takacs, Alexander Sharenko, Thomas S. van der Poll, Alan J. Heeger, Guillermo C. Bazan, and Thuc-Quyen Nguyen. Film Morphology of High Efficiency Solution-Processed Small-Molecule Solar Cells. *Advanced Functional Materials*, 23(40):5019–5026, 2013.

[177] Wanli Ma, Jin Young Kim, Kwanghee Lee, and Alan J. Heeger. Effect of the Molecular Weight of Poly(3-hexylthiophene) on the Morphology and Performance of Polymer Bulk Heterojunction Solar Cells. *Macromolecular Rapid Communications*, 28(17):1776–1780, 2007.

[178] Fei Huang, Hongbin Wu, Deli Wang, Wei Yang, and Yong Cao. Based on Polyfluorene. *Society*, 16(8):708–716, 2004.

[179] Renqiang Yang, Hongbin Wu, Yong Cao, and Guillermo C Bazan. Control of cationic conjugated polymer performance in light emitting diodes by choice of counterion. *Journal of the American Chemical Society*, 128(45):14422–14423, 2006.

[180] Zhicai He, Chengmei Zhong, Shijian Su, Miao Xu, Hongbin Wu, and Yong Cao. Enhanced power-conversion efficiency in polymer solar cells using an inverted device structure. *Nature Photonics*, 6(9):593–597, aug 2012.

[181] Floris B Kooistra, Valentin D Mihailetchi, Lacramioara M Popescu, David Kronholm, Paul W M Blom, and Jan C Hummelen. New C 84 Derivative and Its Application in a Bulk Heterojunction Solar Cell. *Chemistry Materials*, 18:3068–3073, 2006.

[182] Corey Hoven, Renqiang Yang, Andres Garcia, Alan J. Heeger, Thuc Quyen Nguyen, and Guillermo C. Bazan. Ion motion in conjugated polyelectrolyte electron transporting layers. *Journal of the American Chemical Society*, 129(36):10976–10977, 2007.

[183] Paul Heremans. Electronics on plastic foil, for applications in flexible OLED displays, sensor arrays and circuits. In *2014 21st Int. Workshop on Active-Matrix Flatpanel Displays and Devices (Am-Fpd)*, pages 1–4, 2004.

[184] M. Hambsch, K. Reuter, H. Kempa, and a.C. Hübler. Comparison of fully printed unipolar and complementary organic logic gates. *Organic Electronics*, 13(10):1989–1995, 2012.

[185] M. Hambsch, K. Reuter, M. Stanel, G. Schmidt, H. Kempa, U. Fügmann, U. Hahn, and a.C. Hübler. Uniformity of fully gravure printed organic field-effect transistors. *Materials Science and Engineering: B*, 170(1-3):93–98, 2010.

[186] Kris Myny, Erik van Veenendaal, Gerwin H. Gelinck, Jan Genoe, Wim Dehaene, and Paul Heremans. An 8-Bit, 40-Instructions-Per-Second Organic Microprocessor on Plastic Foil. *IEEE Journal of Solid-State Circuits*, 47(1):284–291, 2012.

[187] Giorgio Dell'Erba, Alessandro Luzio, Dario Natali, Juhwan Kim, Dongyoon Khim, Dong-Yu Kim, Yong-Young Noh, and Mario Caironi. Organic integrated circuits for information storage based on ambipolar polymers and charge injection engineering. *Applied Physics Letters*, 104(15):153303, 2014.

[188] M. Guerin, a. Daami, S. Jacob, E. Bergeret, E. Bènevent, P. Pannier, and R. Coppard. High-gain fully printed organic complementary circuits on flexible plastic foils. *IEEE Transactions on Electron Devices*, 58(10):3587–3593, 2011.

[189] H. Kempa, M. Hambsch, K. Reuter, M. Stanel, G. C. Schmidt, B. Meier, and a. C. Hübler. Complementary ring oscillator exclusively prepared by means of gravure and flexographic printing. *IEEE Transactions on Electron Devices*, 58(8):2765–2769, 2011.

[190] Laura Basiricò, Piero Cosseddu, Beatrice Fraboni, and Annalisa Bonfiglio. Inkjet printing of transparent, flexible, organic transistors. *Thin Solid Films*, 520(4):1291–1294, 2011.

[191] Dongyoon Khim, Hyun Han, Kang-Jun Baeg, Juhwan Kim, Sun-Woo Kwak, Dong-Yu Kim, and Yong-Young Noh. Simple Bar-Coating Process for Large-Area, High-Performance Organic Field-Effect Transistors and Ambipolar Complementary Integrated Circuits. *Advanced Materials*, 25(31):4302–4308, 2013.

[192] Huipeng Chen, Raghavendra Hegde, J Browning, and M D Dadmun. The miscibility and depth profile of PCBM in P3HT: thermodynamic information to improve organic photovoltaics. *Physical chemistry chemical physics : PCCP*, 14(16):5635–41, apr 2012.

[193] Sungjune Jung, Antony Sou, Enrico Gili, and Henning Sirringhaus. Inkjet-printed resistors with a wide resistance range for printed read-only memory applications. *Organic Electronics*, 14(3):699–702, 2013.

[194] I. M. Filanovsky and H. Baltes. CMOS Schmitt trigger design. *IEEE Transactions on Circuits and Systems I: Fundamental Theory and Applications*, 41(1):46–49, 1994.

[195] Hagen Klauk. Organic thin-film transistors. *Chemical Society Reviews*, 39(7):2643, 2010.

[196] Neil C. Bird. A simple, solar spectral model for direct-normal and diffuse horizontal irradiance. *Solar Energy*, 32(4):461–471, 1984.

[197] M. Loudon. *Organic Chemistry.* 5th edition, 2009.

[198] H. Haken and H. C. Wolf. *Molecular Physics and Elements of Quantum Chemistry.* 2th edition, 2004.

[199] Francis Garnier. Thin-film transistors based on organic conjugated semiconductors. *Chemical Physics*, 227(1-2):253–262, 1998.

[200] Rudolf E. Peierls. *Quantum theory of solids.* Oxford Univeristy Press, 1955.

[201] M. Pope and C. E. Swenberg. *Electronic Processes in Organic Crystals.* Clarendon Press, 1982.

[202] D.J. Griffiths. *Introduction to Quantum Mechanics.* Prentice-Hall, 1995.

[203] H Bassler. Charge Transport in Disordered Organic Photoconductors. *Physica Status Solidi (b)*, 175:15, 1993.

[204] T. Holstein. Studies of polaron motion: Part I. The molecular-crystal model. *Annals of Physics*, 8(3):325–342, 1959.

[205] N. Karl. Charge carrier transport in organic semiconductors. *Synthetic Metals*, 133-134:649–657, 2003.

[206] Allen Miller and Elihu Amrahams. Impurity Conduction at Low Concentrations. *Physical Review*, 120(3):745–755, 1960.

[207] V.I Arkhipov, E.V Emelianova, G.J Adriaenssens, and H Bässler. Equilibrium carrier mobility in disordered organic semiconductors. *Journal of Non-Crystalline Solids*, 299-302:1047–1051, apr 2002.

[208] S. D. Baranovskii, T. Faber, F. Hensel, and P. Thomas. The applicability of the transport-energy concept to various disordered materials. *Journal of Physics: Condensed Matter*, 9(13):2699–2706, 1999.

[209] G Horowitz. Organic field-effect transistors. *Advanced Materials*, 10(5):365–377, 1998.

[210] M. Bouhassoune, S.L.M. Van Mensfoort, P.a. Bobbert, and R. Coehoorn. Carrier-density and field-dependent charge-carrier mobility in organic semiconductors with correlated Gaussian disorder. *Organic Electronics*, 10(3):437–445, 2009.

[211] L Onsager. Initial Recombination oj Ions. *Physical Review*, 54(554-557), 1938.

[212] P. W. M. Blom, V. D. Mihailetchi, L. J. a. Koster, and D. E. Markov. Device Physics of Polymer:Fullerene Bulk Heterojunction Solar Cells. *Advanced Materials*, 19(12):1551–1566, 2007.

[213] Christoph J. Brabec, Srinivas Gowrisanker, Jonathan J. M. Halls, Darin Laird, Shijun Jia, and Shawn P. Williams. Polymer-Fullerene Bulk-Heterojunction Solar Cells. *Advanced Materials*, 22(34):3839–3856, 2010.

[214] Richard R. Lunt, Noel C. Giebink, Anna a. Belak, Jay B. Benziger, and Stephen R. Forrest. Exciton diffusion lengths of organic semiconductor thin films measured by spectrally resolved photoluminescence quenching. *J. Appl. Phys.*, 105(5):053711, 2009.

[215] Jenny Nelson. Polymer:fullerene bulk heterojunction solar cells. *Materials Today*, 14(10):462–470, 2011.

[216] Jen-Hsien Huang, Kuang-Chieh Li, Dhananjay Kekuda, Hari Hara Padhy, Hong-Cheu Lin, Kuo-Chuan Ho, and Chih-Wei Chu. Efficient bilayer polymer solar cells possessing planar mixed-heterojunction structures. *Journal of Materials Chemistry*, 20(16):3295, 2010.

[217] V. I. Arkhipov and H. Bässler. Exciton dissociation and charge photogeneration in pristine and doped conjugated polymers. *Physica Status Solidi (a)*, 201(6):1152–1187, may 2004.

[218] Clifford B Murphy, Yan Zhang, Thomas Troxler, Vivian Ferry, Justin J Martin, and Wayne E Jones. Probing Fo 1 rster and Dexter Energy-Transfer Mechanisms in Fluorescent Conjugated Polymer Chemosensors. *Journal of Chemical B*, 17:1537–1543, 2004.

[219] R. R. Chance and C. L. Braun. Temperature dependence of intrinsic carrier generation in anthracene single crystals. *Journal of Chemical Physics*, 64:3573, 1976.

[220] J. Noolandi and K. M. Hong. Theory of photogeneration and fluorescence quenching. *Journal of Chemical Physics*, 70:3230, 1979.

[221] T. Skotheim and John R Reynolds. *Conjugated Polymers - Theory, Synthesis, Properties and Characterization.* CRC press, 3rd edition, 2006.

[222] Ingo Riedel and Vladimir Dyakonov. Influence of electronic transport properties of polymer-fullerene blends on the performance of bulk heterojunction photovoltaic devices. *Physica Status Solidi (a)*, 201(6):1332–1341, may 2004.

[223] Albert Rose. *Concepts in Photoconductivity and Allied Problems.* Interscience Publisher, 1963.

[224] J. Campbell Scott. Metal–organic interface and charge injection in organic electronic devices. *Journal of Vacuum Science and Technology A*, 21(521), 2003.

[225] Luca Fumagalli. *Organic transistors based onpolyexylthiophene: modeling, realization and encapsulation with Al2O3.* Phd, Politecnico di Milano, 2008.

[226] P. R. Emtage and J. J. O'Dwyer. Richardson-Schottky Effect in Insulators. *Physical Review Letters*, 16:356, 1966.

List of Figures

List of Tables

List of Publications during the Ph.D.

Publications on Journals

- G. Pace, A. Grimoldi, M. Sampietro, D. Natali and M. Caironi, "Printed photodetectors", Semicond. Sci. Technol., 2015, DOI: 10.1088/0268-1242/30/10/104006
- G. Dell'Erba, A. Perinot, A. Grimoldi, D. Natali and M. Caironi, "Fully-printed, all-polymer integrated twilight switch", Semicond. Sci. Technol., 2015, DOI: 10.1088/0268-1242/30/10/104005
- G. Pace, A. Grimoldi, D. Natali, M. Sampietro, J. E. Coughlin, G. C. Bazan and M. Caironi, "All-Organic and Fully-Printed Semitransparent Photodetectors based in Narrow Bandgap Conjugated Molecules", Adv. Mat., 2014, DOI: 10.1002/adma.201402918
- G. Azzellino, A. Grimoldi, M. Binda, M. Caironi, D. Natali and M. Sampietro, "Fully inkjet printed organic photodetectors with high quantum yield", Adv. Mat., 2013, DOI: 10.1002/adma.201303473

Publications on Congress Proceedings

- A. Grimoldi, G. Azzellino, S. G. Buccella, M. Caironi, D. Natali and M. Sampietro, "Inkjet printing of photodetector and transistor for a pixelated digital imager based on organiza semiconductors", 45th GE Conference, 2013, ISBN: 978-88-903069-3-8, pp. 85-86

Acknowledgements

Giunto alla fine di un lungo percorso di studi vorrei ringraziare tutti coloro che mi hanno aiutato a renderlo bello e interessante.

Desidero ringraziare Dario Natali per avermi guidato, sapientemente consigliato e sostenuto lasciandomi grande libertà e iniziativa. Un ringraziamento va anche a Marco Sampietro e Mario Caironi che mi hanno aiutato ad allargare lo sguardo su stimolanti prospettive.

Grazie a tutti i colleghi del PME, in particolare Sadir, Giovanni, Giuseppina, Letizia, Maddalena, Antonio, Giorgio e Andrea, per il prezioso aiuto, non solo pratico. Ringrazio anche i colleghi e tesisti del LabSamp, Pietro e Giacomo per aver condiviso gli anni del dottorato, Lorenzo, Giacomo e Eleonora per avermi sopportato, Giorgio per i pazienti consigli, Matteo e tutti coloro che hanno reso pranzi e pause caffé dei momenti allegri e costruttivi. Un ringraziamento va anche a chi ha contribuito al progetto InDiXi e ai collaboratori della University of California - Santa Barbara, Guillermo Bazan e Jessica Coughlin.

Infine, un grazie semplice e speciale alla mia famiglia e a tutti gli amici.